

Technische Universität München
Institut für Energietechnik

Lehrstuhl für Thermodynamik

Modeling of Automotive HVAC Units Using Proper Orthogonal Decomposition

Paul Christ

Vollständiger Abdruck der von der Fakultät für Maschinenwesen der
Technischen Universität München zur Erlangung des akademischen Grades
eines

DOKTOR – INGENIEURS

genehmigten Dissertation.

Vorsitzender:

Prof. Dr.-Ing. Gunther Reinhart

Prüfer der Dissertation:

1. Prof. Dr.-Ing. Thomas Sattelmayer
2. Prof. Dr.-Ing. Jürgen Köhler

Die Dissertation wurde am 18.12.2018 bei der Technischen Universität München eingereicht
und durch die Fakultät für Maschinenwesen am 16.04.2019 angenommen.

Vorwort

Diese Arbeit entstand am Lehrstuhl für Thermodynamik der Technischen Universität München während meiner Tätigkeit als wissenschaftlicher Mitarbeiter. Sie wurde finanziert von der Audi AG im Rahmen der INI.TUM-Kooperation. Aus diesem Grund verbrachte ich einen Teil der Promotionszeit bei der Audi AG in der Entwicklung Klimaregelung.

Ich danke besonders meinem Doktorvater, Herrn Professor Dr.–Ing. Thomas Sattelmayer, für die fachliche Betreuung meiner Arbeit und die Übernahme des Hauptreferates. Er hat mit seinen zielführenden Einwänden zum erfolgreichen Gelingen dieser Arbeit beigetragen und mir dennoch Freiraum in der wissenschaftlichen Gestaltung des Projektes gegeben.

Bei Herrn Professor Dr.–Ing. Jürgen Köhler bedanke ich mich für die freundliche Übernahme des Koreferates und bei Herrn Professor Dr.–Ing. Gunther Reinhart für den Vorsitz bei der mündlichen Prüfung.

Nicht nur für das Korrekturlesen, sondern auch für die zahlreichen fachlichen Diskussionen und wertvollen Impulse danke ich Herrn Dr.–Ing. Christoph Hirsch. Meinen Kollegen Alexander Präbst sowie Florian Kiefer, Hannes Dietz und Bernd Heithorst danke ich darüber hinaus in besonderem Maße für die mir in der Promotionszeit geleistete Unterstützung. Mein Dank gilt auch allen weiteren Kollegen für die freundliche Atmosphäre am Lehrstuhl.

Neben der Finanzierung des Projektes hat die Audi AG mir Prüfstände, Sachmittel und Messinstrumente zur Verfügung gestellt. Nicht zuletzt wurde ich auch herzlich in die Abteilung Klimaregelung und in das Audi Doktorandenetzwerk aufgenommen. Besonders Bastian Schmandt hat mich fachlich und auch darüber hinaus unterstützt. Dafür und für die gute Zusammenarbeit bedanke ich mich.

Am Ende waren es jedoch meine Frau Gladys und meine Familie, die mir durch ihr Verständnis, ihren Rückhalt und ihre Geduld das notwendige Durchhaltevermögen gegeben haben.

München, Dezember 2018

Paul Christ

Abstract

In modern vehicle concepts the outlet temperatures of automotive Heating, Ventilation and Air Conditioning (HVAC) units are measured and regulated by an Automatic Climate Control (ACC) to guarantee pleasant thermal comfort for the passengers. A Reduced Order Model approach for HVAC units is developed for model-based climate control to eliminate costly temperature sensors and increase comfort. The methodology combines the strength of well established first law modeling methods with Proper Orthogonal Decomposition (POD) to form an accurate description of flow and mixing in HVAC units.

The core component of the approach is a POD model of the mixing process in the HVAC unit. The proposed POD approach focuses only on control-relevant outlet values in contrast to the traditional application of the POD, which is the POD-Galerkin projection. The methodology developed was first assessed with numerical simulations of a simplified HVAC model. It was shown that the proposed POD method predicts the outlet values with high accuracy. Next, the developed procedure was applied to a real HVAC unit using measurements from a test rig. High accuracy of the predicted outlet values was demonstrated. Measurement data from the transient heat up of a vehicle cabin was used to assess the system simulation of the HVAC unit under real driving conditions. The model remains accurate in quasi-steady state while larger errors occur during highly transient heating due to the missing description of heat transfer phenomena upstream of the ventilation ducts.

This HVAC system simulation was further integrated into a model-based control scheme as an alternative to the standard control procedure in vehicles. The model-based approach exploits the HVAC model to calculate the valve positions for a set of desired outlet values. The proposed control procedure was demonstrated by using a test rig and a vehicle. The calculated valve positions produced only minor differences between the desired outlet values and the measured quantities. The need for temperature sensors can be eliminated with the model-based control scheme while saving money and maintaining or even increasing comfort and safety standards for passengers.

Contents

Nomenclature	vii
List of Tables	xiv
List of Figures	xix
1 Introduction	1
1.1 State of the Art	4
1.1.1 Overview of Modeling Approaches	4
1.1.2 Selection of Modeling Techniques	11
1.2 Goal and Structure of the Thesis	13
2 Proper Orthogonal Decomposition	15
2.1 Introduction to Proper Orthogonal Decomposition	15
2.2 Galerkin Projection (G-POD)	19
2.2.1 Application to Flow Fields in HVAC Units	20
2.2.2 Application to Integral Balances of HVAC Units	26
2.3 POD Based on Control-Relevant Output Parameters (O-POD) . .	29
2.3.1 Introduction to O-POD Procedure	29
2.3.2 Application to Flow and Mixing in HVAC Units	33
2.4 Summary of the POD Models	36
3 Experiments	39
3.1 Test Rig	39
3.1.1 Structure and Function of the Test Rig	39
3.1.2 Design of Components	43
3.1.3 Measurement Procedure	47
3.1.4 Structure of the Experimental Data Set	48

3.2	Vehicle Measurement	50
3.2.1	Test Vehicle	51
3.2.2	Measurement Setup	51
4	Prediction of Flow and Mixing in HVAC Units	53
4.1	Numerical Benchmark Simulation	53
4.1.1	Physical Model	54
4.1.2	Comparison of Galerkin Projection With O-POD Procedure	58
4.2	HVAC Model	73
4.2.1	Modeling Approach	73
4.2.2	Model Assessment	78
5	Application of the HVAC Model	93
5.1	Vehicle Application	93
5.1.1	Driving Cycle	93
5.1.2	Results and Accuracy of the HVAC Model	99
5.2	Model-based Control	106
5.2.1	Test Rig	108
5.2.2	Vehicle	113
6	Summary and Conclusions	121
A	Sub-Models of the HVAC Unit	127
B	Measurement Instrumentation	133
B.1	Detailed Error Analysis of the Test Rig	133
B.2	Specification of Measurement Instrumentation	137
	Previous Publications	141
	Supervised Student Theses	143
	Bibliography	145

Nomenclature

Latin Symbols

A	Area [m^2]
a	Weighting coefficient of POD modes [-]
B	Thickness [m]
C	Correlation tensor [-]
c	Index of test case [-]
c_p	Specific heat capacity [$\text{J kg}^{-1} \text{K}^{-1}$]
D	Diameter [m]
D	Diffusion coefficient [m s^{-2}]
F	Scaling factor for flow resistance [m^{-1}]
H	Enthalpy [J]
L	Length [m]
m	Instance of observation [-]
m	Mass [kg]
M	Torque [Nm]
N_c	Number of test case [-]
N_r	Truncated number of POD modes [-]
N_s	Number of observations [-]
N_x	Values of system states [-]
N	Number of outlets [-]
n	Revolutions per minute [s^{-1}]
p_t	Total pressure [$\text{kg m}^{-1} \text{s}^{-2}$]
p_v	Pressure of water vapor [$\text{kg m}^{-1} \text{s}^{-2}$]
p	Pressure [$\text{kg m}^{-1} \text{s}^{-2}$]

NOMENCLATURE

Q	Heat [J]
\dot{q}	Heat flux [W m^{-2}]
R_s	Specific gas constant for dry air [$\text{J kg}^{-1}\text{K}^{-1}$]
R_v	Specific gas constant for water vapor [$\text{J kg}^{-1}\text{K}^{-1}$]
R	Autocorrelation tensor [-]
R	Radius [m]
R	Summarized loss coefficient [-]
S	Momentum source [m s^{-2}]
s	Location [-]
T	Temperature [K]
t	Time [s]
U	Mean velocity [m s^{-1}]
u	Uncertainty [-]
u	Velocity [m s^{-1}]
V	Volume [m^3]
W	Weighting factor [-]
x	Spatial direction [m]
y	Output value [-]
B	Scalar convection matrix [-]
C	Mode matrix [-]
C	Momentum convection matrix [-]
D	Diffusion matrix [-]
\mathcal{F}	Fluid resistance constraint matrix [-]
\mathcal{F}	POD modes constraint matrix [-]
\mathcal{M}	Divergence matrix [-]
\mathcal{N}	Operator of governing equation [-]
\mathcal{P}	Pressure matrix [-]
\mathcal{S}	Source matrix [-]
\mathcal{T}	Viscous stresses matrix [-]

Greek Symbols

α	Valve angle [°]
ϵ	Error [-]
η	Efficiency [-]
Γ	Boundary surface [m ²]
λ	Eigenvalue of POD mode [-]
μ	Mean average [-]
ν	Viscosity [m ² s ⁻¹]
ω	Blockage [-]
Ω	Domain [-]
ρ	Density [kg m ⁻³]
τ	Thermal time constant [s]
θ	POD mode [-]
φ	Flow variable [-]
φ	Relative air humidity [-]
ζ	Dimensionless loss coefficient [-]

Superscripts

\sim	Estimated
$+$	Dimensionless
\cdot	Per unit time
m	Enumerator of instance [-]
n	Enumerator of instance [-]

Subscripts

Amb	Ambient
Byp	Bypass

NOMENCLATURE

<i>Cavity</i>	Mixing cavity
<i>c</i>	Enumerator of test case
<i>Defr</i>	Defrost outlet
<i>Duct</i>	Ventilation duct
<i>eff</i>	Effective
<i>Evap</i>	Evaporator
<i>Exp</i>	Experiment
<i>E</i>	Ambient
<i>Face</i>	Face outlet
<i>Flow</i>	Flow specific
<i>Foot</i>	Foot outlet
<i>FR</i>	Flow resistance network
<i>HX</i>	Heat exchanger
<i>Inflow</i>	Flow at inlet
<i>Iso</i>	Insulation
<i>i</i>	Enumerator for POD modes
<i>I</i>	Inner
<i>j</i>	Enumerator for POD modes
<i>k</i>	Climate zone of HVAC unit
<i>k</i>	Enumerator for POD modes
<i>L</i>	Left climate zone
<i>max</i>	Minimum
<i>min</i>	Maximum
<i>Non – Obs</i>	Not observed
<i>n</i>	Outlet
<i>Obs</i>	Observed
<i>Outflow</i>	Flow at outlet
<i>O</i>	Outer
<i>R</i>	Right climate zone
<i>Side</i>	Side outlet
<i>Sim</i>	Simulated
<i>SP</i>	Setpoint
<i>tot</i>	Total
<i>t</i>	Turbulent

Dimensionless Numbers

<i>Bi</i>	Biot number
<i>Pr</i>	Prandtl number
<i>Re</i>	Reynolds number
<i>Sc</i>	Schmidt number

Acronyms

<i>ACC</i>	Automatic Climate Control
<i>ANN</i>	Artificial Neural Network
<i>ARMAX</i>	Autoregressive Moving Average Exogenous
<i>CFD</i>	Computational Fluid Dynamics
<i>DOF</i>	Degree of Freedom
<i>FL</i>	Fuzzy Logic
<i>FR</i>	Flow Resistance
<i>G – POD</i>	Proper Orthogonal Decomposition Galerkin
<i>GS</i>	Galerkin equation System
<i>HVAC</i>	Heating, Ventilation and Air Conditioning
<i>HX</i>	Heat Exchanger
<i>IH</i>	Inhomogeneity
<i>O – POD</i>	Output based Proper Orthogonal Decomposition
<i>ODE</i>	Ordinary Differential Equations
<i>ODE</i>	Ordinary Differential Equations
<i>PCA</i>	Principal Component Analysis
<i>PI</i>	Proportional-Integral
<i>PMV</i>	Predicted Mean Vote
<i>POD</i>	Proper Orthogonal Decomposition
<i>RANS</i>	Reynolds-Averaged-Navier-Stokes

NOMENCLATURE

<i>RIC</i>	Relative Information Content
<i>ROM</i>	Reduced Order Model
<i>RPM</i>	Revolutions Per Minute
<i>SP</i>	Setpoint
<i>SST</i>	Shear Stress Transport
<i>TCC</i>	Temperature Control Curve
<i>UK</i>	United Kingdom

Mathematical Operators

T	Transposed
∇	Differential operator
$-$	Mean

List of Tables

1.1	Summary of modeling techniques in literature	5
1.2	Comparison of selected modeling techniques for HVAC systems (+: high, o: medium, -: low)	11
2.1	Summary of the Galerkin procedure	24
2.2	Summary of the POD procedures applied to the mixing process	37
3.1	Geometrical data of the measurement channels	44
3.2	Parameters for experimental data set	50
3.3	Important sensor hardware in the test vehicle	52
4.1	Boundary Conditions	56
4.2	Loss coefficient for different butterfly valve angles [39] applied as input for the POD	57
4.3	Loss coefficient for different butterfly valve angles [39] applied as reference to evaluate the POD models	57
4.4	Modifications to apply the HVAC model from the test rig to dif- ferent vehicles using the same HVAC unit	78
4.5	Test cases for the model validation	79
4.6	Error evaluation of the outlet temperatures modeled	90

LIST OF TABLES

5.1	Selected setpoints for the volume flow rates \dot{V}_{SP}^+	108
5.2	Selected setpoints for the outlet temperatures \mathbf{T}_{SP}	108
5.3	Estimated valve positions α^+ for the specified operating conditions	109
5.4	Measured volume flow rates and outlet temperatures at steady state	112
5.5	Estimated valve positions α^+ using the outlet quantities measured as setpoint	113
5.6	Valve positions applied for model-based control in the vehicle .	114
A.1	Summarized coefficients of the FR network model	129
A.2	Loss coefficients of the FRN	129
B.1	Expected fluctuations of the ambient air	134
B.2	Uncertainties of the measured quantities used to evaluate the error of the mass flow rates at the outlets of the HVAC unit	136
B.3	Errors of the mass flow rates at the outlets of the HVAC unit . . .	136
B.4	Technical specification of the differential pressure sensor sensirion SDP1000L provided by the manufacturer	137
B.5	Technical specification of the 3D printer and material of the printed components	138
B.6	Technical specification of the anemometers Schiltknecht Mini-Air6 Macro provided by the manufacturer	138

List of Figures

1.1	Market share of cars with HVAC systems in UK [20]	1
1.2	Schematic sketch of a representative HVAC unit	3
2.1	Schematic flowchart of the G-POD approach	21
2.2	Integral flow variables of a HVAC unit	26
2.3	Schematic flow chart of the O-POD procedure	30
3.1	Piping and instrumentation diagram of the test rig	40
3.2	Test rig	41
3.3	Bellmouth inlet nozzle for the measurement of total mass flow rate	42
3.4	Range and uncertainty $u_{\dot{m}_{tot}}$ of the total mass flow rate measured with the bellmouth inlet nozzle	43
3.5	Channel for the measurement of temperature and volume flow rates at the outlets of the HVAC unit	44
3.6	Geometry of the static blade mixer	45
3.7	Loss of total head of the mixer for varying number of elements	46
3.8	Step response of the dimensionless temperature at the left side outlet	48

3.9	Left side ventilation duct equipped with thermocouples for driving measurements	52
4.1	Two-dimensional HVAC model (orange: cell region Ω_n with flow resistance)	54
4.2	Loss of total head in a cylindrical butterfly valve	55
4.3	Flow resistance network	57
4.4	Deviation of the actual flow distribution from the mean distribution	60
4.5	Weighting coefficients for the three operating conditions of Fig 4.4	61
4.6	Change of the flow distribution introduced by the modes	62
4.7	Superposition of the weighted POD modes for the volume flow rates	62
4.8	Reconstruction of the enthalpy flow rates	64
4.9	Isolines of the temperature mean distribution (4.9a), temperature mode 1 (4.9b) and temperature mode 2 (4.9c).	65
4.10	Eigenvalue spectrum	66
4.11	Maximum and mean truncation error of the observations for the enthalpy flow rates by O-POD procedure and Galerkin method .	67
4.12	Error distribution of the O-POD procedure and dimensionless enthalpy flow rate at the defrost outlet for varying volume flow rates	68
4.13	Reference coefficients and estimated weighting coefficients by the O-POD procedure of the first (4.13a) and second mode (4.13b)	69

4.14 Reference coefficients and estimated weighting coefficients by the G-POD procedure of the first (4.14a) and second mode (4.14b)	70
4.15 Comparison of the error for the test cases between the O-POD method and the G-POD approach	71
4.16 Average time to reconstruct enthalpy and volume flow rates at the outlets	72
4.17 Sub-models and signal flow of the HVAC unit model (the numbers refer to the components in Fig. 3.1 modeled by the respective sub-model).	74
4.18 Flow resistance network of the HVAC unit	76
4.19 Nodal network of the ventilation ducts and surrounding material layers	77
4.20 Error of the dimensionless volume flow rates at the outlets	80
4.21 RIC using the original and extended data set	81
4.22 Error of the enthalpy flow rates for test case 1	82
4.23 Error of the enthalpy flow rates for test case 2	82
4.24 Absolute error of the enthalpy flow rates at the right climate zone outlets for test case 1 using the extended data set	83
4.25 Weighting coefficients a_i of the right climate zone for test case 1	85
4.26 Weighting coefficients a_i of the right climate zone for test case 2	86
4.27 Influence of the flow through the HX on the mixing process	87
4.28 Heat transfer \dot{Q}_{HX} in the HX at the left and right climate zone of the HVAC unit for test case 1	88
4.29 Heat transfer \dot{Q}_{HX} in the HX at the left and right climate zone of the HVAC unit for test case 2	88

LIST OF FIGURES

4.30	Temperature error for test case 1 using the extended data set . . .	89
4.31	Temperature error for test case 2 using the extended data set . . .	89
4.32	Comparison of the absolute temperature error for test case 1 using the extended and the original data set	90
5.1	Ambient temperature and cabin temperature during the driving cycle	94
5.2	Driving velocity during the driving cycle	95
5.3	Total air mass flow rate during the driving cycle	95
5.4	Valve positions and mass flow rates in the left climate zone . . .	97
5.5	Position of the mixing valve of the HVAC unit and the coolant inlet temperature of the HX	98
5.6	Summary of the different operating conditions during the driving cycle	99
5.7	Comparison of the measured and simulated total heat transfer of the HX	100
5.8	Face and side outlet temperatures during the driving cycle in the left climate zone of the HVAC unit	101
5.9	Outlet temperatures during the driving cycle in the left climate zone of the HVAC unit	102
5.10	Relative temperature error during driving cycle in the left climate zone of the HVAC unit	104
5.11	Standard feedback control of the HVAC unit [95]	106
5.12	Model-based control approach of the HVAC unit	107
5.13	Comparison of the simulated and measured values with the set-points for the left defrost and foot outlets	110

5.14 Comparison of the simulated and measured mass flow rates and outlet temperatures with the setpoints for the left side and face outlets	111
5.15 Velocity profile and total mass flow rate for model-based control	115
5.16 Estimated mixing valve positions α^+	116
5.17 Estimated valve positions α^+ using the outlet quantities measured as setpoints	117
5.18 Estimated valve positions α^+ using the outlet temperatures measured as setpoints	118
A.1 Energy balance applied to the blower	127
A.2 Sections of the heat exchanger	130
A.3 Efficiency of the heat exchanger	131
B.1 Relative error of the total mass flow rate	135
B.2 Calibration protocol of the thermocouples	139

1 Introduction

From the beginning of modern vehicle mobility pleasant thermal comfort is an important aspect [1]. In 1953 the first heating, ventilation and air conditioning (HVAC) systems were mainly installed in premium vehicles and sold at high price [14]. The HVAC unit was controlled by the driver and high knowledge about the system was needed to obtain thermal comfort under different operating conditions.

The market penetration of cars with HVAC system increased first in hot climate areas and from the 1990s also in colder areas as shown in Fig. 1.1 on the example of United Kingdom (UK). Nowadays almost all vehicles are sold with an HVAC system.

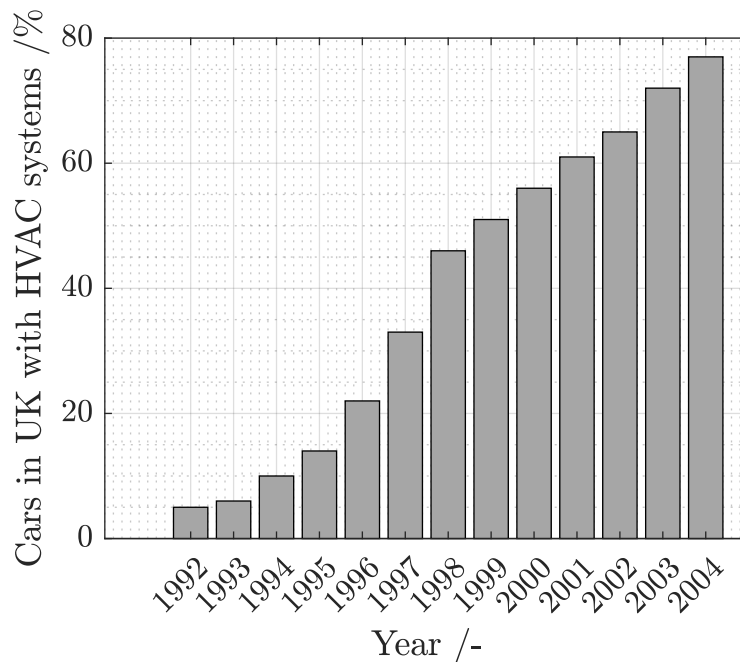


Figure 1.1: Market share of cars with HVAC systems in UK [20]

Thus, the passenger comfort has become a major aspect in the design process of cars. The customers expectations regarding the climate control system changed with growing market penetration. While initially high user experience was required to manipulate the HVAC unit, most of the current users are not willing to occupy themselves with comfort regulation but expect this to work automatically. To account for this, the first automatic climate control (ACC) was already introduced in 1964 [54]. Modern ACC receives sensor data about ambient conditions, individual inputs from the passengers, the vehicle state and the cabin temperature. Based on this information the ACC prescribes outlet temperatures of the HVAC unit as setpoints to produce pleasant thermal comfort. Thus, the ACC aims to link the passenger comfort with the thermal state of the vehicle. Given the example of low ambient temperatures (around 0 °C), the ACC would provide a setpoint for the outlet temperatures of 60 °C at the foot region but only 50 °C at the chest region as shown by the test drive in chapter 5. This is because of the different thermal sensation of the human body parts. Therefore, the air temperatures at the outlets of the HVAC unit are measured by sensors and they provide the most important variables for climate control. Beyond pleasant thermal cabin conditions, vehicle air conditioning systems must comply with legal regulations [2]. These regulations include safety-related features such as de-icing of the windshield. The interpretation of thermal comfort and the resulting control strategy to obtain pleasant conditions depends on the car manufacturer, the vehicle and the country [99]. Although the control strategy is adopted according to the markets needs, the HVAC unit remains identical for different vehicles to reduce manufacturing costs.

A HVAC unit is shown schematically in Fig. 1.2. The blower generates the air volume flow rate by moving the air in the HVAC unit. Downstream of the blower, the air flow is dehumidified and cooled down in the evaporator. Valves split the total air volume flow rate in two parts leaving the evaporator. One part is heated in the heat exchanger. The rest bypasses the heat exchanger. Both air streams are then mixed inhomogeneously in the mixing cavity such that the air temperatures at the outlets of the HVAC unit are different. Further downstream, ventilation ducts connect the outlets of the HVAC unit with the vehicle cabin.

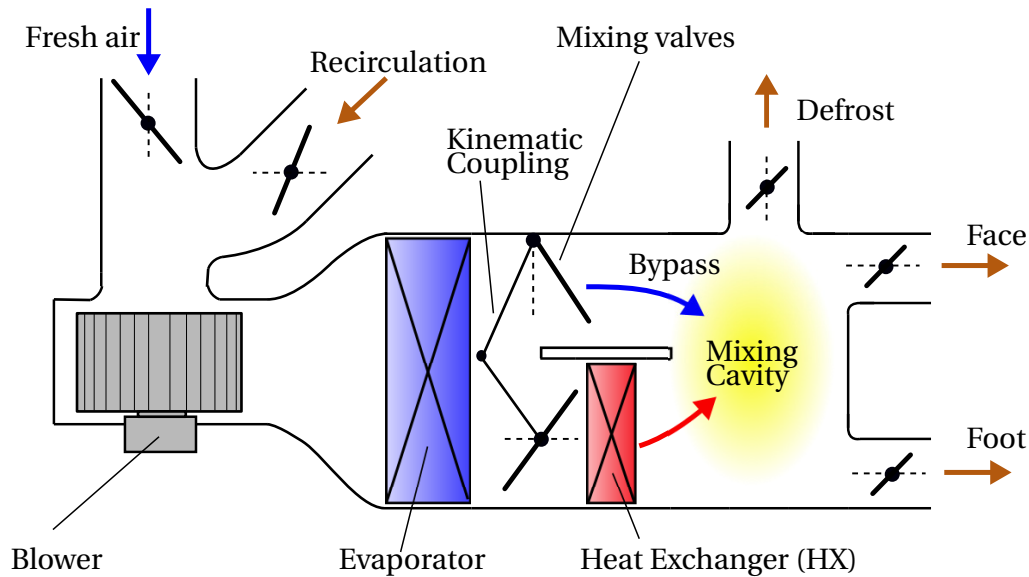


Figure 1.2: Schematic sketch of a representative HVAC unit

The temperature distribution of the air flow leaving the cavity is inhomogeneous too as a result from the inhomogeneous mixing in the cavity. This causes deviations between the bulk mean and the sensor temperature, which reduces the robustness of the climate control system. Also, these sensors essentially contribute to the manufacturing cost. Due to increasing electrification of the vehicles, energetic optimization becomes a focus in future climate control concepts and requires more efficient control strategies of the ACC [45].

A way to address these challenges is to incorporate a real-time HVAC model in the ACC. A model-based control scheme, which integrates actuator and sensor signals to model the HVAC unit, has several advantages. It allows diagnostics for sensor plausibility to increase robustness, a control strategy with energetic optimization and to eliminate sensors reducing costs.

The low-dimensional description of the HVAC unit and its functions for real-time control is subject of this work. The model should have high generalization capability for application within an industrial process. This is an important feature since the interface components between HVAC unit and passenger cabin vary greatly, depending on the design of the vehicle. Extensive measurements are not practical for the same reason. So, only a moderate amount of data is available for model calibration. Although only a few operating conditions can be used for model calibration, the model results must respect phys-

ical laws, e.g. mass conservation, for the complete operating range. Implausible values can lead to great discomfort and dissatisfied costumers. To save time and to automate the modeling procedure, no tuning of the model architecture should be required and the model should be easy to generate.

In summary, four requirements are particularly important to select a suitable model procedure. The procedure must have high generalization capability, which is important to apply the method to different vehicles. Furthermore, the model should be easy to generate without tuning of the model architecture and a moderate amount of data must be sufficient for model calibration. Finally, the model always must deliver plausible results to avoid discomfort.

1.1 State of the Art

In this section the state of knowledge is reviewed. First, modeling approaches for HVAC systems are presented and categorized. These approaches are then compared with respect to their applicability to model flow and mixing in HVAC units. Suitable modeling techniques are selected based on this comparison.

1.1.1 Overview of Modeling Approaches

HVAC modeling techniques can be divided into three different categories: *physical models*, *black-box models* and *gray-box models* [3, 4, 7]. These three model types are outlined below and relevant literature regarding HVAC systems is presented. A summary of the techniques from the reviewed literature and their application is given in Tab 1.1.

Table 1.1: Summary of modeling techniques in literature

	Physical models	Black-box models		Gray-box models
		e.g. ANN, FL, ARMAX	POD based models	
Application to HVAC systems in literature	Blower [11] Air distribution system [34, 79] Heat Exchanger [17, 29, 38, 87] Mixing cavity [17, 29, 87] Heat transfer ducts [31, 41]	Blower [23, 29] Air distribution system [6, 25] Heat Exchanger [6, 21, 25, 44] Mixing cavity [25] Heat transfer ducts [8, 25]	No application of POD reported.	Blower [33] Air distribution system [31, 83] Heat Exchanger [5, 31, 83] Mixing cavity [17, 29, 87] Heat transfer ducts [26, 36, 42, 100, 101]
Model base	Governing equations	Collected data	Collected data/ Governing equations	Collected data/ Governing equations
Data type	Not required	Input and output data	Spatially resolved flow fields	Input and output data, state variables
Model structure	Represents physical system closely	Non-physical system representation	Represents physical behavior of the system	Represents physical system closely
Model generation	Requires physical simplifications	Requires tuning of model architecture	Requires weighting procedure for POD modes	Requires physical simplifications and method for parameter optimization

Physical Models

Physical models are based on the physical laws, which govern the HVAC system. Typically the momentum, mass and energy balance are applied to model the flow and heat transfer. Physical models are mostly used to assess HVAC systems at an early design stage or to investigate control strategies.

Sambandan and Valencia [79] describe a fluid resistance network to model the airflow distribution from the HVAC outlets to the cabin. A core component of the model was the description of heat transfer in the heat exchanger for different inlet temperatures and volume flow rates of both air and coolant. A mixing model was not required, because the bypass of the HX was closed and no mixing occurred. Different concepts for HVAC systems were analyzed in Hager and Anzenberger [34] using a fluid resistance network. The fluid resistance network was coupled to a cabin model and an engine model to evaluate the heating performance of vehicle configurations. Several physical models have been developed for control purposes to quantify the heat and power consumption [16, 17, 29, 38, 48, 49, 87]. The aims of the investigated control strategies were consumption reduction, improved thermal comfort or both of them. Farzaneh and Tootoonchi [29] applied a fuzzy controller acting on a physical model to achieve thermal comfort in a vehicle cabin. The setpoint was based on the Predicted Mean Vote (PMV) index proposed by Fanger [28]. None of the cited references has addressed the effect of inhomogeneous thermal mixing on the outlet temperatures since the warm and cold inflows were considered to be perfectly mixed.

In summary it can be stated that physics-based models are often applied at an early design stage of HVAC units since no calibration data is required for model generation. HVAC concepts can be analyzed qualitatively without the need of conducting expensive measurements or simulations. They can be easily applied to different HVAC units but assumptions are required to estimate parameters of the models. For this reason, only moderate accuracy is achieved. The inhomogeneous mixing process in the HVAC unit has been simplified to homogeneous mixing of the air streams through the bypass and the HX. This does not reflect the reality as stated in the introduction.

Black-box Models

Black-box models are generated from recorded data of HVAC systems. Several techniques to process the data and to develop a mathematical correlation of the values have been proposed. Representative data-driven modeling types are data mining algorithms, Fuzzy Logic (FL) models or statistical models. An approach for the first modeling type is an Artificial Neural Network (ANN) and for the third type is an Autoregressive Moving Average Exogenous (ARMAX) model [3, 4, 7]. ANN is the most prominent technique for system identification among these data-driven methods. Traditionally, these methods are applied to input and output data of a component or the complete HVAC system [43, 66].

ANN aim to mirror brain functions in a computerized way. The model consists of connected devices, which are called neurons. The connections are weighted and summed to calculate the corresponding output. The weighting of the neurons is optimized by the training data. Kamar et al. [44] used ANN to predict the performance of the refrigerant cycle. Test rig data were used to train the ANN. Several configurations of the model architecture have been analyzed to optimize the prediction accuracy. Durovic and Kovacevic [25] applied ANN to generate an HVAC model for model-based control. The required data was collected by test drives. These test drives are usually performed during the developing process of a vehicle. The gathered data was not sufficient to generate an ANN with acceptable accuracy for climate control. Other research studies [69, 70, 88] proposed offline and online training of the ANN to handle the amount of data needed. In the offline stage an initial model is generated and the model architecture is optimized. Afterwards in the online stage the model is fed with online data to increase the accuracy. It can be stated that ANN are particularly applied if large data sets were available or can be measured. To model the HVAC unit outlined in chapter 3 with ANN and considering only the valve positions as parameters, approximately 820 days would be needed for the test rig measurements. This goes beyond an industrial applicability. No understanding of the physical HVAC system is required and the physical structure is not preserved. This results in a low generalization capability and the model structure needs to be tuned to obtain accurate model values. Consequently ANN do not meet the model requirements outlined in the introduction.

The FL method has been developed in 1968 to deal with inexact process data. The fuzzy algorithm involves if-then rules to model the system behavior qualitatively. Watanuki and Murata [94] controlled the temperature in a car cabin to provide pleasant comfort of the passengers. However, high process knowledge and data is required to apply FL models [72]. The correlation between volume flow rates and enthalpy flow rates at the outlets is very complex and unknown. Therefore, FL models are difficult to apply and are not suitable to model the mixing process in the HVAC unit.

Statistical models are based on an assumption for the probability density distribution. These models usually result in a polynomial description of the input and output correlation. Dong et al. [23] generated a polynomial function for a blower to calculate energy consumption using the fan speed signal. Mustafaraj et al. [67] compared different statistical modeling procedures to calculate the room temperature of a building. Collected data from 9 months have been used for model generation. It was shown that the effort to identify parameters for a large number of inputs and outputs of the system increases significantly. Hence, regression models are particularly suitable for a single input and output correlation [3, 7]. But, the models required for the HVAC unit (see Tab. 1.1) have multiple inputs and multiple outputs.

A method, which has not been applied yet to HVAC systems, is Proper Orthogonal Decomposition (POD) [3, 4, 7]. Lumley [62] stated that the POD has been independently discovered by different researchers, e.g. Kosambi [68] or Pearson [74]. It is also known as Karhunen-Loève-Decomposition [73], POD [15] or Principal Component Analysis (PCA) [50], among others. The basic idea remains the same although different names are used for this method [97]. Typical application fields are process monitoring [43, 76, 98], data analysis [47, 84] and fluid dynamics [12]. The POD method aims to decompose a set of observations into a series expansion of orthogonal basis functions. These basis functions are also called POD modes and only few POD modes are sufficient to describe the complete data set with high accuracy. This method has been firstly applied to image processing, e.g. face recognition [89] or data compression of static images [52]. For image processing, the pixel values of digital images are provided as observations. While the name PCA is particularly used

in the context of image processing, POD refers to the application to fluid mechanics and was introduced by Lumley [35]. In fluid mechanics, the observations are the values of the flow variables. For the classical application of the POD, each flow observation corresponds to a time instance of a dynamic flow field and the POD has been used to analyze the flow [12]. Kobayashi et al. [53] performed the POD on numerical data of a cooling fan to identify dominant structures in the pressure field. These flow structures were related further to the performance of the fan. The POD is also widely used to generate Reduced Order Models (ROM) besides the analysis of flow fields. The weighting coefficients for the POD modes of the series expansion need to be estimated for observations which are not included in the original data set. The most popular approach to calculate these coefficients is the Galerkin projection. This weighting procedure utilizes the fact that the POD modes preserve the physical characteristics of the flow observations such as mass and energy conservation. Therefore, the underlying governing equations can be exploited to restrict the values of the weighting coefficients. The Galerkin projection results in ordinary differential equations (ODE) applied to spatio-temporal flow fields [60, 93]. Ling et al. [58] used the POD-Galerkin projection to model the cabin of a vehicle. In comparison to CFD simulations the cabin model predicts the temperature distribution in the cabin within an error margin of less than 1 K. Recently, the POD-Galerkin procedure was also applied to parametric variations of a flow system. Instead of flow observations at different time instances, the observations correspond to a specific parametric variation. The Galerkin projection results in an equation system, which can be solved to obtain the weighting coefficients. Vendl et al. [90] modeled the steady flow over an air-foil at different angles of attack using the Galerkin projection. However, the Galerkin projection is limited to spatially resolved flow observations since it incorporates the Navier Stokes Equations. These flow observations are obtained from numerical simulations. Other research studies proposed interpolation methods to estimate the weighting coefficients [13, 63, 75, 82]. But interpolation methods have been reported to perform worse than the physically motivated Galerkin projection [92].

Gray-box Models

Gray-box models combine both, the physical modeling approach and data-driven black-box methods. The models represent the physical structure of the system, but its parameters are estimated based on the analysis of collected data. Therefore, an optimization procedure needs to be applied for parameter estimation. Gray-box models are often applied in combination with nodal networks to model transient heat transfer [26, 36, 42, 100, 101] or in fluid resistance networks to compute the fluid flow [31, 83]. Zhang et al. [101] modeled the refrigerant cycle of the HVAC unit for model-based control. The heat transfer coefficients were calibrated by using a single operating condition of a vehicle. It was shown that the residual mean square error is less than 10 % for different operating conditions. A similar approach has been applied by Shojaei et al. [83]. The refrigerant cycle of the HVAC system for an electric car has been modeled to analyze different strategies for the reduction of energy consumption. A Nusselt correlation was formulated to calculate the heat transfer at the air side of the evaporator. The coefficients of this correlation were obtained by a set of experimental data. Furthermore, the coolant flow was described by an hydraulic network. In the PhD thesis of Ghebru [31], the coolant flow of a vehicle's engine has been modeled by means of a resistance model. The resistances were calibrated by numerical simulations of the coolant loop. Afram and Janabi-Sharifi [5] used a physical description of a residential HVAC system to calculate the energy consumption. Parameters such as heat capacities and heat transfer coefficients were estimated from experimental data by using a least square algorithm.

It can be summarized from the literature presented above that gray-box models are often applied to increase the accuracy of physic-based models. Higher accuracy can be achieved using collected data, which cover relevant operating conditions. Also state variables can be applied and not only input and output data of the HVAC system. These models preserve the physical structure of the system and only a moderate amount of data is needed.

1.1.2 Selection of Modeling Techniques

Table 1.2 summarizes the modeling techniques presented before and ranks them with respect to the requirements regarding the model procedure stated in the introduction. As discussed above, physical models are very powerful if a sufficiently generalized description can be formulated. The accuracy of these models can be tuned by incorporating a moderate amount of data.

An example is the heat exchanger where zero- or one-dimensional energy balances can be used together with correlations of the convective heat transfer [78]. Furthermore, during the design of a vehicle performance data of the heat exchanger is recorded. From these measurements the heat transfer can be estimated as an alternative to correlations from literature. This leads to a scalable and flexible model, which is robust against large geometrical variations. The same can be stated for the blower. Therefore, these components are described by energy balances in this thesis.

The mass flow rate distribution has been proven to allow quasi-one-dimensional simplification. Downstream of the evaporator particularly the flow resistance of the valves, the heat exchanger and the ventilation ducts dominate the distribution of the air flow. These valves are located in the ventilation ducts. The dynamic pressures in the ducts are comparatively high due to the large ratio of area change A_{Cavity}/A_{Duct} between mixing cavity and duct. Therefore, the loss of total head in the mixing cavity $\Delta p_{t,Cavity}$ is very low in comparison to the losses induced by the components listed above and is considered to be negligible. Correlations for valve losses have been comprehen-

Table 1.2: Comparison of selected modeling techniques for HVAC systems (+: high, o: medium, -: low)

Model type	Generalization capability	Ease of model generation	Amount of needed data	Physical behavior	Applicability to mixing process
ANN	-	o	-		✓
POD based	o	+	o	✓	✓
Gray-box	o	+	o	✓	
Physical	+	o	+	✓	
Requirement	+	+	o	✓	✓

sively investigated and documented in literature. The pressure loss of the ventilation ducts and heat exchanger is a performance indicator for the design process and measured by the car manufacturers. These measurements and the correlations for the valve loss can be applied to generate a flexible and robust model. Modifications of the vehicle design easily can be accounted by adjusting the loss coefficient of the respective component.

Transient heat transfer is considered to be mainly determined by the surrounding dashboard geometry of the ventilation ducts. A one dimensional discretization of this geometry has been shown to provide good approximations for the heat transfer between vehicle structure and air flow [31, 59]. The discretization of the geometry by layers is referred as nodal network according Incropera et al. [41]. Well-correlated heat transfer coefficients can be used to model the transient behavior of outlet temperatures. Therefore, a nodal network provides high flexibility for an application to different vehicles.

In summary, an energy balance is applied to model the blower and the heat exchanger. Furthermore, a nodal network of thermal resistances and capacities of the ventilation ducts is generated to calculate the heat transfer to the vehicle structure. The air flow in the HVAC unit is described by a fluid resistance network model.

The inhomogeneous mixing process in the mixing cavity of the HVAC unit can not be described by these physical approaches mentioned above. Nevertheless, a physical framework to model the mixing process would be preferable since it requires less measurement data. One method, which maintains the physical behavior of the system and allows a physical modeling framework, is the POD. However, POD so far has been applied to spatial flow fields. The application of the POD to the outlet values has not been discussed in literature. But this application is particularly interesting because only the integral enthalpy flow rates are needed for climate control. Furthermore, these values can be acquired easily from experiments eliminating the need of numerical simulations. Coupling well established physical model approaches with the POD is a remaining knowledge gap.

1.2 Goal and Structure of the Thesis

The goal of this thesis is to create a Reduced Order Model of the mixing process based on POD. Furthermore, the aim is to develop the methodology to combine this POD model with a first principle system simulation of a HVAC unit for climate control. The input data for the POD is the system response for selected parameter combinations of the HVAC unit, which cover the relevant operating range. The traditional application of the POD-Galerkin (G-POD) projection models the high dimensional flow fields based on a set of numerical simulations using the selected parameter combinations. From the modeled flow fields, integral values are calculated. But, these simulations are very time consuming and only the outlet values are needed for climate control. Considering practical application, the ROM should solely require measured data of control-relevant output values of the HVAC unit. These output values are the volume flow rates and enthalpy flow rates at the outlets. Therefore, a new weighting procedure is developed, which focuses only on the information needed for climate control. This procedure is known as Output-based POD (O-POD).

The evaluation of the proposed O-POD approach and application to automotive climate control covers three essential steps:

1. The development of the O-POD approach based on the fundamentals of the POD procedure and Galerkin projection.
2. The integration of the O-POD procedure in a HVAC system simulation using experimental calibration data from a test rig and assessment of the resulting model with experimental validation data.
3. The application of the validated model to a real driving scenario and the presentation of a model-based control scheme.

This thesis is structured according to these steps. In chapter 2, the basics of POD are explained. The theoretical background is necessary to understand the O-POD approach, which is derived by inspecting the traditional POD

Galerkin method. In the following chapter 3, the experimental setup and measurement procedure are introduced. The measurements are needed to acquire experimental data of selected operating conditions as input for the O-POD procedure. Furthermore, the same setup is used to generate comprehensive validation data. Then in chapter 4, the O-POD approach is evaluated. This chapter is divided into two main parts: First, the O-POD approach is applied to a numerical benchmark model and assessed with reference simulations. Second, the O-POD approach is used to model mixing in the real HVAC unit. The CFD model in the first part is needed to obtain a consistent data set, which has a complexity similar to the real HVAC unit, without experimental uncertainties. Deviations between the predicted values and the reference simulations can be traced back to the O-POD approach. For this purpose, the volume flow rates and enthalpy flow rates are computed from a set of numerical simulations as input for the O-POD. The traditional Galerkin projection is also applied to the numerical benchmark model and the differences between O-POD and POD-Galerkin are demonstrated. As the O-POD approach shows good results, the procedure is applied to the real HVAC system in the second part of chapter 4. The measurement data of chapter 3 is provided as input to generate the O-POD model for the real mixing cavity in the HVAC unit. The resulting O-POD model is then integrated into a system simulation of the HVAC unit. Experimental validation data is used for the model assessment in this chapter. Afterwards, the HVAC model developed in chapter 4 is applied in chapter 5 to a driving cycle and the model performance under real operating conditions is evaluated. Finally, the HVAC model is incorporated in a model-based control scheme to eliminate the need of expensive temperature sensors. This thesis ends with a summary and conclusions of the major results in chapter 6.

2 Proper Orthogonal Decomposition

The Proper Orthogonal Decomposition (POD) method is introduced to model the mixing process in HVAC units in this chapter. The POD method requires measurements or numerical data of selected operating conditions as input and delivers a series expansion of POD modes as output. This series expansion is the basis for the POD model approach. Therefore, the fundamentals of the POD are given in section 2.1. The modes need to be weighted to generate a Reduced Order Model of the mixing process. Two weighting procedures are introduced: The POD-Galerkin projection (G-POD) and the Output-based POD (O-POD). The G-POD procedure is presented in section 2.2. This method is usually applied in literature to model high dimensional flow fields as described in the first part of the section. The G-POD method is also capable to model only the volume flow rates and enthalpy flow rates by using integral balances of the flow in the HVAC unit. This application of the Galerkin procedure is discussed in the second part of section 2.2 to understand the output based POD (O-POD) method and the differences between the two weighting procedures. In the next section 2.3, the O-POD is introduced. This method focuses solely on the integral outlet values of the HVAC unit. For the O-POD method, measurements can be used and numerical data is not required. First, the general procedure of the O-POD is presented. Then, the application to the mixing process in HVAC units is discussed. A summary and comparison of both weighting procedures is given in the last section.

2.1 Introduction to Proper Orthogonal Decomposition

The POD generates a series expansion of orthogonal basis functions. The basis functions are needed for the G-POD method and O-POD approach. However, the general POD procedure remains identical for both methods.

The difference is only the data base provided as input for the POD. Therefore, the basic definitions and the generalized POD procedure is explained in this section.

A system is considered where observations $\boldsymbol{\varphi}^{(m)}$ can be made. The observation $\boldsymbol{\varphi}^{(m)}$ is a vector of N_x values of the systems state taken at the same instance m

$$\boldsymbol{\varphi}^{(m)} = [\varphi(s_1), \varphi(s_2), \dots, \varphi(s_{N_x})]^{(m)}. \quad (2.1)$$

Considering a time varying system, the instance is the time m at which the observed N_x values are acquired at a location \mathbf{s} . An observation could be pixel values of a digital image in a sequence of frames. Given this example, the number of observed values N_x is the number of pixels in the image. More generally, the instance m refers to a parameter combination of a system. In the present work, each instance is a combination of valve positions. The objective of the POD is the optimal approximation of such an observation $\boldsymbol{\varphi}^{(m)}$ from the entire ensemble of N_s observations by orthogonal basis functions $\boldsymbol{\theta}_i$, or so-called POD modes

$$\boldsymbol{\theta}_i = [\theta(s_1), \theta(s_2), \dots, \theta(s_{N_x})]_i. \quad (2.2)$$

The number N_s refers to the number of instances or parameter combinations at which observations $\boldsymbol{\varphi}^{(m)}$ are obtained. The basis function $\boldsymbol{\theta}_i$ is again a vector of N_x values and with orthogonality follows $\boldsymbol{\theta}_i \boldsymbol{\theta}_j = 0$ for $i \neq j$. Accordingly, the observation $\boldsymbol{\varphi}^{(m)}$ can be expressed by

$$\boldsymbol{\varphi}^{(m)} = \sum_{i=1}^{N_s} a_i^{(m)} \boldsymbol{\theta}_i. \quad (2.3)$$

In Eq. 2.3, $a_i^{(m)}$ is the weighting coefficient of the i -th mode and the current observation m . The coefficients $a_i^{(m)}$ result for a mode i to

$$\mathbf{a}_i^{(m)} = [a_i^{(1)} \quad a_i^{(2)} \quad \dots \quad a_i^{(N_s)}]^T. \quad (2.4)$$

The POD modes are generated from the ensemble of N_s observations. First, the autocorrelation tensor \mathbf{R} of the observations is computed. This results in a N_x -by- N_x matrix

$$\mathbf{R} = \frac{1}{N_s} \sum_{m=1}^{N_s} \boldsymbol{\varphi}^{(m)} [\boldsymbol{\varphi}^{(m)}]^T = \frac{1}{N_s} \sum_{m=1}^{N_s} \begin{bmatrix} \varphi(s_1) \\ \vdots \\ \varphi(s_{N_x}) \end{bmatrix}^{(m)} [\varphi(s_1) \cdots \varphi(s_{N_x})]^{(m)}. \quad (2.5)$$

Second, an eigenvalue problem can be solved for the direct calculation of the basis function $\boldsymbol{\theta}_i$

$$\mathbf{R}\boldsymbol{\theta}_i = \lambda_i \boldsymbol{\theta}_i, \quad (2.6)$$

where λ_i refers to the eigenvalue of the respective POD mode. A detailed derivation of Eq. 2.6 is given in [35, 37]. The computational effort and memory to solve the eigenvalue problem of a N_x -by- N_x matrix is a formidable task and quickly exceeds the limits of practical application for a large number of states N_x , e.g. for numerical simulations.

To perform the POD with few N_s observations of high-dimensional size N_x , the Method of Snapshots was presented by Sirovich [86]. In this method, the observations are called snapshots. In literature, snapshots refer usually to flow observations at different time instances, e.g. different time steps of Large Eddy Simulations (LES). But in the present work, the observations are gathered based on selected valve positions to cover the relevant operating range of the HVAC unit. Therefore, the term snapshot is not used to describe the data set for the POD in the following. The idea of the Method of Snapshots is to first calculate the weighting coefficients $a_i^{(m)}$ and to compute the POD modes afterwards using these weighting coefficients [71]. The calculation of the POD modes yields again an eigenvalue problem

$$\mathbf{C}a_i^{(m)} = \lambda_i a_i^{(m)}. \quad (2.7)$$

The correlation tensor \mathbf{C} is calculated from the inner product of the different

instances m and follows to

$$\mathbf{C} = \frac{1}{N_s} [\boldsymbol{\varphi}^{(m)}, \boldsymbol{\varphi}^{(n)}] = \frac{1}{N_s} [\varphi(s_1) \cdots \varphi(s_{N_x})]^{(m)} \begin{bmatrix} \varphi(s_1) \\ \vdots \\ \varphi(s_{N_x}) \end{bmatrix}^{(n)}, \quad (2.8)$$

where $m, n = 1$ to N_s . The size of the correlation tensor \mathbf{C} scales now with the number of observations N_s and not with the number of observed states N_x . Therefore, the Method of Snapshots is applied in particular with Computational Fluid Dynamics (CFD) since the number of observations is much smaller than the number of system states: $N_s \ll N_x$. The POD modes are then generated by using the weighting coefficients

$$\boldsymbol{\theta}_i = \frac{1}{\sqrt{N_s \lambda_i}} \sum_{m=1}^{N_s} a_i^{(m)} \boldsymbol{\varphi}^{(m)}. \quad (2.9)$$

A maximum of N_s POD modes can be calculated from Eq. 2.9. But in practice, the series expansion is truncated after N_r modes since the first few modes cover most of the information provided by the observations. The Relative Information Content (RIC) is calculated for this purpose. The RIC is a measure for the cumulative information content of the POD series expansion by increasing the number of eigenfunctions. First, the eigenvalues are sorted in descending order of magnitude $\lambda_1 > \lambda_2 > \dots$ and then the RIC is calculated by

$$RIC(N_r) = \frac{\sum_{i=1}^{N_r} \lambda_i}{\sum_{j=1}^{N_s} \lambda_j}. \quad (2.10)$$

With respect to the HVAC application, the extension of the series expansion with the mean average is of advantage, since the mean value can be often estimated from basic conservation laws. The difference between the mean average of the entire ensemble and the observations is calculated and provided as input data set for the POD. As a result, both the input data set and the modes correspond to a deviation from the mean average, which is a more generalized approach for a given set of instances. The mean average is introduced as ze-

roth mode $\boldsymbol{\theta}_0$ with a weighting coefficient of $a_0^{(m)} = 1$. Accordingly, the mode $\boldsymbol{\theta}_0$ describes the mean of the observation ensemble, while the POD modes compute the deviation from the mean values for the actual observation

$$\tilde{\boldsymbol{\varphi}}^{(m)} = a_0^{(m)} \boldsymbol{\theta}_0 + \sum_{i=1}^{N_r} a_i^{(m)} \boldsymbol{\theta}_i = \sum_{i=0}^{N_r} a_i^{(m)} \boldsymbol{\theta}_i \quad (2.11)$$

with $N_r < N_s$ and

$$\boldsymbol{\theta}_0 = \frac{1}{N_s} \sum_{m=1}^{N_s} \boldsymbol{\varphi}^{(m)}. \quad (2.12)$$

The POD modes remain constant for a given set of input data. To reconstruct a parameter combination m , only the weighting coefficients need to be modified. In Eq. 2.7 it can be seen that the weighting coefficients of the POD modes are known for the observations. Instances, which are not included in the ensemble of observations, need to be determined. Estimating the weighting coefficients for a parameter combination m , e.g. a combination of valve positions, is the objective of the G-POD method and the O-POD approach.

2.2 Galerkin Projection (G-POD)

The basics of the Galerkin projection are explained in this section. The general procedure is presented below. In the first part of this section, the traditional application to model the high dimensional flow field of the numerical benchmark model from section 4.1 is discussed. Based on these fundamentals, the Galerkin method applied to integral balances of the HVAC unit is briefly introduced in the second part of this section. This is necessary to derive the O-POD approach in the next section 2.3 and to understand the differences between both methods.

The general idea of G-POD is to use the governing equations of a system to generate a ROM. Since the basis functions $\boldsymbol{\theta}_i$ are constructed from the observations (see Eq. 2.9), the modes preserve the physical behavior of the system, e.g. mass or energy conservation. This allows to incorporate them into the governing equations, which describe the system. Suppose that the values of the

observations $\boldsymbol{\varphi}^{(m)}$ are the values of the variables from a governing equation $\mathcal{N}[\boldsymbol{\varphi}]$. These variables can be substituted by the series expansion of Eq. 2.3

$$\mathcal{N}[\boldsymbol{\varphi}] \approx \mathcal{N}\left[\sum_{i=0}^{N_r} a_i \boldsymbol{\theta}_i\right]. \quad (2.13)$$

Instead of projecting the solution of the governing equation onto the POD modes $\boldsymbol{\theta}_i$ to obtain the weighting coefficients, the operator \mathcal{N} is projected

$$(\boldsymbol{\varphi}, \boldsymbol{\theta}_i) \longrightarrow \left(\mathcal{N}\left[\sum_{j=0}^{N_r} a_j \boldsymbol{\theta}_j\right], \boldsymbol{\theta}_i\right). \quad (2.14)$$

A system of N_r equations is generated based on Eq. 2.14 and can be solved. The estimated weighting coefficients \tilde{a}_i are obtained as the result. Subsequently, the real coefficient a_i is replaced with the estimated coefficient \tilde{a}_i and the reconstructed observation follows to

$$\tilde{\boldsymbol{\varphi}} = \sum_{i=0}^{N_r} \tilde{a}_i \boldsymbol{\theta}_i. \quad (2.15)$$

A schematic flowchart of the Galerkin procedure is shown in Fig. 2.1.

2.2.1 Application to Flow Fields in HVAC Units

Now, the flow in a HVAC unit is considered and the values of observations $\boldsymbol{\varphi}^{(m)}(\mathbf{x})$ are the flow variables at the location \mathbf{x} of the domain Ω . The Galerkin procedure is applied to the steady Reynolds-Averaged-Navier-Stokes (RANS) and scalar transport equations. Both equations are required to model scalar mixing in the turbulent flow of the mixing cavity. The traditional G-POD approach requires numerical simulations and uses the Navier-Stokes equations to model the flow field. The needed observations are CFD simulations of different valve positions.

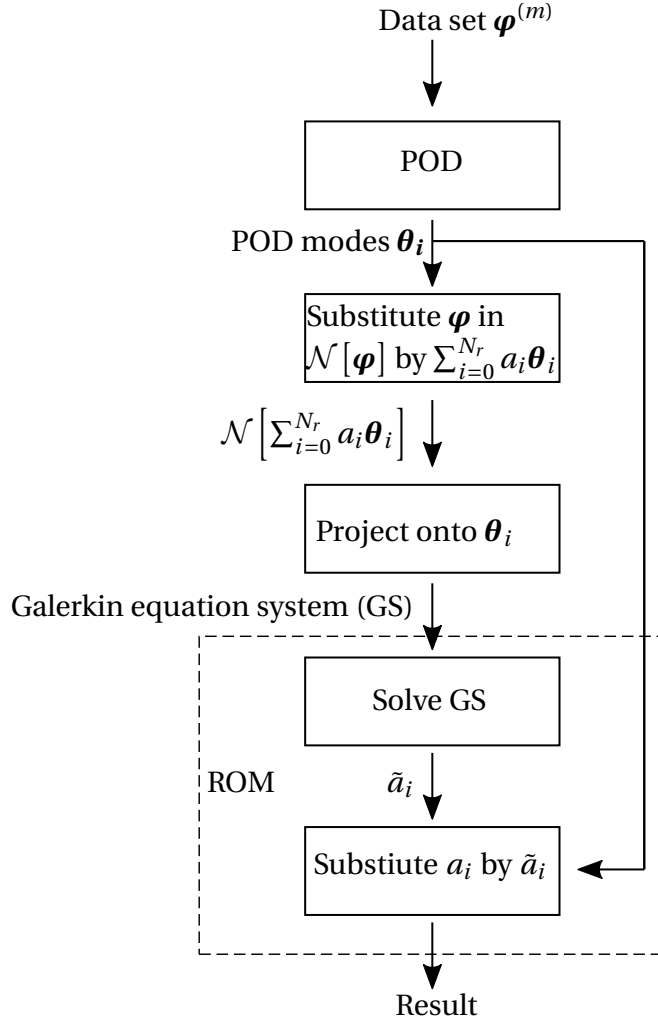


Figure 2.1: Schematic flowchart of the G-POD approach

The operator of the governing equations reads for the RANS equations

$$\mathcal{N}_I := \quad 0 = (\mathbf{u} \cdot \nabla) \mathbf{u} - \nabla \cdot [\nu_{\text{eff}} (\nabla \mathbf{u} + (\nabla \mathbf{u})^T)] + \nabla \frac{p}{\rho} + \mathbf{S}, \quad (2.16a)$$

$$0 = \nabla \cdot \mathbf{u} \quad (2.16b)$$

and for the scalar transport equation

$$\mathcal{N}_{II} := \quad 0 = (\mathbf{u} \cdot \nabla) T - \nabla \cdot [(D + D_t) (\nabla T)]. \quad (2.17)$$

In the momentum Eq. 2.16a \mathbf{S} refers to an arbitrary source term. This source term is used at the end of this subsection to model different valve positions. The effective viscosity ν_{eff} is the sum of the kinematic molecular viscosity ν

and the turbulent apparent viscosity ν_t

$$\nu_{\text{eff}} = \nu + \nu_t. \quad (2.18)$$

For incompressible and laminar flows, the POD is only applied to the velocity field and the variables have the same dimension. But the state vector of the flow field from Eq. 2.16a and 2.17 consists of the velocities \mathbf{u} , pressure p , effective viscosity ν_{eff} and temperature T . In a straightforward application of the Method of Snapshots outlined in section 2.1, one notes that the inner product of Eq. 2.8 is not consistent for different flow quantities. This is because the units may not agree. The most common approach to cope with the dimensionality of the flow quantities is to use vector-valued modes with an appropriate scaling of the variables. The flow quantities of the spatially distributed field variables $\boldsymbol{\varphi}(\mathbf{x})$ are scaled by nominal values as follows

$$\boldsymbol{\varphi}^+(\mathbf{x}) = \begin{pmatrix} \mathbf{u}^+(\mathbf{x}) \\ p^+(\mathbf{x}) \\ \nu_t^+(\mathbf{x}) \\ T^+(\mathbf{x}) \end{pmatrix} = \begin{pmatrix} \mathbf{u}(\mathbf{x})/U_0 \\ p(\mathbf{x})/U_0^2 \\ \nu_t(\mathbf{x})/(U_0L) \\ (T(\mathbf{x}) - T_{\min})/(T_{\max} - T_{\min}) \end{pmatrix}. \quad (2.19)$$

The state vector of the flow field in Eq. 2.19 is expanded in a series expansion of vector-valued POD modes

$$\boldsymbol{\varphi}^+(\mathbf{x}) = \begin{pmatrix} \mathbf{u}^+(\mathbf{x}) \\ p^+(\mathbf{x}) \\ \nu_t^+(\mathbf{x}) \\ T^+(\mathbf{x}) \end{pmatrix} \approx \begin{pmatrix} \tilde{\mathbf{u}}^+(\mathbf{x}) \\ \tilde{p}^+(\mathbf{x}) \\ \tilde{\nu}_t^+(\mathbf{x}) \\ \tilde{T}^+(\mathbf{x}) \end{pmatrix} = \sum_{i=0}^{N_r} a_i \begin{pmatrix} \boldsymbol{\theta}_i^u(\mathbf{x}) \\ \theta_i^p(\mathbf{x}) \\ \theta_i^{\nu_t}(\mathbf{x}) \\ \theta_i^T(\mathbf{x}) \end{pmatrix}. \quad (2.20)$$

The POD modes $\boldsymbol{\theta}_i$ can be substituted in the operator \mathcal{N}_I and \mathcal{N}_{II} and the terms of the governing equations are projected on the subspace spanned by the POD modes.

For better understanding, the Galerkin procedure is demonstrated in detail by an example using the convection term of the RANS equation. First, the series expansion in Eq. 2.20 is substituted into the governing equations.

Applied to the convection term this leads to

$$\begin{aligned}
 (\mathbf{u} \cdot \nabla) \mathbf{u} &\approx (a_0 \boldsymbol{\theta}_0^{\mathbf{u}} \cdot \nabla) a_0 \boldsymbol{\theta}_0^{\mathbf{u}} + (a_0 \boldsymbol{\theta}_0^{\mathbf{u}} \cdot \nabla) a_1 \boldsymbol{\theta}_1^{\mathbf{u}} + \dots \\
 &\quad + (a_{N_r} \boldsymbol{\theta}_{N_r}^{\mathbf{u}} \cdot \nabla) a_{N_r} \boldsymbol{\theta}_{N_r}^{\mathbf{u}} \\
 &= a_0 a_0 (\boldsymbol{\theta}_0^{\mathbf{u}} \cdot \nabla) \boldsymbol{\theta}_0^{\mathbf{u}} + a_0 a_1 (\boldsymbol{\theta}_0^{\mathbf{u}} \cdot \nabla) \boldsymbol{\theta}_1^{\mathbf{u}} + \dots \\
 &\quad + a_{N_r} a_{N_r} (\boldsymbol{\theta}_{N_r}^{\mathbf{u}} \cdot \nabla) \boldsymbol{\theta}_{N_r}^{\mathbf{u}} \\
 &= \sum_{j=0}^{N_r} \sum_{k=0}^{N_r} a_j a_k (\boldsymbol{\theta}_j^{\mathbf{u}} \cdot \nabla) \boldsymbol{\theta}_k^{\mathbf{u}}.
 \end{aligned} \tag{2.21}$$

Subsequently, the terms with the substituted POD modes can be projected onto the POD subspace by calculating the inner product of the respective term and POD mode.

The projected convection term with the substituted POD modes of Eq. 2.21 yields

$$\begin{aligned}
 &\left[\sum_{j=0}^{N_r} \sum_{k=0}^{N_r} a_j a_k (\boldsymbol{\theta}_j^{\mathbf{u}} \cdot \nabla) \boldsymbol{\theta}_k^{\mathbf{u}}, \boldsymbol{\theta}_i^{\mathbf{u}} \right]_{\Omega} = \\
 &\sum_{j=0}^{N_r} \sum_{k=0}^{N_r} a_j a_k \left[(\boldsymbol{\theta}_j^{\mathbf{u}} \cdot \nabla) \boldsymbol{\theta}_k^{\mathbf{u}}, \boldsymbol{\theta}_i^{\mathbf{u}} \right]_{\Omega} = \\
 &\sum_{j=0}^{N_r} \sum_{k=0}^{N_r} a_j a_k \mathcal{C}_{ijk}.
 \end{aligned} \tag{2.22}$$

with

$$\mathcal{C}_{ijk} = \begin{pmatrix} \mathcal{C}_{000} & \dots & \mathcal{C}_{0N_r N_r} \\ \mathcal{C}_{100} & \dots & \mathcal{C}_{1N_r N_r} \\ \vdots & \vdots & \vdots \\ \mathcal{C}_{N_r 00} & \dots & \mathcal{C}_{N_r N_r N_r} \end{pmatrix} = \begin{pmatrix} [(\boldsymbol{\theta}_0^{\mathbf{u}} \cdot \nabla) \boldsymbol{\theta}_0^{\mathbf{u}}, \boldsymbol{\theta}_0^{\mathbf{u}}]_{\Omega} & \dots & [(\boldsymbol{\theta}_{N_r}^{\mathbf{u}} \cdot \nabla) \boldsymbol{\theta}_{N_r}^{\mathbf{u}}, \boldsymbol{\theta}_0^{\mathbf{u}}]_{\Omega} \\ [(\boldsymbol{\theta}_0^{\mathbf{u}} \cdot \nabla) \boldsymbol{\theta}_0^{\mathbf{u}}, \boldsymbol{\theta}_1^{\mathbf{u}}]_{\Omega} & \dots & [(\boldsymbol{\theta}_{N_r}^{\mathbf{u}} \cdot \nabla) \boldsymbol{\theta}_{N_r}^{\mathbf{u}}, \boldsymbol{\theta}_1^{\mathbf{u}}]_{\Omega} \\ \vdots & \vdots & \vdots \\ [(\boldsymbol{\theta}_0^{\mathbf{u}} \cdot \nabla) \boldsymbol{\theta}_0^{\mathbf{u}}, \boldsymbol{\theta}_{N_r}^{\mathbf{u}}]_{\Omega} & \dots & [(\boldsymbol{\theta}_{N_r}^{\mathbf{u}} \cdot \nabla) \boldsymbol{\theta}_{N_r}^{\mathbf{u}}, \boldsymbol{\theta}_{N_r}^{\mathbf{u}}]_{\Omega} \end{pmatrix}. \tag{2.23}$$

Each term of the governing equation \mathcal{N}_I and \mathcal{N}_{II} results in a matrix as shown for the convection term. The entries of the respective matrices are summarized in Tab. 2.1

Table 2.1: Summary of the Galerkin procedure

Matrix symbol	Interpretation of term	Term in equation	Galerkin projection	Galerkin system
RANS Eq. 2.16a				
C_{ijk}	Convection	$0 = (\mathbf{u} \cdot \nabla) \mathbf{u}$	$0 = \sum_{j=0}^{N_r} \sum_{k=0}^{N_r} a_j a_k \left((\boldsymbol{\theta}_j^{\mathbf{u}} \cdot \nabla) \boldsymbol{\theta}_k^{\mathbf{u}} \boldsymbol{\theta}_i^{\mathbf{u}} \right)_{\Omega}$	$0 = \sum_{j=0}^{N_r} \sum_{k=0}^{N_r} a_j a_k C_{ijk}$
T_{ijk}	Viscous stresses	$-\nabla \cdot [\nu_{\text{eff}} (\nabla \mathbf{u} + (\nabla \mathbf{u})^T)]$	$-\sum_{j=0}^{N_r} \sum_{k=0}^{N_r} a_j a_k \left(\nabla \cdot \left[\left(\boldsymbol{\theta}_j^{\nu_i} + \frac{1}{Re} \right) (\nabla \boldsymbol{\theta}_k^{\mathbf{u}} + (\nabla \boldsymbol{\theta}_k^{\mathbf{u}})^T) \right], \boldsymbol{\theta}_i^{\mathbf{u}} \right)_{\Omega}$	$-\sum_{j=0}^{N_r} \sum_{k=0}^{N_r} a_j a_k T_{ijk}$
P_{ij}	Pressure	$+\nabla \frac{p}{\rho}$	$+\sum_{j=0}^{N_r} a_j \left(\nabla \theta_j^p, \boldsymbol{\theta}_i^{\mathbf{u}} \right)_{\Omega}$	$+\sum_{j=0}^{N_r} a_j P_{ij}$
S_{ijk}	Source	$+\frac{1}{2} F_n \mathbf{u} \mathbf{u}$	$+\sum_{j=0}^{N_r} \sum_{k=0}^{N_r} a_j a_k \left(\frac{1}{2} F_n L \boldsymbol{\theta}_k^{\mathbf{u}} \boldsymbol{\theta}_j^{\mathbf{u}}, \boldsymbol{\theta}_i^{\mathbf{u}} \right)_{\Omega}$	$+F_n \sum_{j=1}^{N_r} \sum_{k=0}^{N_r} a_j a_k S_{ijk}$
Continuity Eq. 2.16b				
M_{ij}	Divergence	$0 = \nabla \cdot \mathbf{u}$	$0 = \sum_{j=0}^{N_r} a_j \left(\nabla \cdot \boldsymbol{\theta}_j^{\mathbf{u}}, \theta_i^p \right)_{\Omega}$	$0 = \sum_{j=0}^{N_r} a_j M_{ij}$
Scalar transport Eq. 2.17				
B_{ijk}	Convection	$0 = (\mathbf{u} \cdot \nabla) T^+$	$0 = \sum_{j=0}^{N_r} \sum_{k=0}^{N_r} a_j a_k \left((\boldsymbol{\theta}_k^{\mathbf{u}} \cdot \nabla) \theta_j^T, \theta_i^T \right)_{\Omega}$	$0 = \sum_{j=0}^{N_r} \sum_{k=0}^{N_r} a_j a_k B_{ijk}$
D_{ijk}	Diffusion	$-\nabla \cdot [(D + D_f) (\nabla T^+)]$	$-\sum_{j=0}^{N_r} \sum_{k=0}^{N_r} a_j a_k \left(\nabla \cdot \left[\left(\frac{1}{Pr_t} \theta_j^{\nu_i} + \frac{1}{ReSc} \right) (\nabla \theta_k^T) \right], \theta_i^T \right)_{\Omega}$	$-\sum_{j=0}^{N_r} \sum_{k=0}^{N_r} a_j a_k D_{ijk}$

Incorporating Boundary Conditions

Since the aim of the G-POD is to generate a ROM for different valve positions of the HVAC unit, these parameters need to be incorporated in the Galerkin System. In the real HVAC unit, the operating conditions are specified by valve positions or the total mass flow rate. Different approaches have been presented in literature to account for parameter variations [46, 85]. However, only different valve positions were considered to evaluate the POD models with numerical data in section 4.1. Instead of physically modeling the valves, a flow resistance is applied to a specific sub-domain of the numerical model to regulate the flow field. The flow resistance \mathbf{S} describes a pressure drop proportional to the squared velocity. It can be computed by

$$\mathbf{S} = \frac{1}{2} F_n |\mathbf{u}| \mathbf{u}, \quad (2.24)$$

where F_n is the scaling factor of the resistance for the sub-domain n .

As a final result of the Galerkin projection, the Galerkin system of the steady RANS and scalar transport equations can be written as

$$\begin{aligned} \text{Momentum Eq.} \quad & \sum_{j=0}^{N_r} \sum_{k=0}^{N_r} a_j a_k (C_{ijk} - \mathcal{T}_{ijk} + F_n \mathcal{S}_{ijk}) \\ & + \sum_{j=0}^{N_r} a_j \mathcal{P}_{ij} \\ & = 0, \end{aligned} \quad (2.25)$$

$$\text{Continuum Eq.} \quad \sum_{j=0}^{N_r} a_j \mathcal{M}_{ij} = 0,$$

$$\text{Scalar transport Eq.} \quad \sum_{j=0}^{N_r} \sum_{k=0}^{N_r} a_j a_k (\mathcal{B}_{ijk} - \mathcal{D}_{ijk}) = 0.$$

The Galerkin system can be solved iteratively. In the present work, Newton's method is applied. The solution of the Galerkin System leads to the estimated weighting coefficients \tilde{a}_i . These coefficients are further used to reconstruct the complete flow field from which integral volume flow rates and enthalpy flow rates are computed by

$$\dot{V}_n = \int_{\Gamma} u dA, \quad (2.26a)$$

$$\dot{H}_n = \rho c_p \int_{\Gamma} u T dA, \quad (2.26b)$$

where n corresponds to the respective outlet (e.g. defrost).

In summary, the Galerkin projection applied to RANS results in a ROM of the high dimensional flow fields for the temperature, velocity, etc.. Therefore, this application is in particular suitable if the distribution of the flow variables, e.g. a temperature profile at the outlet, is required. However, the Galerkin projection can also be applied to integral values as described in the following subsection.

2.2.2 Application to Integral Balances of HVAC Units

Particularly the volume flow rates and enthalpy flow rates are important for climate control. The application of the Galerkin projection to these values is explained below. This is necessary to derive the O-POD approach in the next section and to understand the link between both weighting methods.

In Fig. 2.2 the most important components and values to model the flow in the HVAC unit are shown. In this figure, integral volume flow rates are denoted by \dot{V} and enthalpy flow rates by \dot{H} . The density ρ_0 is considered to be constant for the sake of simplicity. In Fig. 2.2, p_t is the total pressure at a specific location. In particular, the pressure at the inlet cross section $p_{t,0}$, in the mixing

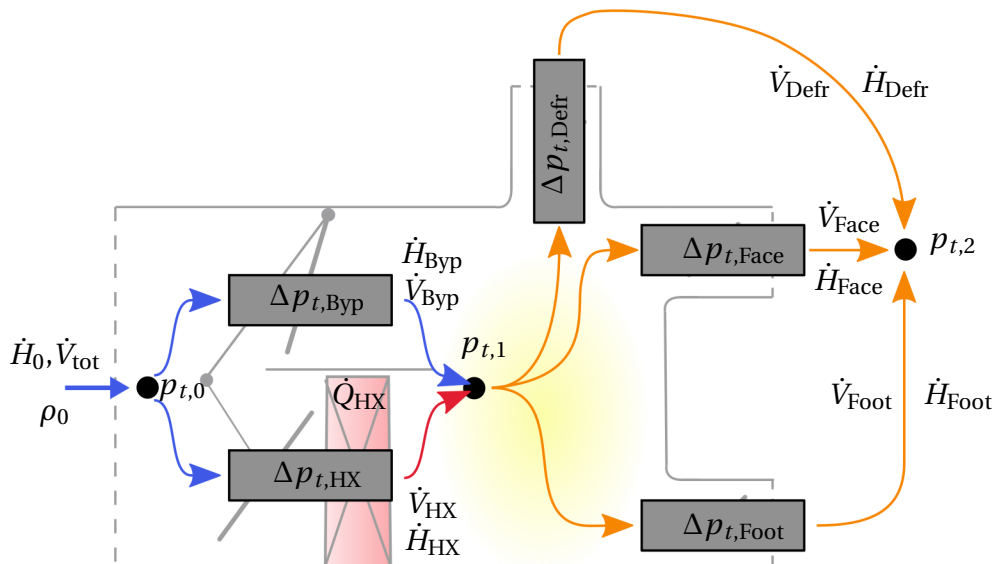


Figure 2.2: Integral flow variables of a HVAC unit

cavity $p_{t,1}$ and in the vehicle cabin $p_{t,2}$ are important. Furthermore, the flow path through the HVAC unit is shown. The total pressure drop introduced by a component i , e.g. a valve, is described by $\Delta p_{t,i}(\zeta_i, \dot{V}_i)$. The pressure drop depends on a loss coefficient ζ_i and the flow through this component (for more details see also 4.1.1).

Following the G-POD approach, the operator of the governing equations for the flow through the HVAC unit reads

$$\text{Momentum Eq.} \quad \mathcal{N}_I := \quad 0 = \Delta p_{t,\text{HX}}(\zeta_{\text{HX}}, \dot{V}_{\text{HX}}) - \Delta p_{t,\text{Byp}}(\zeta_{\text{Byp}}, \dot{V}_{\text{Byp}}), \quad (2.27a)$$

$$0 = \Delta p_{t,\text{Defr}}(\zeta_{\text{Defr}}, \dot{V}_{\text{Defr}}) - \Delta p_{t,\text{Face}}(\zeta_{\text{Face}}, \dot{V}_{\text{Face}}), \quad (2.27b)$$

$$\vdots$$

$$\text{Continuum Eq.} \quad \mathcal{N}_{II} := \quad 0 = \left(\sum_{l=1} \dot{V}_l \right)_{\text{Inflow}} - \left(\sum_{l=1} \dot{V}_l \right)_{\text{Outflow}}, \quad (2.27c)$$

$$\text{Energy Eq.} \quad \mathcal{N}_{III} := \quad 0 = \left(\sum_{l=1} \dot{H}_l \right)_{\text{Inflow}} - \left(\sum_{l=1} \dot{H}_l \right)_{\text{Outflow}}. \quad (2.27d)$$

In Eq.2.27 it can be seen that the data set used for the POD must contain the volume flow rates and enthalpy flow rates. A data set of these values for different parameter combinations m can be obtained by calculating the integral volume flow rates and enthalpy flow rates from numerical simulations or by an experimental approach as described in chapter 3. The input data set is then structured as follows

$$\boldsymbol{\varphi}^m = \begin{pmatrix} \dot{V}_{\text{Defr}} \\ \vdots \\ \dot{H}_{\text{Defr}} \\ \vdots \end{pmatrix}^m \quad (2.28)$$

and the POD delivers the series expansion of vector-valued POD modes

$$\begin{pmatrix} \dot{\tilde{V}}_{Defr} \\ \vdots \\ \dot{\tilde{H}}_{Defr} \\ \vdots \end{pmatrix} = \sum_{i=0}^{N_r} a_i \begin{pmatrix} \theta_i^{\dot{V}_{Defr}} \\ \vdots \\ \theta_i^{\dot{H}_{Defr}} \\ \vdots \end{pmatrix}. \quad (2.29)$$

In the next step of the Galerkin procedure, the integral flow variables of Eq. 2.27 are substituted by the series expansion of Eq. 2.29 and projected onto the the POD modes. As a result, a system of equations is generated similar to the RANS application. This system of equations can be solved to estimate the weighting coefficients \tilde{a}_i . Afterwards, the coefficients a_i of the series expansion in Eq. 2.29 are substituted by the estimated coefficients \tilde{a}_i and the volume flow rates and enthalpy flow rates can be directly reconstructed. The series expansion with substituted coefficients is given in matrix form by

$$\begin{pmatrix} \dot{\tilde{V}}_{Defr} \\ \vdots \\ \dot{\tilde{H}}_{Defr} \\ \vdots \end{pmatrix} = \begin{pmatrix} \theta_1^{\dot{V}_{Defr}} & \theta_2^{\dot{V}_{Defr}} & \dots & \theta_{N_r}^{\dot{V}_{Defr}} \\ \vdots & \ddots & & \\ \theta_i^{\dot{H}_{Defr}} & \theta_2^{\dot{H}_{Defr}} & \dots & \theta_{N_r}^{\dot{H}_{Defr}} \\ \vdots & \ddots & & \end{pmatrix} \begin{pmatrix} \tilde{a}_1 \\ \tilde{a}_2 \\ \vdots \\ \tilde{a}_{N_r} \end{pmatrix}. \quad (2.30)$$

However, two major conclusions can be made by inspecting the G-POD procedure applied to integral balances. First, Eq. 2.27a and Eq. 2.27b are the same equations needed to generate a flow resistance network of the HVAC unit. The flow resistance (FR) network is a well established method and frequently used in literature to model the flow distribution as stated in the introduction. In comparison to the Galerkin projection, the network model is more efficient because only few iterations are needed to compute the volume flow rates (see subsection 4.2.1). Second, in Eq. 2.30 it can be seen that the POD modes include two subsets. One subset are the volume flow rates and the other subset are the enthalpy flow rates at the outlets. Although the two subsets refer to different quantities, the coefficients used are identical due to the vector-valued

modes. Considering that the volume flow rates are the results of the flow resistance network, these flow rates can be exploited to estimate the weighting coefficients instead of performing the Galerkin projection. Based on these two conclusions, the O-POD approach is introduced in the following section.

2.3 POD Based on Control-Relevant Output Parameters (O-POD)

The methodology to combine the results of the traditional flow resistance (FR) network with the POD is the focus of this section. The general idea of the O-POD is to structure volume flow rates and enthalpy flow rates in vector-valued POD modes. The task is then to minimize the deviation between the result of the FR network and the series expansion of the volume flow rates by changing the weighting coefficients. Afterwards, the estimated weighting coefficients are further applied to compute the values of the enthalpy flow rates. The major difference between the Galerkin projection and the O-POD is that the Galerkin projection exploits the governing equations, while O-POD incorporates the result of the governing equations for the estimation of the coefficients. Although the O-POD is introduced in the present work to model mixing in HVAC units, it is not limited to this application. Therefore, the generalized procedure is presented in the first subsection. Next, the application to the HVAC unit is described.

2.3.1 Introduction to O-POD Procedure

The generalized concept of the O-POD method is explained below since it can be applied to different technical fields. First, basic definitions are given and then the procedure is explained.

More generally, the volume flow rates at the outlets are observed output variables of the HVAC system. The definition of an observed output variable y^{Obs} is that the actual value is available due to measurements or other models while operating the system. In contrast, the enthalpy flow rates are not observed

output variables. The not observed output $y^{\text{Non-Obs}}$ is not known during operation of the system, but it is required for system control. Therefore, whether a variable is observed or not depends only on their availability during operation. The objective of the output based POD is to generate a ROM to predict the not observed output values by using the observed states. It is known as output based POD (O-POD) method. The basic idea goes back to Everson and Sirovich [27]. They used POD to reconstruct incomplete images of faces. The theory developed by Sirovich was extended by Astrid [9, 10] to accelerate the estimation of the coefficients for high dimensional flow fields. A major difference to applications presented in literature is that observed volume flow rates and not observed values enthalpy flow rates are structured in vector-valued modes (see Eq. 2.30 as example). This allows to separate two subsets of the modes and to estimate the coefficients by using only one of these subsets.

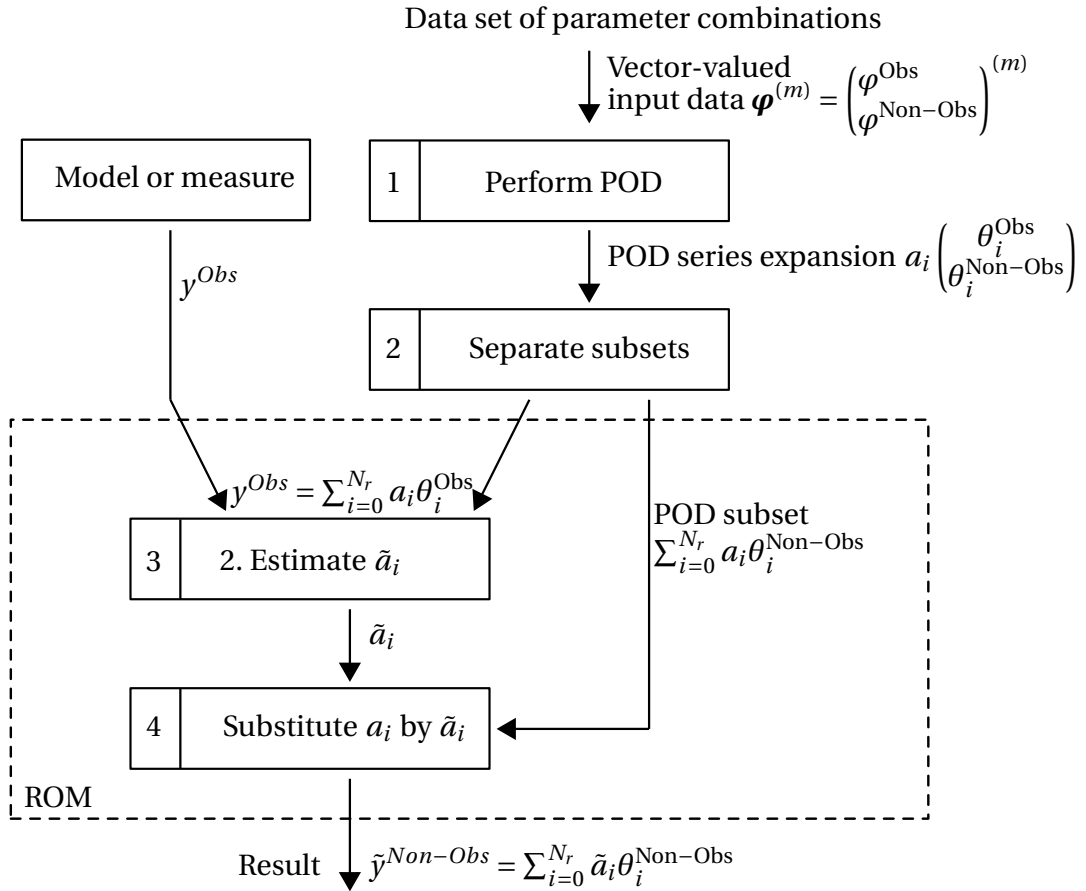


Figure 2.3: Schematic flow chart of the O-POD procedure

The O-POD procedure consists of four steps, which are explained below. A flowchart of this method is shown in Fig.2.3. The numbers in this figure highlight the step of the procedure.

Step 1: Generate vector-valued data set and perform POD

The input data set for the POD consists only of the relevant output data, e.g. integral outlet values of the HVAC unit. An ensemble of observed and not observed variables is obtained for different instances m

$$\boldsymbol{\varphi}^{(m)} = \begin{bmatrix} y^{\text{Obs}} \\ y^{\text{Non-Obs}} \end{bmatrix}^{(m)}. \quad (2.31)$$

Experiments are used in the present thesis to acquire the input data. The POD delivers vector-valued basis functions $\boldsymbol{\theta}_i$, which contain a subset related to the observed quantity θ_i^{Obs} and a subset for the not observed quantity $\theta_i^{\text{Non-Obs}}$

$$\boldsymbol{\theta}_i = \begin{bmatrix} \theta_i^{\text{Obs}} \\ \theta_i^{\text{Non-Obs}} \end{bmatrix}. \quad (2.32)$$

Accordingly, the resulting series expansion of the POD modes follows as

$$\begin{bmatrix} \tilde{y}^{\text{Obs}} \\ \tilde{y}^{\text{Non-Obs}} \end{bmatrix} = \sum_{i=0}^{N_r} a_i \begin{bmatrix} \theta_i^{\text{Obs}} \\ \theta_i^{\text{Non-Obs}} \end{bmatrix}, \quad (2.33)$$

where $N_r < N_s$. A change of \tilde{y}^{Obs} results in different weighting coefficients a_i as shown in Eq. 2.33. This also leads to a different weighting of the POD modes for the not observed output values $\tilde{y}^{\text{Non-Obs}}$. For this reason, the modes of the observed variables are linked to the modes of the not observed output variables by the weighting coefficients. Since y^{Obs} is available during operation, the task is now to estimate the weighting coefficients from this current observed value. The estimated coefficients \tilde{a}_i can then be used to reconstruct the estimated system output $\tilde{y}^{\text{Non-Obs}}$ for unknown instances.

Step 2: Separate POD modes into subsets

For this purpose, the vector-valued modes generated by the POD procedure are separated into two subsets. One subset corresponds to the known value \tilde{y}^{Obs} and the other to the needed output value $\tilde{y}^{\text{Non-Obs}}$

$$\tilde{y}^{\text{Obs}} = \sum_{i=0}^{N_r} a_i \theta_i^{\text{Obs}}, \quad (2.34a)$$

$$\tilde{y}^{\text{Non-Obs}} = \sum_{i=0}^{N_r} a_i \theta_i^{\text{Non-Obs}}. \quad (2.34b)$$

Step 3: Project onto POD modes and estimate \tilde{a}_i

The observed actual value y^{Obs} is utilized to estimate the weighting coefficients from Eq. 2.34a. This results in the minimization of the error between the actual value y^{Obs} and the series expansion in Eq. 2.34a

$$\min_{a_i \in \mathbb{R}} \|y^{\text{Obs}} - \tilde{y}^{\text{Obs}}\|^2 = \min_{a_i \in \mathbb{R}} \left\| y^{\text{Obs}} - \sum_{i=0}^{N_r} a_i \theta_i^{\text{Obs}} \right\|^2. \quad (2.35)$$

Mathematically, this can be expressed by the projection of Eq. 2.35 onto the POD modes, which yields to

$$\begin{aligned} 0 &= \sum_{i=0}^{N_r} \sum_{j=0}^{N_r} \left[(y^{\text{Obs}}, \theta_i^{\text{Obs}}) - a_j (\theta_j^{\text{Obs}}, \theta_i^{\text{Obs}}) \right] \\ \begin{bmatrix} 0 \\ 0 \\ \vdots \\ 0 \end{bmatrix}^T &= \begin{bmatrix} (y^{\text{Obs}}, \theta_0^{\text{Obs}}) \\ (y^{\text{Obs}}, \theta_1^{\text{Obs}}) \\ \vdots \\ (y^{\text{Obs}}, \theta_{N_r}^{\text{Obs}}) \end{bmatrix}^T - [1 \quad a_1 \quad \dots \quad a_{N_r}] \begin{bmatrix} (\theta_0^{\text{Obs}}, \theta_0^{\text{Obs}}) & \dots & (\theta_0^{\text{Obs}}, \theta_{N_r}^{\text{Obs}}) \\ (\theta_1^{\text{Obs}}, \theta_0^{\text{Obs}}) & \dots & (\theta_1^{\text{Obs}}, \theta_{N_r}^{\text{Obs}}) \\ \vdots & \ddots & \vdots \\ (\theta_{N_r}^{\text{Obs}}, \theta_0^{\text{Obs}}) & \dots & (\theta_{N_r}^{\text{Obs}}, \theta_{N_r}^{\text{Obs}}) \end{bmatrix}, \end{aligned} \quad (2.36)$$

where $i, j \in [1, N_r]$. The system of equations in Eq. 2.36 is solved by an iterative procedure to estimate the weighting coefficients \tilde{a}_i . Newtons method has been applied. At this point, a limitation of the O-POD approach has to be reported. The number of modes used by the O-POD procedure is limited by the Degrees of Freedom (DOF) of the system of equations in Eq. 2.36.

Thus, the number of POD modes N_r has to fulfill the following criterion: $N_r \leq DOF$. Otherwise the system of equations is overdetermined.

Step 4: Substitute a_i by \tilde{a}_i

The needed output $\tilde{y}^{\text{Non-Obs}}$ is calculated in the last step. The weighting coefficients a_i are substituted by the estimated weighting coefficients \tilde{a}_i in the series expansion of Eq. 2.34b. Then, the approximated output $\tilde{y}^{\text{Non-Obs}}$ is computed

$$\tilde{y}^{\text{Non-Obs}} = \sum_{i=0}^{N_r} \tilde{a}_i \theta_i^{\text{Non-Obs}}. \quad (2.37)$$

2.3.2 Application to Flow and Mixing in HVAC Units

The O-POD procedure is applied to the mixing process in HVAC units. The not observed output quantities are the enthalpy flow rates \dot{H}^+ at the outlets downstream of the mixing process in the HVAC unit. The observed values are the volume flow rates \dot{V}^+ , since they can be easily computed with a Fluid Resistance (FR) network. Volume flow rates and enthalpy flow rates are scaled by the total inflow of the mixing chamber

$$\dot{V}_n^+ = \frac{\dot{V}_n}{\sum_{n=1}^N \dot{V}_n}, \quad (2.38a)$$

$$\dot{H}_n^+ = \frac{\dot{H}_n}{\sum_{n=1}^N \dot{H}_n}, \quad (2.38b)$$

where N is the number of outlets. Thus, the input data for the O-POD proce-

ture is structured as follows

$$\boldsymbol{\varphi}^{(m)} = \begin{bmatrix} \mathbf{y}^{\text{Obs}} \\ \mathbf{y}^{\text{Non-Obs}} \end{bmatrix}^{(m)} = \begin{bmatrix} \dot{\mathbf{V}}^+ \\ \dot{\mathbf{H}}^+ \end{bmatrix}^{(m)} = \begin{bmatrix} \dot{V}_{\text{HX}}^+ \\ \dot{V}_{\text{Defr}}^+ \\ \vdots \\ \dot{V}_{\text{Foot}}^+ \\ \dot{H}_{\text{Defr}}^+ \\ \vdots \\ \dot{H}_{\text{Foot}}^+ \end{bmatrix}^{(m)}. \quad (2.39)$$

The first value of the vector \dot{V}_{HX}^+ corresponds to the dimensionless volume flow rate through the HX. The other values \dot{V}_{Defr}^+ to \dot{V}_{Foot}^+ refer to the air distribution at the outlets. The input data set for the POD can be obtained by calculating the integral values from numerical simulations or experiments. In section 4.1 numerical simulations of a simplified model are used to assess the O-POD procedure without experimental uncertainties. To model the real HVAC unit, measurement data from section 3.1 is provided as input since experiments require less time than CFD simulations of the HVAC unit. From the vector-valued observations in Eq. 2.39, the POD modes $\boldsymbol{\theta}_i = \left[\boldsymbol{\theta}^{\dot{V}^+} \boldsymbol{\theta}^{\dot{H}^+} \right]_i^T$ can be calculated and the series expansion yields (**step 1**)

$$\begin{bmatrix} \dot{\mathbf{V}}^+ \\ \dot{\mathbf{H}}^+ \end{bmatrix} = \sum_{i=0}^{N_r} a_i \begin{bmatrix} \boldsymbol{\theta}^{\dot{V}^+} \\ \boldsymbol{\theta}^{\dot{H}^+} \end{bmatrix}_i = \sum_{i=0}^{N_r} a_i \begin{bmatrix} \theta_{\text{HX}}^{\dot{V}^+} \\ \theta_{\text{Defr}}^{\dot{V}^+} \\ \vdots \\ \theta_{\text{Foot}}^{\dot{V}^+} \\ \theta_{\text{Defr}}^{\dot{H}^+} \\ \vdots \\ \theta_{\text{Foot}}^{\dot{H}^+} \end{bmatrix}_i. \quad (2.40)$$

The modes from Eq. 2.40 are then separated into two subsets according to **step 2** of the O-POD procedure. The first subset corresponds to the volume

flow rates as observed output parameters

$$\tilde{\mathbf{y}}^{\text{Obs}} = \dot{\mathbf{V}}^+ = \sum_{i=0}^{N_r} a_i \boldsymbol{\theta}_i \dot{V}_i^+. \quad (2.41)$$

The actual volume flow rates at the outlets from Eq. 2.41 can be computed by using the fluid resistance model (see section 1.1.2). The second subset of Eq.2.40 describes the not observed output parameters, which are the enthalpy flow rates

$$\tilde{\mathbf{y}}^{\text{Non-Obs}} = \dot{\mathbf{H}}^+ = \sum_{i=0}^{N_r} a_i \boldsymbol{\theta}_i \dot{H}_i^+. \quad (2.42)$$

The subset of the volume flow rates in Eq. 2.41 is used to estimate the weighting coefficients \tilde{a}_i for instances, which are not included in the parameter combinations of the input data (**step 3**). It is considered that the calculated volume flow rates $\dot{\mathbf{V}}_{FR}^+$ from the FR model are the actual observed output values \mathbf{y}^{Obs} . The error between the reconstructed volume flow rates $\dot{\mathbf{V}}^+$ and the actual value from the FR model is minimized

$$\begin{aligned} 0 &= \mathbf{y}^{\text{Obs}} - \tilde{\mathbf{y}}^{\text{Obs}} \\ &= \dot{\mathbf{V}}_{FR}^+ - \dot{\mathbf{V}}^+. \end{aligned} \quad (2.43)$$

In Eq. 2.43 the series expansion of the volume flow rates from Eq. 2.41 can be substituted. Subsequently, Eq. 2.43 is projected onto the POD modes. This results in

$$\begin{aligned} \text{Substitute } 0 &= \dot{\mathbf{V}}_{FR}^+ - \sum_{j=0}^{N_r} a_j \boldsymbol{\theta}_j \dot{V}_j^+ \\ \text{Project } \left(\sum_{i=0}^{N_r} \boldsymbol{\theta}_i \dot{V}_i^+, 0 \right) &= \left(\sum_{i=0}^{N_r} \boldsymbol{\theta}_i \dot{V}_i^+, \dot{\mathbf{V}}_{FR}^+ \right) - \left(\sum_{i=0}^{N_r} \boldsymbol{\theta}_i \dot{V}_i^+, \sum_{j=0}^{N_r} a_j \boldsymbol{\theta}_j \dot{V}_j^+ \right) \\ \underbrace{\sum_{i=0}^{N_r} \left(\boldsymbol{\theta}_i \dot{V}_i^+, 0 \right)}_{=0} &= \underbrace{\sum_{i=0}^{N_r} \left(\boldsymbol{\theta}_i \dot{V}_i^+, \dot{\mathbf{V}}_{FR}^+ \right)}_{\mathcal{F}_i} - \sum_{i=0}^{N_r} \sum_{j=0}^{N_r} a_j \underbrace{\left(\boldsymbol{\theta}_i \dot{V}_i^+, \boldsymbol{\theta}_j \dot{V}_j^+ \right)}_{\mathcal{C}_{ij}}. \end{aligned} \quad (2.44)$$

The reconstruction of the series expansion in Eq. 2.41 and 2.42 must respect mass conservation and energy conservation, respectively

$$\begin{aligned} \text{Mass conservation } 0 &= \dot{V}_{\text{Inflow}}^+ - \sum_{n=1}^N \dot{V}_n^+, \\ \text{Energy conservation } 0 &= \dot{H}_{\text{Inflow}}^+ - \sum_{n=1}^N \dot{H}_n^+. \end{aligned} \quad (2.45)$$

The total flow rates V_{Inflow}^+ and H_{Inflow}^+ result in 1 since all volume flow rates and all mass flow rates are scaled by the corresponding total inflow. The POD modes are substituted in Eq. 2.45 and the resulting system of equations of the O-POD procedure reads

$$\begin{aligned}
 \text{Constraint FR model} \quad 0 &= \sum_{i=0}^{N_r} \mathcal{F}_i - \sum_{i=0}^{N_r} \sum_{j=0}^{N_r} a_j \mathcal{C}_{ij}, \\
 \text{Mass conservation} \quad 0 &= 1 - \sum_{n=1}^N \sum_{j=0}^{N_r} a_j \boldsymbol{\theta}_j^{\dot{V}^+}, \\
 \text{Energy conservation} \quad 0 &= 1 - \sum_{n=1}^N \sum_{j=0}^{N_r} a_j \boldsymbol{\theta}_j^{\dot{H}^+}.
 \end{aligned} \tag{2.46}$$

2.4 Summary of the POD Models

In summary, two procedures have been presented in this chapter to estimate the weighting coefficients of POD modes. These weighting methods are compared in Tab. 2.2 with each other.

The ROM generated by G-POD models the high dimensional flow fields. Numerical data of the complete flow field is required as input for the POD procedure. This data set is obtained by CFD simulations for selected valve positions. The governing equations are incorporated to estimate the coefficients for the POD modes. Afterwards, the high dimensional flow field of the HVAC unit can be reconstructed using the POD series expansion and the integral enthalpy flow rates are computed from these flow fields. This procedure is in particular suitable if detailed information about the distribution of the flow variables is needed, e.g. a temperature profile on a surface. Regarding climate control, the flow fields cover more information than needed because only the integral outlet values are important.

In contrast to the G-POD method, the ROM generated by the O-POD procedure models only the control-relevant parameters. The POD input are observed and not observed output values. Applied to the HVAC unit, the observed parameters are the volume flow rates and the not observed parameters are the enthalpy flow rates. Therefore, the resulting POD modes have a lower dimension in comparison to the modes from the G-POD method and include only necessary information. The input data to perform the POD is obtained

Table 2.2: Summary of the POD procedures applied to the mixing process

	Traditional POD-Galerkin	Output based POD
Input data	Spatial flow field $\boldsymbol{\varphi}(\mathbf{x}) = \begin{pmatrix} \mathbf{u}^+(\mathbf{x}) \\ p^+(\mathbf{x}) \\ v_t^+(\mathbf{x}) \\ T^+(\mathbf{x}) \end{pmatrix}$	Integral values $\boldsymbol{\varphi} = \begin{pmatrix} \dot{\mathbf{V}}^+ \\ \dot{\mathbf{H}}^+ \end{pmatrix}$
Applicability	Numerical simulations	Measurements or simulations
Number of POD modes N_r	$\leq N_s$ (see Eq. 2.9)	$\leq DOF$ (see systems of equations in Eq. 2.36)
Additional modeling	Not required	Fluid resistance network
Constraints	RANS Equations Scalar Transport Equation	Observed volume flow rates

for relevant operating conditions of the HVAC unit by calculating the integral values from numerical simulations or by measurements. In section 4.1 the application to a numerical benchmark model is shown, while the O-POD model for the real HVAC unit in section 4.2 is generated from an experimental data set. The weighting coefficients are estimated by using only the volume flow rates. These flow rates are computed by a FR network. The estimated weighting coefficients are then utilized to reconstruct the estimated enthalpy flow rates at the outlets.

3 Experiments

The experimental approach is described in this chapter. The measurements were needed to obtain the experimental data set of the enthalpy flow rates and volume flow rates for the generation of the O-POD model. This data base was acquired from a laboratory test rig of the HVAC unit. The test rig and the structure of the experimental input data for the POD are described in section 3.1. Furthermore, a test vehicle was equipped with additional measurement technique. The vehicle and applied sensor hardware are presented in section 3.2. Validation data from the test rig and a real driving scenario were finally used in chapter 4 and chapter 5 to evaluate the generated O-POD model.

3.1 Test Rig

3.1.1 Structure and Function of the Test Rig

The test rig provided integral volume flow rates and enthalpy flow rates at the outlets as a function of operational parameters. The piping and instrumentation diagram of the test rig is shown in Fig. 3.1. The detailed specification of its components is given in subsection 3.1.2. The set up is explained below following the flow through the set up.

The bellmouth intake nozzle was used to determine the total mass flow rate induced by the blower (see ① in Fig.3.1). The Revolutions Per Minute (RPM) of the blower (②.1) were regulated to control the total mass flow rate. The HVAC unit provided conditioned air for three climate zones (front left, front right and rear) of the vehicle cabin and was separated into two parts (left and right climate zone).

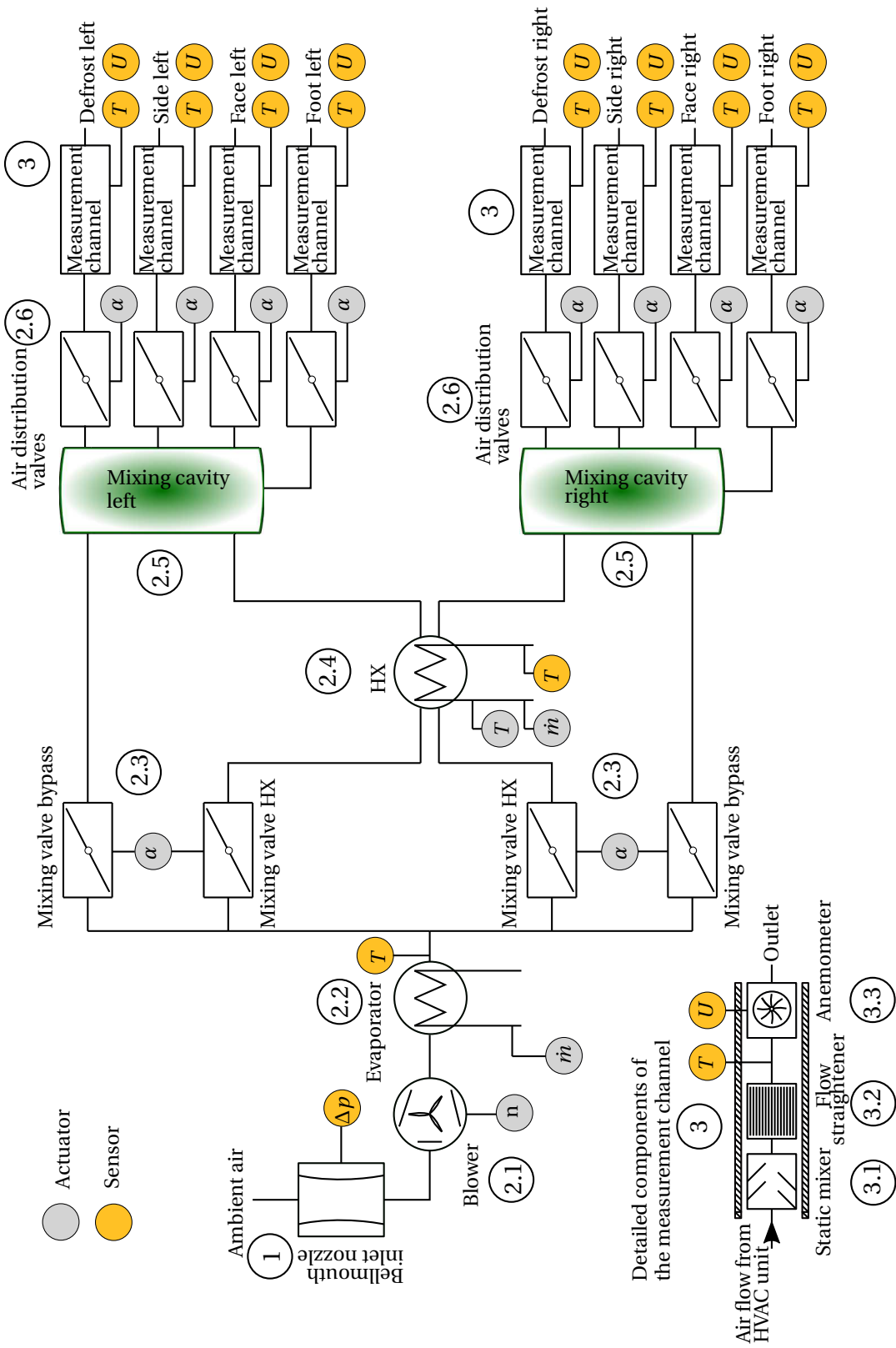


Figure 3.1: Piping and instrumentation diagram of the test rig

These parts were almost symmetrical and contained the same components. The rear flow path was connected to a secondary HVAC unit in the vehicle. However, the flow path to the rear has been shut off at the test rig and is not discussed further to reduce the experimental effort. From the blower, the air passed the evaporator (2.2). There it was cooled down and dehumidified. The air temperature at the outlet of the evaporator was measured and used for the control of the refrigerant cycle. Mixing valves (2.3) after the evaporator determined the amount of air flow through the heat exchanger (HX) (2.4) and the bypass. The evaporator has been connected to an external refrigerant cycle and the HX to an external heating loop. The external components are shown in Fig. 3.2. The cold air stream from the bypass and the hot air stream from the HX were then mixed in the mixing cavity (2.5).

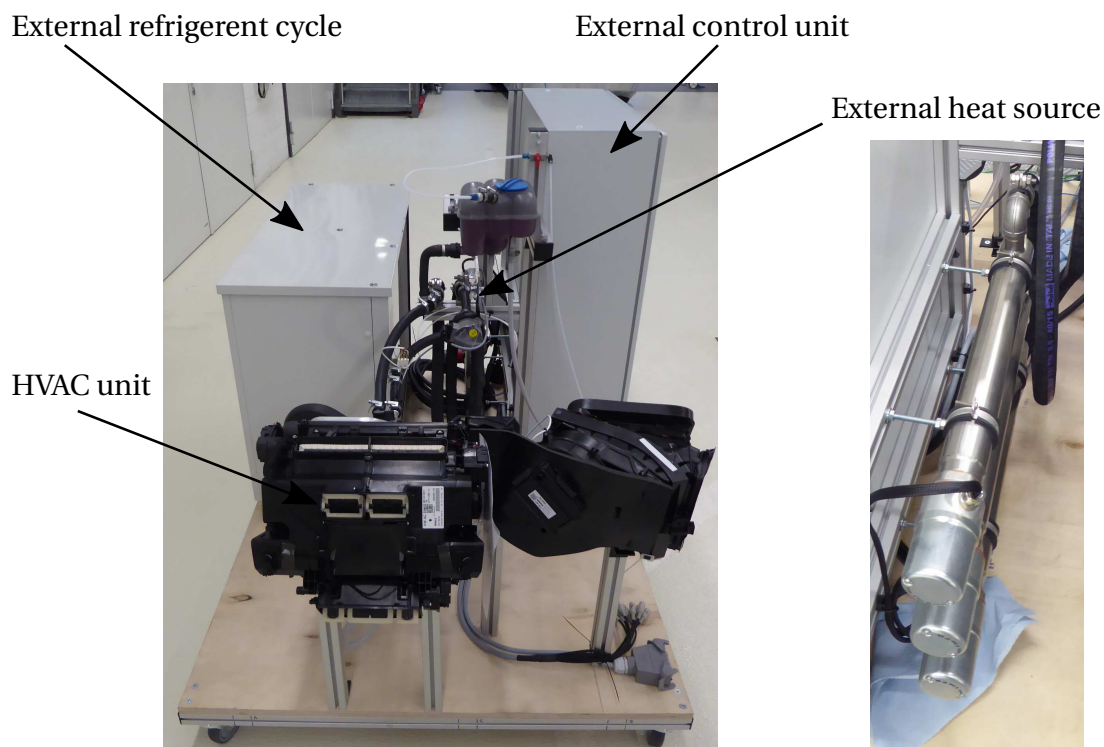


Figure 3.2: Test rig

3.1 Test Rig

From the mixing cavity, the air left the HVAC unit through the outlets and through the measurement channels. Each climate zone of the HVAC unit had four outlets: side, foot, face and defrost. The mass flow rates through the outlets were independently regulated by air distribution valves (2.6). In the measurement channels (3), static mixers (3.1) homogenized the temperature profile of the flow. A flow straightener (3.2) created a uniform velocity profile for the volume flow rate measurements downstream of the mixer. The outlet temperatures were measured by 4 thermocouples. Anemometers (3.3) were used for the determination of the mean velocity at each outlet. The velocities measured were further utilized to calculate the dimensionless mass flow rate at the corresponding outlet.

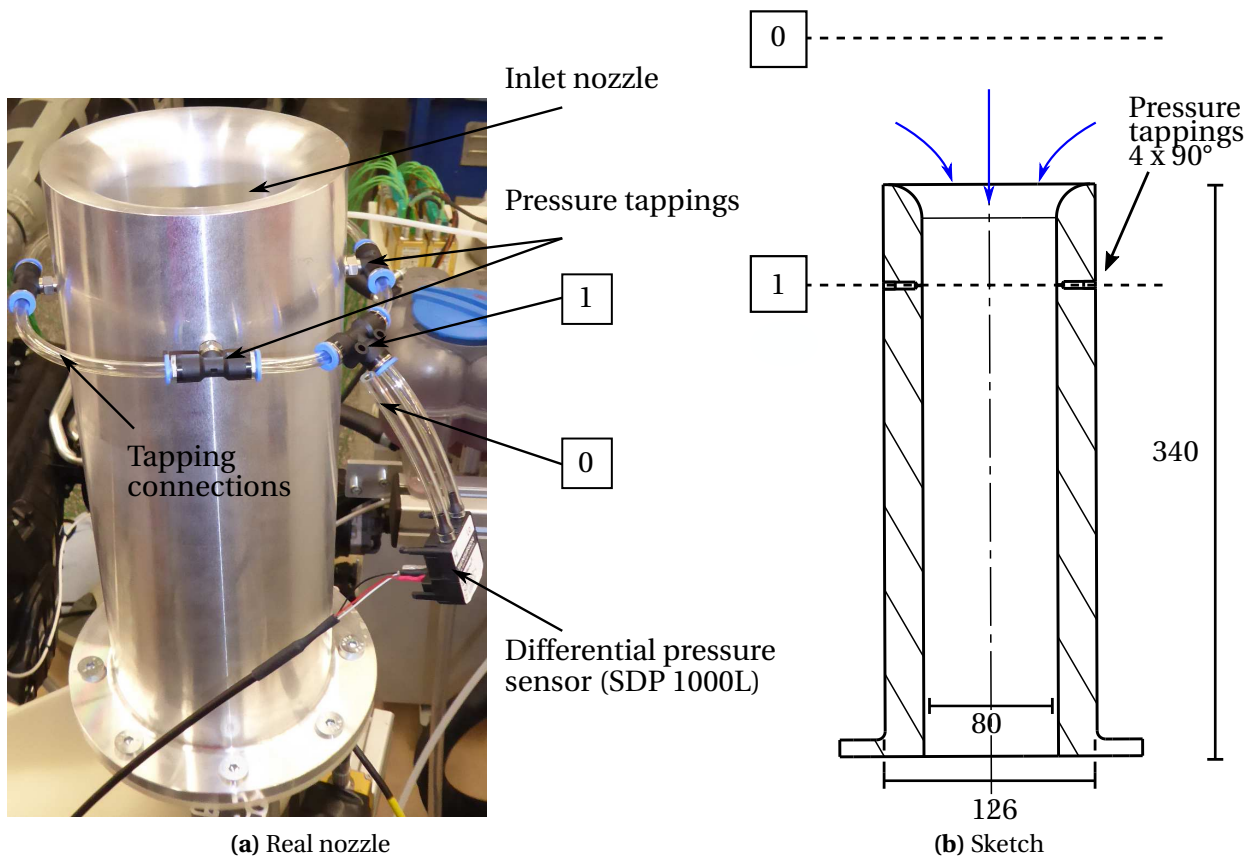


Figure 3.3: Bellmouth inlet nozzle for the measurement of total mass flow rate

3.1.2 Design of Components

The bellmouth inlet nozzle and the measurement channels were used to determine the mass flow rate and enthalpy flow rate distribution in the test rig.

Bellmouth inlet nozzle

The nozzle geometry was based on DIN EN ISO 5801[22] and is shown in Fig. 3.3. The differential pressure Δp between the the environment (section 0) and the cross section 1 was measured. Due to the bellmouth, the total air mass flow rate can be calculated from the measured differential pressure

$$\dot{m}_{tot} = \frac{\pi D^2}{4} \sqrt{2\rho_E \Delta p}. \quad (3.1)$$

$D = 0.08$ m was the diameter of the inlet throat and ρ_E was the ambient air density. The error of the measured mass flow rates has been evaluated according to [80, 81, 91].

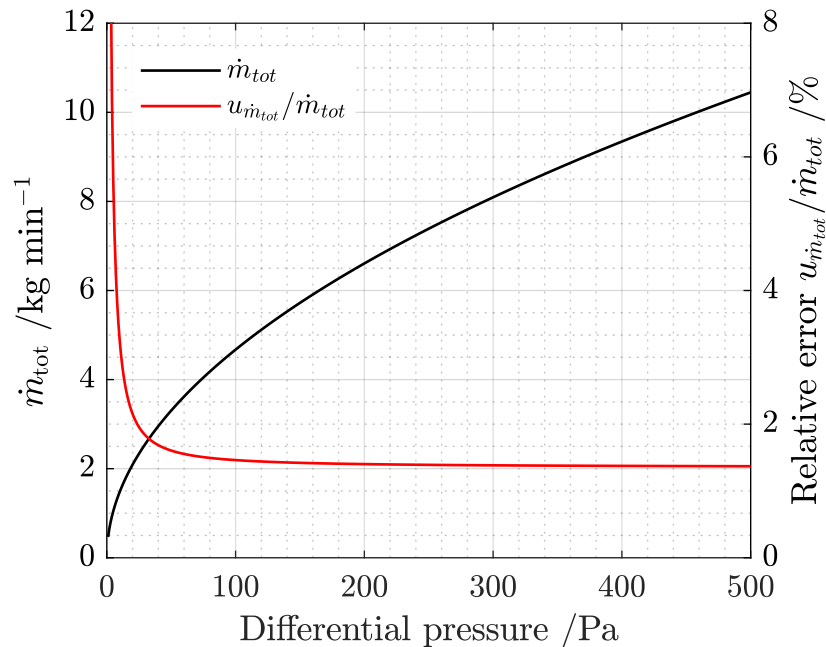


Figure 3.4: Range and uncertainty $u_{\dot{m}_{tot}}$ of the total mass flow rate measured with the bellmouth inlet nozzle

For the expected operation range of the total air mass flow rate ($3\text{-}10\text{ kg min}^{-1}$), an error of $< 2\%$ of the mass flow rate was determined for the measurement configuration as shown in Fig. 3.4.

Measurement channels

The measurement channel is illustrated in detail in Fig. 3.5. It contained the static mixer, the flow straightener, the thermocouples and the anemometer. Temperatures above 60°C were expected during operation of the test rig. Polypropylene channels have been selected as they provide good thermal properties and have a recommended operating temperature $\leq 85^\circ\text{C}$. The diameter $D_O = 90\text{ mm}$ has been chosen according to the diameter of the anemometers. The geometrical data of the measurement channels is summarized in Tab. 3.1.

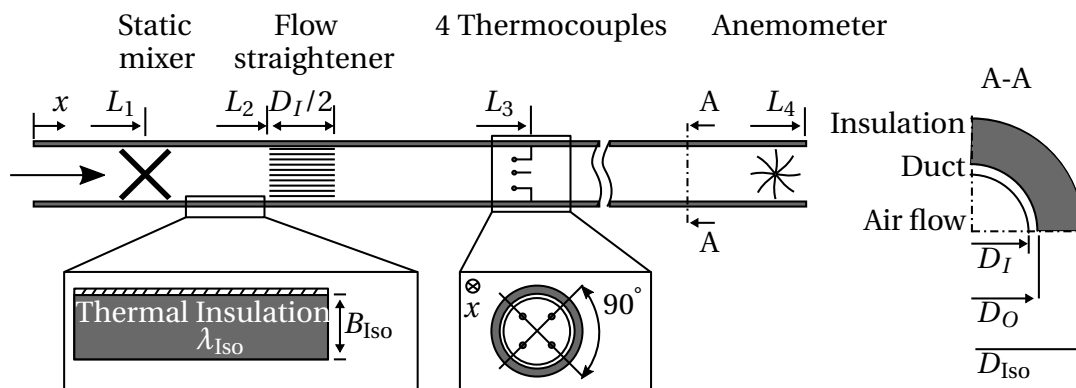
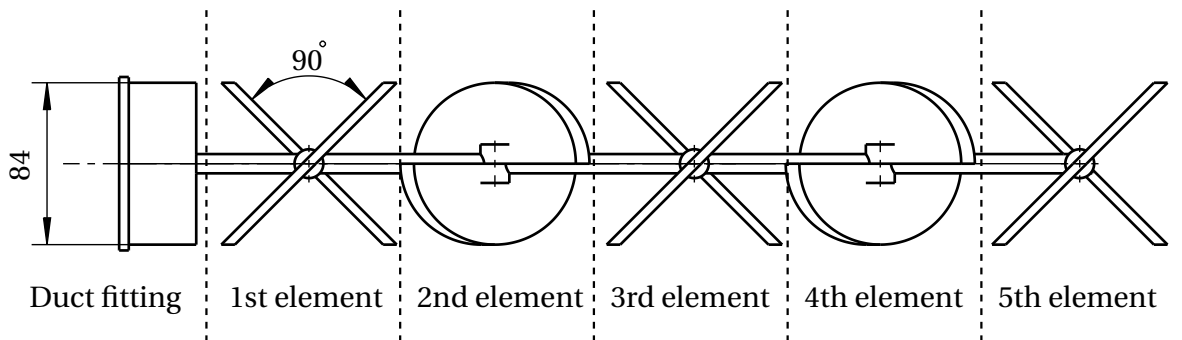


Figure 3.5: Channel for the measurement of temperature and volume flow rates at the outlets of the HVAC unit

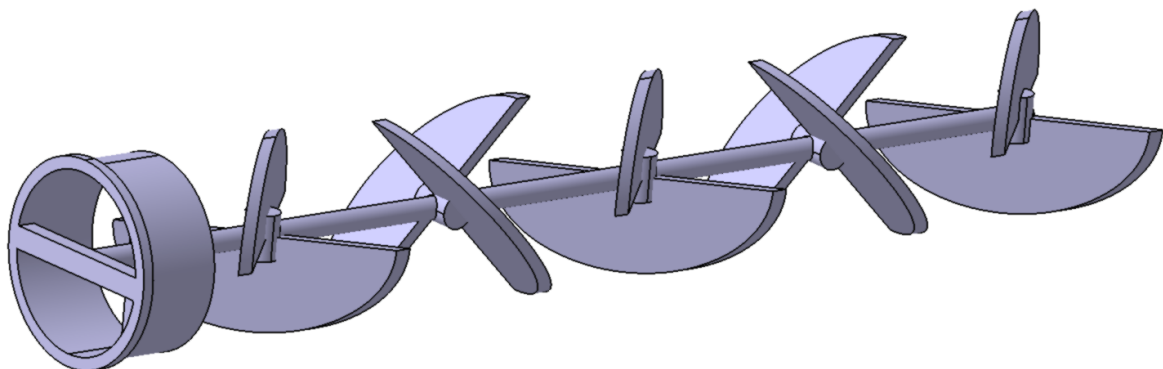
Table 3.1: Geometrical data of the measurement channels

Specification	Value
Outer diameter duct D_O	0.090 m
Inner diameter duct D_I	0.0856 m
Outer diameter insulation D_{Iso}	0.135 m
Static mixer - Length L_1	0.25 m
Flow straightener - Length L_2	0.4 m
Thermocouples - L_3	0.65 m
Anemometer - L_4	2 m

Thermal insulation was used to minimize heat loss along the channel. The thickness of the insulation B_{ISO} was 22.5 mm with a thermal conductivity of $0.035 \text{ W m}^{-1} \text{ K}^{-1}$. The heat loss to the ambient air of the flow with an inlet temperature of $45 \text{ }^\circ\text{C}$ and a mass flow rate of 3.3 kg min^{-1} was 0.2 % of the respective enthalpy flow rate [24]. Thermocouples have been utilized for the temperature measurements. Four thermocouples were arranged at a 90° angle over the circumference of the duct (see Fig. 3.5) to verify that no temperature inhomogeneities remained in the air flow. A static mixer has been designed, which allowed the sequential placement of mixing elements (see Fig. 3.6). The objective of the mixer was to eliminate temperature differences in the air flow resulting from the mixing process in the HVAC unit. This was necessary to measure a bulk mean temperature and to compute the enthalpy flow rates for the O-POD procedure.



(a) Sketch



(b) 3D computer-aided design model

Figure 3.6: Geometry of the static blade mixer

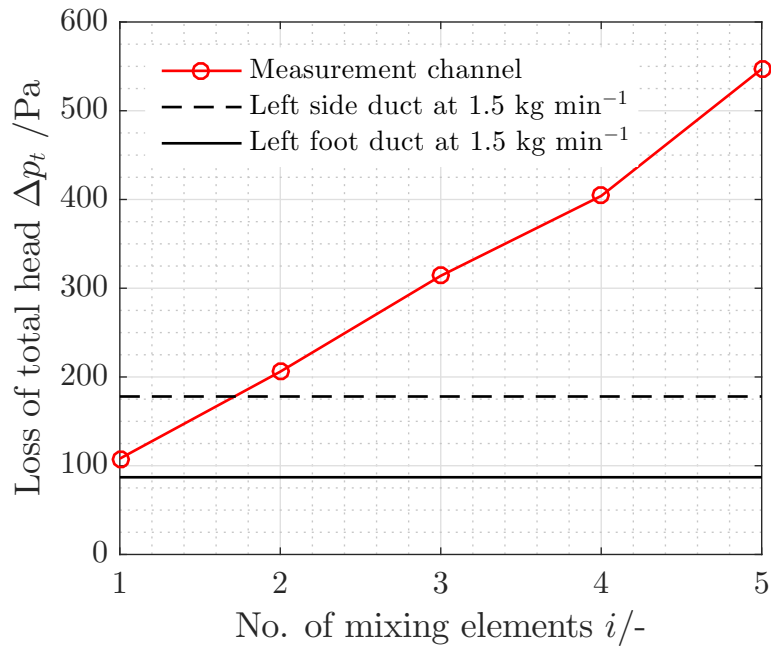


Figure 3.7: Loss of total head of the mixer for varying number of elements

CFD simulations and measurements were conducted to optimize the balance between the induced pressure drop and mixing quality. The loss of total head is shown in Fig. 3.7 for the mixer configurations. Furthermore, the head loss for two representative ventilation ducts is shown. They were used as permissible loss for the measurement duct to have a similarity of the operating behavior between test rig and car application. This was important since the O-POD model generated by measurements from the test rig was also applied to a real driving scenario using the test vehicle in subsection 4.2.1. It can be seen that the maximum permissible number of mixing elements is two since three or more elements significantly exceed the loss of the ventilation ducts in the vehicle. The maximum temperature deviation between the thermocouples for one and two mixing elements is very small ($< 0.2 \text{ K}$) and is within the measurement uncertainty of the calibrated thermocouples ($\approx 0.15 \text{ K}$, see Fig. B.2 in the appendix). Thus, mixers with one element were applied for further experimental investigations as a compromise between low pressure loss and sufficient mixing performance.

3.1.3 Measurement Procedure

The integral volume flow rates and enthalpy flow rates were calculated from the measured velocities and temperatures at the outlets. An anemometer measured the mean velocity $U_{n,k}$ at each outlet. The subscript k refers to the climate zone of the HVAC unit and n denotes the corresponding outlet. As an example, k could be the left climate zone and n the defrost outlet. These velocities were further applied to compute the dimensionless mass flow rate at a specific outlet

$$\dot{m}_{n,k}^+ = \frac{\rho_{n,k} A_{n,k} U_{n,k}}{\sum_{k=1}^2 \sum_{n=1}^4 \rho_{n,k} A_{n,k} U_{n,k}}. \quad (3.2)$$

The anemometers had identical cross sections. The corresponding mass flow rate of the outlet was then be calculated with the dimensionless mass flow rate from Eq. 3.2 and the total mass flow rate \dot{m}_{tot}

$$\dot{m}_{n,k} = \frac{\rho_{n,k} U_{n,k}}{\sum_{k=1}^2 \sum_{n=1}^4 \rho_{n,k} U_{n,k}} \dot{m}_{tot} = \dot{m}_{n,k}^+ \dot{m}_{tot}. \quad (3.3)$$

The dimensionless enthalpy flow rates are computed by

$$\dot{H}_{n,k}^+ = \frac{\dot{m}_{n,k}^+ \dot{m}_{tot} c_p T_{n,k}}{\sum_k \sum_n \dot{m}_{n,k}^+ \dot{m}_{tot} c_p T_{n,k}} = \frac{\dot{m}_{n,k}^+ c_p T_{n,k}}{\sum_k \sum_n \dot{m}_{n,k}^+ c_p T_{n,k}}. \quad (3.4)$$

A constant value was assumed for the heat capacity c_p and Eq. 3.4 simplifies to

$$\dot{H}_{n,k}^+ = \frac{\dot{m}_{n,k}^+ T_{n,k}}{\sum_k \sum_n \dot{m}_{n,k}^+ T_{n,k}}. \quad (3.5)$$

The error of both dimensionless volume flow rate and dimensionless enthalpy flow rate at an outlet was approximately 0.015 for a representative operating condition of the HVAC unit (see appendix B.1).

The step response of the temperature was investigated to obtain a time scale for the measurement campaign. The step response of the dimensionless temperature to a large step at the left side outlet is shown in Fig. 3.8. The dimen-

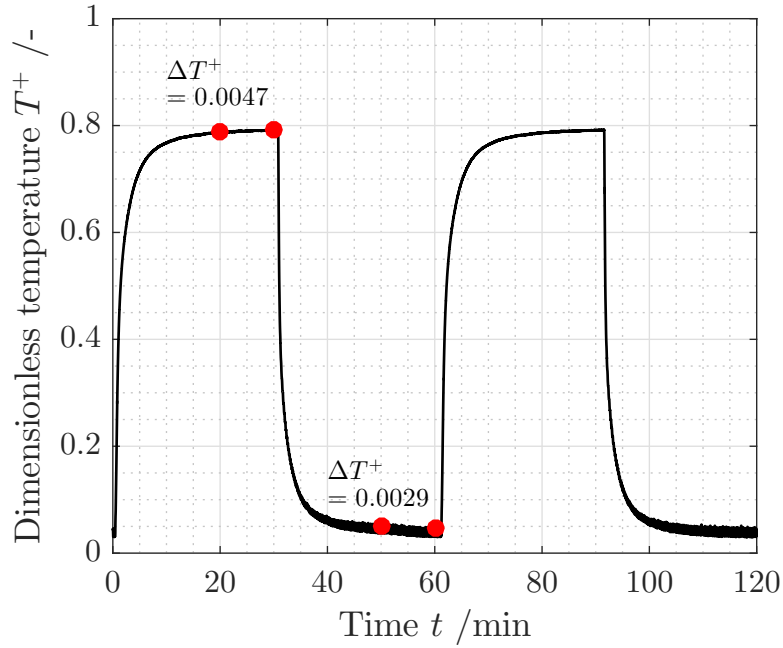


Figure 3.8: Step response of the dimensionless temperature at the left side outlet

Dimensionless outlet temperature is the ratio of the actual temperature increase to the maximum permissible temperature increase

$$T^+ = \frac{T - T_{\text{Evap}}}{T_{\text{HX}} - T_{\text{Evap}}}. \quad (3.6)$$

Steady state is reached after 20 minutes where the dimensionless outlet temperature difference ΔT^+ falls below 0.005. Therefore, each operating condition was run for 20 minutes before the temperature was measured for 1 minute. The average was calculated from the measured data. The test rig was pre-heated for 60 minutes to reduce the effect of initial transients before a series of operating conditions was measured to account for the dynamic behavior of external components.

3.1.4 Structure of the Experimental Data Set

The selection of operating conditions is explained below. The selected operating conditions were measured by the test rig and the resulting experimental

data set was provided as input for the O-POD procedure in section 4.2. The aim was to balance measurement time with coverage of the parameter space. First, combinations for the positions of the air distribution valves were specified. Then, these valve combinations were measured at different mixing valve angles. Three positions have been selected for each air distribution valve as shown in Tab.3.2. In this table, 100% corresponds to an opened valve and 0 % to a closed valve. The operating conditions of the valves for both climate zones were identical, which led to a total of $3^4 = 81$ valve combinations. From these combinations only those valve combinations were measured, which corresponded to a realistic operating scenario of the real vehicle. The following criterion was used to down-select the initial set of operating conditions

$$150\% \leq \sum_n^N \alpha_n^+ \leq 300\%, \quad (3.7)$$

where N denotes the number of outlets. This avoided that all valves were completely opened or almost closed. As a result, 41 combinations remained. This set of operating conditions for the air distribution valves was applied for different positions of the mixing valves. From prestudies it was known that mixing valve positions from 30 % to 60 % with steps of 10 % covered the interesting range of the mixing process. So, $4 \cdot 41 = 164$ operating conditions were measured. Approximately 60 h were required to obtain these 164 valve combinations.

In comparison to CFD simulations, the measurements require significantly less time. The average time to perform a CFD simulation of the real HVAC unit is 5 hours using 120 CPU cores at 2.4 GHz on a cluster architecture[55]. 820 hours would have been required if the input data for the POD had been obtained by CFD simulations.

The experimental data set for the O-POD procedure should cover large variations of the valve positions. This was necessary to maintain accuracy over a wide operating range and to cover asymptotic behavior as shown in section 4.2.2. Therefore, the 164 valve combinations were extended based on physical assumptions: The total volume flow rate was heated in the HX at a mixing

valve position of 100 %. So at $\dot{V}_{HX}^+ = 1$, all outlet temperatures corresponded approximately to the air temperature at the outlet of the HX. The dimensionless enthalpy flow rates resulted in $\dot{H}^+ (\dot{V}_{HX}^+ = 1) = \dot{V}^+ (\dot{V}_{HX}^+ = 1)$. The dimensionless volume flow rates at the outlets were particularly influenced by the air distribution valves. Therefore, the volume flow rates measured were provided as observations for the enthalpy flow rates at a mixing valve position of 100 % to extend the operating range of O-POD model. The data set generated by using this physical assumption is named as extended data set in the following.

3.2 Vehicle Measurement

A vehicle was equipped with additional measurement instrumentation to gain measurement data similar to the experimental data from the test rig. This allowed the validation of the model under real driving conditions. The test vehicle and HVAC system of the car are described in the first subsection. Subsequently, in the second subsection the additional sensor hardware for the model validation is outlined.

Table 3.2: Parameters for experimental data set

Parameter	Value
Valves	
Left/Right defrost	0% - 20% - 40%
Left/Right face	0% - 50% - 100%
Left/Right side	0% - 50% - 100%
Left/Right foot	0% - 50% - 100%
Left/Right mixing valves	30% - 40% - 50% - 60%
Blower and external cycles	
Total mass flow rate \dot{m}_{tot}	4 kg min ⁻¹
Air outlet temperature evaporator T_{Evap}	10 °C
Coolant inlet temperature HX T_{HX}	70 °C
Volume flow rate coolant HX \dot{V}_{HX}	25 L min ⁻¹

3.2.1 Test Vehicle

The test vehicle was an Audi Q7 model. The front HVAC unit of this vehicle and the test rig were identical. In the test vehicle a secondary rear HVAC unit was connected to the rear outlets. This rear HVAC unit operated in the recirculation mode and drew air from the cabin. It was regulated independently from the front HVAC unit and will not be considered here. Ventilation ducts distributed the air flow to the car cabin. The design of ventilation ducts resulted in a complex geometry with small cross sections and high length to height ratios to fit in the car package. The outlet temperatures were measured by standard sensors. These standard sensors were only applied at the side and foot outlets. This led to a total of 4 standard sensors (left side, left foot, right side and right foot) for the HVAC system. The actual driving situation and ambient conditions were determined by a large number of standard sensors in the car. These sensors provided the input for the ACC to calculate the setpoints for the outlet temperatures (see also section 5.2.2).

3.2.2 Measurement Setup

Additional measurement hardware was integrated in the vehicle to allow a comprehensive validation of the HVAC model. In Tab. 3.3 the standard and additional measurement instrumentation is summarized. At the inlets of the ventilation ducts thermocouples measured the temperature. The thermocouples are shown for the left side ventilation duct in Fig. 3.9. Five thermocouples were distributed evenly over the inlet cross section. This was necessary because no mixer was applied to produce a homogeneous temperature profile. These 5 thermocouples detected temperature inhomogeneities in the airflow. It had been assumed that the mean average of these 5 thermocouples corresponded approximately to the caloric mean temperature. A grid of thermocouples measured the air temperatures at the outlet of the HX and evaporator. In total 98 thermocouples were used for measurements in the air path of the HVAC unit. In the heating loop thermocouples measured the coolant temperature at the inlet and outlet of the HX. Furthermore, the volume flow rate was determined by a flow sensor to calculate the heat transfer in the HX.

Table 3.3: Important sensor hardware in the test vehicle

Location	Measured quantity	Unit	Standard sensors	Additional sensors
Air path HVAC unit				
Left/Right defrost	Air temperature	°C	-	✓
Left/Right side	Air temperature	°C	✓	✓
Left/Right face	Air temperature	°C	-	✓
Left/Right foot	Air temperature	°C	✓	✓
Cabin	Air temperature	°C	✓	-
HX outlet	Air temperature	°C	-	✓
Evaporator outlet	Air temperature	°C	✓	✓
Heating loop				
Inlet HX	Coolant temperature	°C	-	✓
Outlet HX	Coolant temperature	°C	-	✓
Inlet HX	Coolant volume flow rate	Lmin ⁻¹	-	✓
Ambient conditions				
Ambient air	Air temperature	°C	✓	-
Ambient pressure	Air pressure	bar	✓	-
Solar radiation	Radiant flux	Wm ⁻²	✓	-



(a) Left side ventilation duct



(b) Thermocouples at the inlet of the ventilation duct

Figure 3.9: Left side ventilation duct equipped with thermocouples for driving measurements

4 Prediction of Flow and Mixing in HVAC Units

The O-POD approach is evaluated in this chapter. In the first section, integral outlet values were computed from numerical simulations of a simplified mixing cavity as input for the O-POD. Furthermore, the same simulations were used to perform the Galerkin projection. The aim of the numerical model was to produce fully consistent data (i.e. without experimental uncertainty), which had a complexity similar to the real mixing process. This ensured that the results of the model evaluation were also valid for the real HVAC unit. The performance of O-POD and G-POD was compared with reference simulations and the major differences between both methods were discussed. Based on the model evaluation, it was shown that the O-POD method was suitable to model mixing in HVAC units. Thus, the O-POD procedure was applied to the real HVAC unit and integrated into a system model in section 4.2. Measurements from the test rig were provided in section 4.2 as input for the POD to generate the O-POD model of the real HVAC unit. Experimental validation data was also used to assess the resulting HVAC model.

4.1 Numerical Benchmark Simulation

In this section, the performance of the O-POD procedure is evaluated and the differences between the traditional G-POD and O-POD method are shown. Since the Galerkin projection required spatially resolved flow fields (see section 2.4), a simplified mixing cavity was modeled. CFD simulations with different combinations of the valve positions were conducted to obtain the input data for the G-POD and the O-POD model. The G-POD method used the spatial flow fields for the POD. In contrast, the integral volume flow rates and

enthalpy flow rates at the outlets were calculated from the same simulations as input for the O-POD model (see subsection 2.3.2). Besides the input data, a second numerical data set was computed and the integral outlet values were calculated. This data set is known as test data. It contained valve combinations, which were not included in the input data for the POD. The accuracy of the integral enthalpy flow rates modeled by the G-POD method and by the O-POD procedure was then evaluated using the test data set. Furthermore, the resulting POD modes and weighting coefficients of G-POD and O-POD were analysed and compared with each other.

4.1.1 Physical Model

HVAC units consist of a blower, an evaporator, an heat exchanger (HX) and several ventilation ducts leading into the cabin. Since the focus of the investigation is the mixing cavity, the full system has been reduced to a simplified mixing cavity benchmark geometry. The two-dimensional generic cavity model consisted of two inlet ducts and three outlets as seen in Fig. 4.1.

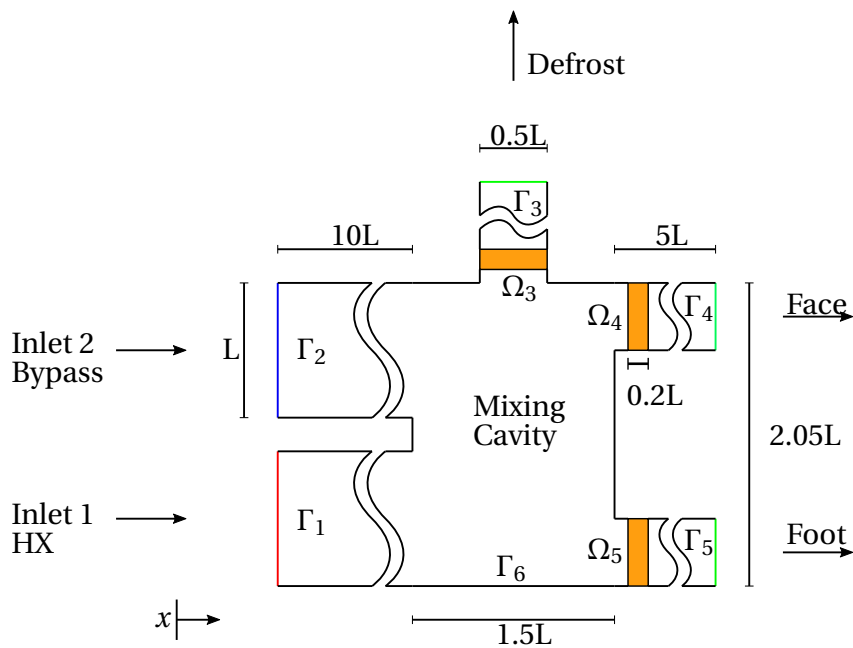


Figure 4.1: Two-dimensional HVAC model (orange: cell region Ω_n with flow resistance)

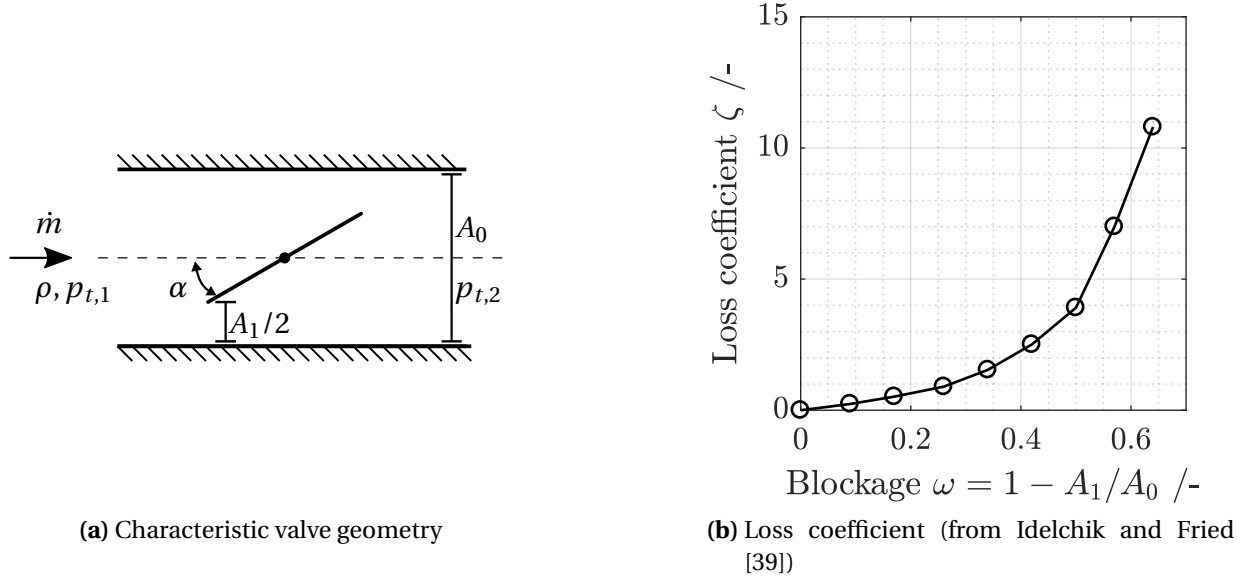


Figure 4.2: Loss of total head in a cylindrical butterfly valve

Inlet 1 represents the hot inflow from the HX. Inlet 2 supplies the mixing cavity with cold air. The length of both inlet channels have been chosen to $10L$ to guarantee independence of the numerical results in the mixing cavity from the boundary conditions. Corresponding to a real HVAC geometry, the outlets 3 to 5 referred to the defrost, face, and foot ducts.

In real HVAC units the distribution of the mass flow rates to the ventilation ducts is regulated by valves. Butterfly valves are commonly utilized. The characteristic geometry of a butterfly valve is shown in Fig. 4.2a. The valves were treated as a loss of total head, which was described by the the dimensionless loss coefficient ζ

$$\zeta = \frac{\Delta p_t A_0^2 \rho}{\dot{m}^2}. \quad (4.1)$$

The loss coefficient ζ is specified based on the modeled total pressure loss, the mass flow rate and the reference cross section as well as the reference density. In literature experimental data and correlations can be found to estimate the dimensionless loss coefficient ζ for different valve types and geometries [32, 39, 51, 56]. Fig. 4.2b shows the loss coefficient for different valve blockages ω .

Table 4.1: Boundary Conditions

Boundary	Velocity	Pressure	Temperature
Γ_1	U_0	$\nabla p \cdot \mathbf{n} = 0$	1
Γ_2	U_0	$\nabla p \cdot \mathbf{n} = 0$	0
$\Gamma_3, \Gamma_4, \Gamma_5$	$\nabla \mathbf{u} \cdot \mathbf{n} = 0$	$p = 0$	$\nabla T^+ \cdot \mathbf{n} = 0$
Γ_6	(0,0)	$\nabla p \cdot \mathbf{n} = 0$	$\nabla T^+ \cdot \mathbf{n} = 0$

The valves and actual blockages were not modeled to reduce the computational effort of the CFD simulations. Instead, the flow resistance of the subdomain Ω_3 , Ω_4 and Ω_5 (see Fig. 4.1) was varied using the loss coefficients shown in Fig. 4.2b. The flow field of the simplified mixing cavity was considered to be steady and incompressible. The mixing in the cavity was computed with RANS (see subsection 2.2.1).

The transport of the sensible enthalpy was reduced to that of a passive scalar T^+ to further simplify the benchmark simulation. The passive scalar T^+ denotes the dimensionless temperature

$$T^+ = \frac{T - T_{Bypass}}{T_{HX} - T_{Bypass}}. \quad (4.2)$$

A constant value of $20 \cdot 10^{-6} \text{ m}^2 \text{ s}^{-1}$ was used for the thermal diffusion coefficient D . Reynolds Analogy was employed to compute the turbulent diffusion coefficient according to $D_t = \nu_t Pr_t^{-1}$ with $Pr_t = 0.85$.

At both inlets Γ_1 and Γ_2 from Fig. 4.1 a mean velocity U_0 of 2.5 ms^{-1} was prescribed. This corresponds to a Reynolds number Re of 25,000 with $L = 0.1 \text{ m}$ and is a typical operating scenario for HVAC units. Further boundary conditions are summarized in Tab 4.1. The numerical simulations were performed using the open source tool OpenFoam. The $k-\omega$ -SST model and the Boussinesq assumption were utilized [65] as closure for the RANS Equations.

As stated in the introduction of this section, two data sets of numerical simulations were obtained. The first numerical data set was the POD input. This data set contained simulations for selected valve angles covering the relevant operating range of the HVAC unit. These angles and the respective loss coefficient are given in Tab. 4.2.

Table 4.2: Loss coefficient for different butterfly valve angles [39] applied as input for the POD

Angle α [°]	0	10	20	30	40
Loss Coefficient ζ [-]	0	0.52	1.54	3.91	10.8
Valve blockage R_1/R_0 [-]	0	0.17	0.34	0.5	0.64

Table 4.3: Loss coefficient for different butterfly valve angles [39] applied as reference to evaluate the POD models

Angle α [°]	5	15	25	35
Loss Coefficient ζ [-]	0.24	0.9	2.51	7
Valve blockage R_1/R_0 [-]	0.09	0.26	0.42	0.57

In total $5^3 = 125$ CFD simulations were performed using 5 valve angles at 3 outlets. For the G-POD method, the variables of the resulting flow fields were provided directly as observations. According to O-POD, the needed integral volume flow rates and enthalpy flow rates were computed from the numerical data set. Subsequently, the second numerical test data set was obtained to evaluate both methods. It contained numerical simulations for valve angles different to the POD input data. These positions are shown in Tab.4.3 resulting in $4^3 = 64$ CFD simulations. The integral values were computed from the simulations and applied as reference to evaluate the results of the G-POD model and O-POD model in subsection 4.1.2.

Following the O-POD procedure presented in subsection 2.3.2, the volume flow rates at the outlets were required. These volume flow rates were computed by the FR network model. The network model of the simplified mix-

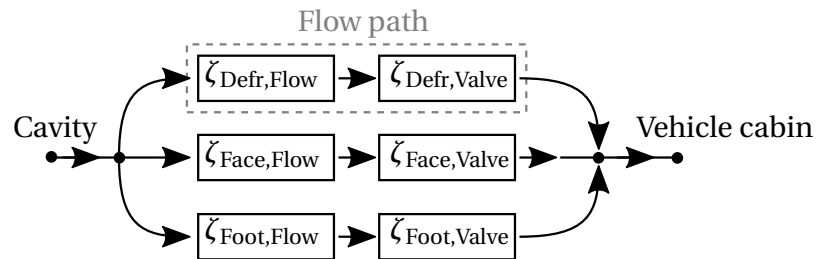


Figure 4.3: Flow resistance network

ing cavity is shown in Fig. 4.3. A constant density was considered. Each flow path was described by two loss coefficients $\zeta_{n,Flow}$ and $\zeta_{n,Valve}$. The valve losses $\zeta_{n,Valve}$ refer to the values given in Tab. 4.2 and Tab. 4.3. The coefficients $\zeta_{n,Flow}$ were introduced to increase the accuracy of the network model. To calibrate $\zeta_{n,Flow}$, the numerical data set for the POD input was used. The following optimization problem was solved to determine $\zeta_{n,Flow}$

$$\min_{\zeta_{n,Flow} \in R} |\dot{\mathbf{V}}_m^+ - \dot{\mathbf{V}}_{FR}^+(\zeta_{n,Flow})|. \quad (4.3)$$

4.1.2 Comparison of Galerkin Projection With O-POD Procedure

Two Reduced Order Models were generated from the numerical simulations of the last section. One with the O-POD approach and the other one based on the Galerkin procedure. The difference of the resulting POD modes, the truncation error and the performance of both models is evaluated below.

O-POD modes

The capability of the POD to reveal inherent mechanisms of correlated data can be analysed in particular by the modes of the O-POD procedure. These modes are the result of the POD procedure using the integral outlet values of the numerical data set. Accordingly to Eq.2.40 in subsection 2.3.2, the series expansion of the POD modes for the volume flow rates yields

$$\begin{aligned} \dot{\mathbf{V}}^+ &= \overbrace{\boldsymbol{\theta}_0^{\dot{\mathbf{V}}^+}}^{\text{Mean distribution}} + \overbrace{+a_1 \boldsymbol{\theta}_1^{\dot{\mathbf{V}}^+} + a_2 \boldsymbol{\theta}_2^{\dot{\mathbf{V}}^+} + a_3 \boldsymbol{\theta}_3^{\dot{\mathbf{V}}^+}}^{\text{Variational modes}} \\ \begin{pmatrix} \dot{V}_{Defr}^+ \\ \dot{V}_{Face}^+ \\ \dot{V}_{Foot}^+ \end{pmatrix} &= \begin{pmatrix} 0.31 \\ 0.33 \\ 0.36 \end{pmatrix} + a_1 \begin{pmatrix} 0.17 \\ 0.16 \\ -0.33 \end{pmatrix} + a_2 \begin{pmatrix} 0.71 \\ -0.71 \\ 0 \end{pmatrix} + a_3 \begin{pmatrix} -0.12 \\ -0.17 \\ 0.29 \end{pmatrix} \\ &\quad \Sigma = 1 \qquad \qquad \Sigma = 0 \qquad \qquad \Sigma = 0 \qquad \qquad \Sigma = 0 \end{aligned} \quad (4.4)$$

and for enthalpy flow rates follows

$$\begin{aligned}
 \begin{pmatrix} \dot{\mathbf{H}}^+ \\ \dot{\mathbf{H}}_{\text{Defr}}^+ \\ \dot{\mathbf{H}}_{\text{Face}}^+ \\ \dot{\mathbf{H}}_{\text{Foot}}^+ \end{pmatrix} &= \underbrace{\begin{pmatrix} \theta_0^{\dot{\mathbf{H}}^+} \\ 0 \\ 0.29 \\ 0.71 \end{pmatrix}}_{\text{Mean distribution}} + \underbrace{\begin{pmatrix} +a_1 \theta_1^{\dot{\mathbf{H}}^+} \\ +a_1 \begin{pmatrix} 0 \\ 0.64 \\ -0.64 \end{pmatrix} \\ +a_2 \theta_2^{\dot{\mathbf{H}}^+} \\ +a_2 \begin{pmatrix} 0.03 \\ -0.02 \\ -0.01 \end{pmatrix} \\ +a_3 \theta_3^{\dot{\mathbf{H}}^+} \\ +a_3 \begin{pmatrix} -0.75 \\ 0.49 \\ 0.26 \end{pmatrix} \end{pmatrix}}_{\text{Variational modes}} \\
 & \quad \Sigma = 1 \qquad \qquad \qquad \Sigma = 0 \qquad \qquad \qquad \Sigma = 0 \qquad \qquad \qquad \Sigma = 0
 \end{aligned} \tag{4.5}$$

In Eq. 4.4 and Eq. 4.5 the mode θ_0 denotes the mean average of the observations. This mode delivers a mean distribution of the respective quantity, e.g. the volume flow rates. Therefore, the sum of the entries for the defrost, face and foot outlet is 1. Higher modes from θ_1 to θ_{N_r} can be described as variational modes. These modes lead to a change of the volume flow rates or enthalpy flow rates at the outlets but do not affect the total mass or energy balance. The sum of their entries is 0 since the POD modes maintain mass and energy conservation. Each mode corresponds to an individual change of the volume flow rates and enthalpy flow rates at the outlets, which can be seen by analyzing the mode values. This is shown using the first volume flow rate mode as example

$$\theta_1^{\dot{\mathbf{V}}^+} = \begin{pmatrix} \theta_1^{\dot{\mathbf{V}}_{\text{Defr}}^+} \\ \theta_1^{\dot{\mathbf{V}}_{\text{Face}}^+} \\ \theta_1^{\dot{\mathbf{V}}_{\text{Foot}}^+} \end{pmatrix} = \begin{pmatrix} 0.17 \\ 0.16 \\ -0.33 \end{pmatrix} \longrightarrow \begin{pmatrix} \text{Defrost} \\ \text{Face} \\ \updownarrow \\ \text{Foot} \end{pmatrix}. \tag{4.6}$$

This mode leads to a change of the volume flow rate from the foot to the defrost and face outlet. The difference in the volume flow rate at the foot outlet is almost equally distributed to the defrost and face outlet. The deviation of the actual flow distribution from the mean distribution $\theta_0^{\dot{\mathbf{V}}^+}$ can be calculated by using the result \mathbf{V}_{FR}^+ of the fluid resistance network model

$$\Delta \dot{\mathbf{V}}^+ = \dot{\mathbf{V}}_{FR}^+ - \theta_0^{\dot{\mathbf{V}}^+}. \tag{4.7}$$

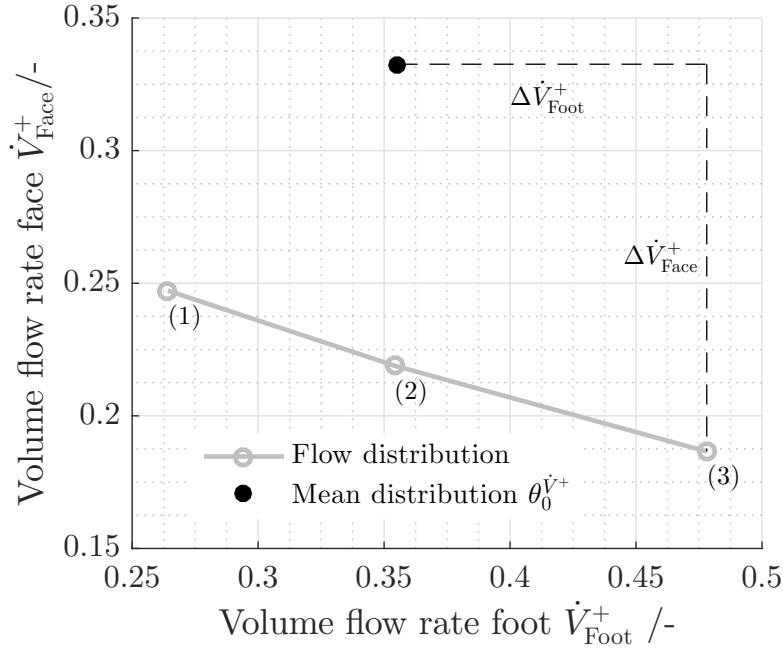


Figure 4.4: Deviation of the actual flow distribution from the mean distribution

In Fig. 4.4 the flow distribution of three operating conditions (1 to 3) from the numerical model are shown. These operating conditions serve as example to discuss the effect of changing the volume flow rates on the weighting coefficients. The volume flow rate at the foot outlet of the first operating condition is less than the mean distribution and increases for the second and third flow distribution. In contrast, the face volume flow rates of all shown operating conditions are smaller than the mean distribution. Furthermore, the difference between the mean distribution and the flow distribution (3) is highlighted. Based on the change of the volume flow rates shown in Fig. 4.4 the weighting coefficients are estimated by the O-POD method.

The resulting coefficients can be seen in Fig.4.5 for the first and second mode. The coefficients of the first mode decrease by increasing the volume flow rate at the foot outlet. This is because the first mode describes a change of the volume flow rates between the foot outlet and the other outlets (see Eq. 4.6). For the same reason, the first coefficient is almost 0 for the second operating condition (2) because the deviation of the volume flow rate at the foot outlet from the mean distribution is approximately 0. The second mode leads to a

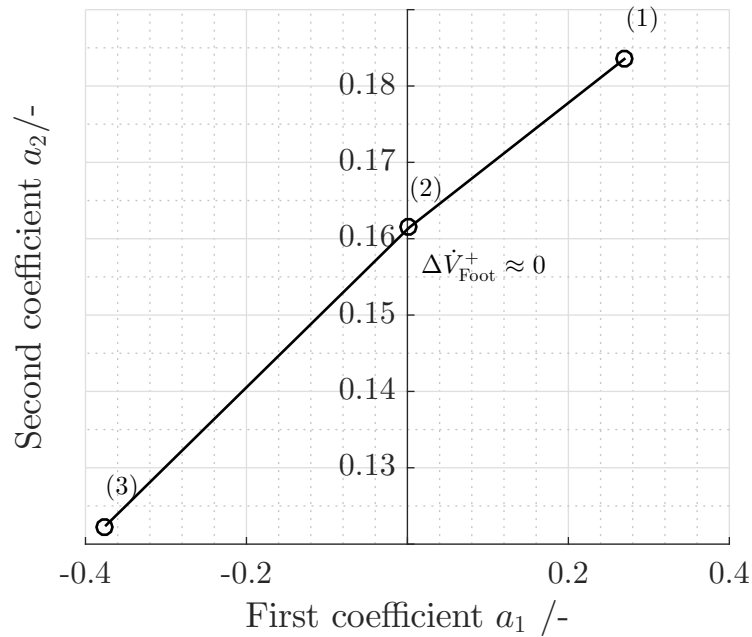


Figure 4.5: Weighting coefficients for the three operating conditions of Fig 4.4

change between the defrost and face outlet. Thus, this coefficient scales with an increased volume flow rate at the face outlet. The individual deviation from the mean distribution introduced by a specific mode is calculated by $a_i\theta_i$ and illustrated in Fig. 4.6 for the three operating conditions.

While the first mode influences the flow distribution at all outlets, the second mode has no significant effect on the volume flow rate at the foot outlet. Moreover, the change of the volume flow rates between the operating conditions introduced by the second mode is smaller than the change by the first mode. This is because the modes are sorted according to their information content (see section 2.1) and the first mode covers most of the information. The superposition of the individual changes of the volume flow rates by the modes is shown in Fig. 4.7. Only two modes are sufficient to reconstruct the volume flow rates with minor errors to the exact flow distribution.

The exact deviation of the enthalpy flow rates from the mean distribution is unknown due to different outlet temperatures. But it can be used that the modes for the volume flow rates and enthalpy flow rates are linked with each

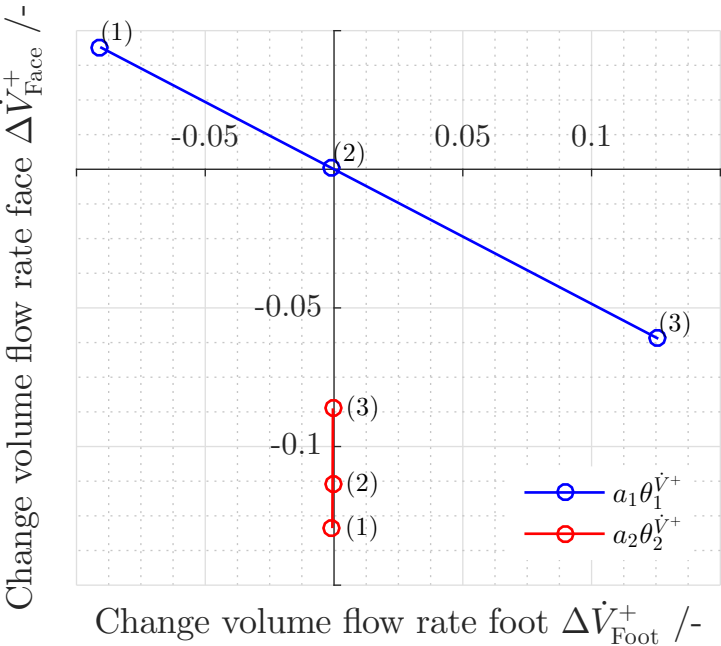


Figure 4.6: Change of the flow distribution introduced by the modes

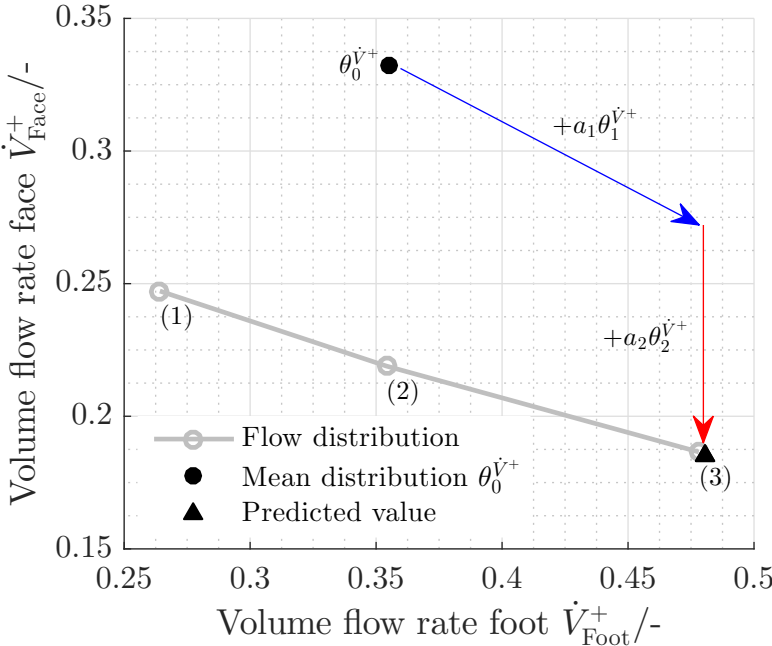


Figure 4.7: Superposition of the weighted POD modes for the volume flow rates

other due to the same weighting coefficients of the POD modes

$$\begin{array}{ccc}
 \begin{pmatrix} \Delta \dot{V}_{\text{Defr}}^+ \\ \Delta \dot{V}_{\text{Face}}^+ \\ \Delta \dot{V}_{\text{Foot}}^+ \end{pmatrix} & = a_1 \begin{pmatrix} \text{Defrost} \\ \text{Face} \\ \Downarrow \\ \text{Foot} \end{pmatrix} + a_2 \begin{pmatrix} \text{Defrost} \\ \Downarrow \\ \text{Face} \end{pmatrix} & \\
 \downarrow & \downarrow & \downarrow \\
 \text{Exact} & \text{Deviation} & \text{Deviation} \\
 \text{deviation} & \text{1st mode} & \text{2nd mode} \\
 \text{unknown} & \text{(RIC 85 \%)} & \text{(RIC 99.7 \%)} & (4.8) \\
 & \downarrow & \downarrow \\
 \begin{pmatrix} \Delta \dot{H}_{\text{Defr}}^+ \\ \Delta \dot{H}_{\text{Face}}^+ \\ \Delta \dot{H}_{\text{Foot}}^+ \end{pmatrix} & = a_1 \begin{pmatrix} \text{Face} \\ \Downarrow \\ \text{Foot} \end{pmatrix} + a_2 \begin{pmatrix} \text{Defrost} \\ \Downarrow \\ \text{Face} \\ \text{Foot} \end{pmatrix} &
 \end{array}$$

Instead of estimating the exact deviation of the enthalpy flow rates from the mean value, only the individual changes of the most dominant modes are considered. The series expansion of these modes lead to the approximate change of enthalpy flow rates for an unknown operating condition as shown in Fig.4.8. In this figure it can also be seen that the second mode has almost no influence on the enthalpy flow rates. As shown in Eq. 4.6, the values for the enthalpy flow rates of the second modes are small (< 0.03). Accordingly, this mode does not lead to a significant change of the enthalpy flow rates. The POD modes reveal that the most important mechanism of the mixing process (1st mode) reflects a change of the volume flow rate from the foot outlet to the other outlets. But this change of the volume flow rate leads only to a difference of the enthalpy flow rates between the face and foot outlet because the temperatures at the outlets are different.

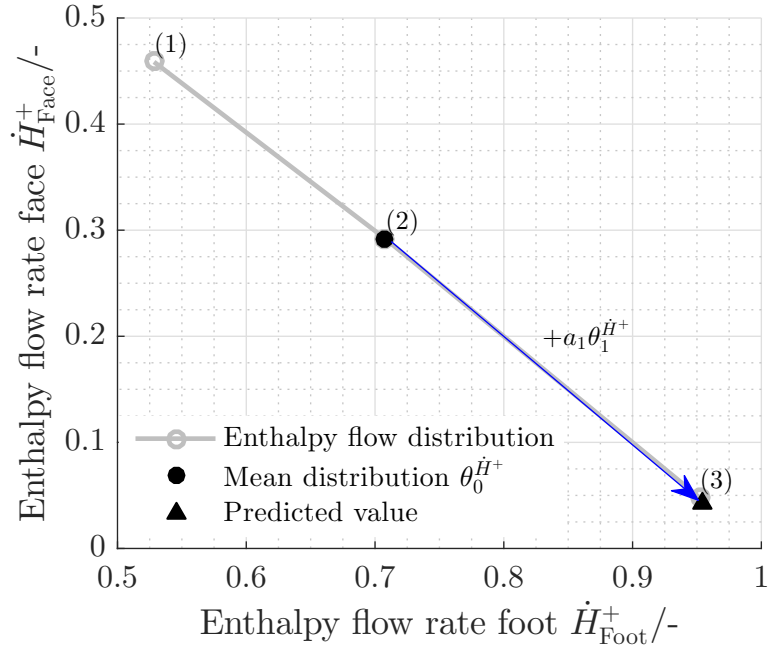


Figure 4.8: Reconstruction of the enthalpy flow rates

G-POD modes

The modes used for the G-POD method reflect the spatial changes of the flow variables as the POD was performed with the complete flow fields. For each flow variable, e.g. velocity or temperature, a G-POD mode is generated (see subsection 2.2.1). As an example, the temperature modes are analysed below. These modes are shown in Fig. 4.9. The zeroth temperature mode θ_0^T describes again the mean distribution for the temperature. The higher modes θ_1^T and θ_2^T are the variational modes. It is shown that the general appearance of the modes is similar. Temperature gradients occur at the mixing layer of the cold and warm inflows. The modes θ_1^T and θ_2^T lead particularly in this region to a deviation from the mean distribution. The relation of the integral volume flow rates and enthalpy flow rates is less obvious due to the spatial distribution of the field variables at the outlets. Further post-processing of the modes would be necessary for an analysis. These POD modes contain more information than required since the spatial distribution of the temperature is not needed. Regarding climate control, the increased information content has not a significant advantage.

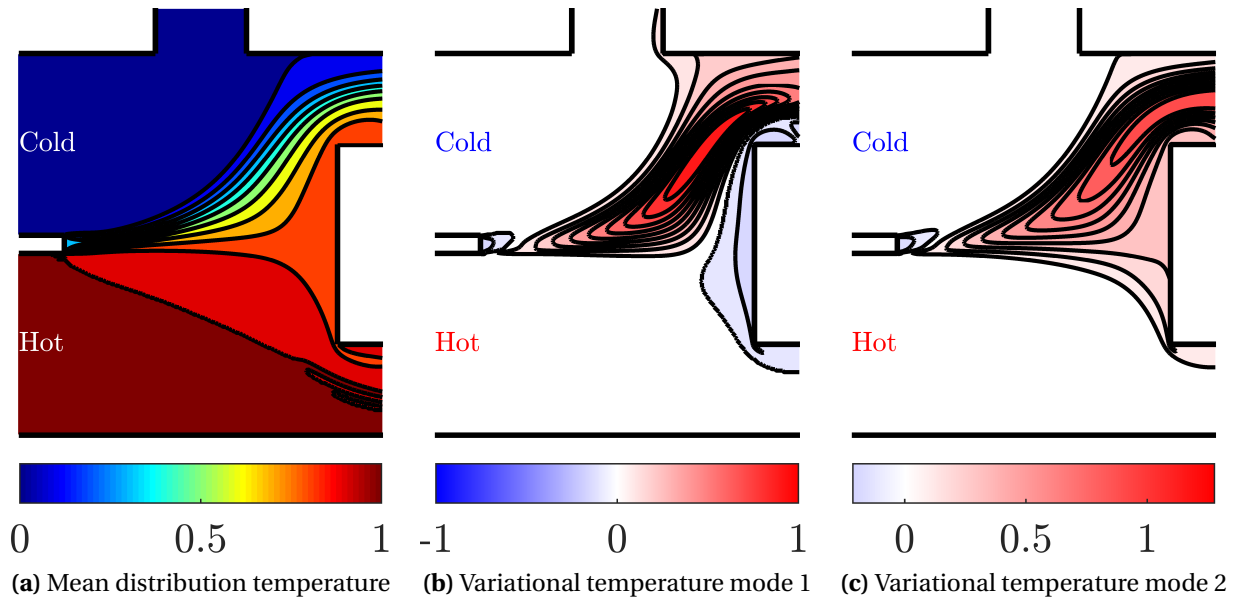


Figure 4.9: Isolines of the temperature mean distribution (4.9a), temperature mode 1 (4.9b) and temperature mode 2 (4.9c).

Truncation error

As it is seen, the dimension of the G-POD modes is much higher than the dimension of the O-POD modes. Therefore, the information content of the modes from both procedures is compared with each other. The Relative Information Content (RIC) is shown for the POD modes of both procedures in Fig. 4.10. It can be seen that the O-POD procedure requires only 3 modes to reach a RIC of $\geq 99.9\%$, while for the G-POD procedure 7 modes are needed for an equal RIC. This difference can be explained by the different data base, which is used to construct the POD modes. The G-POD procedure aims to capture the most significant information from the spatial flow fields as shown in Fig. 4.9. More modes are needed to reconstruct the high dimensional flow fields in comparison to the O-POD method, which extracts only the most dominant features from the integral outlet values. The DOF of the flow field modeled by the G-POD procedure is 168480 times higher than the dimension of the integral values used of the O-POD method. Since the dimensionality of the data base is different for both procedures, the RIC is not a suitable measure for a comparison of the POD methods with each other. Thus, only the prediction capability of the integral volume flow rates and enthalpy flow rates are discussed below.

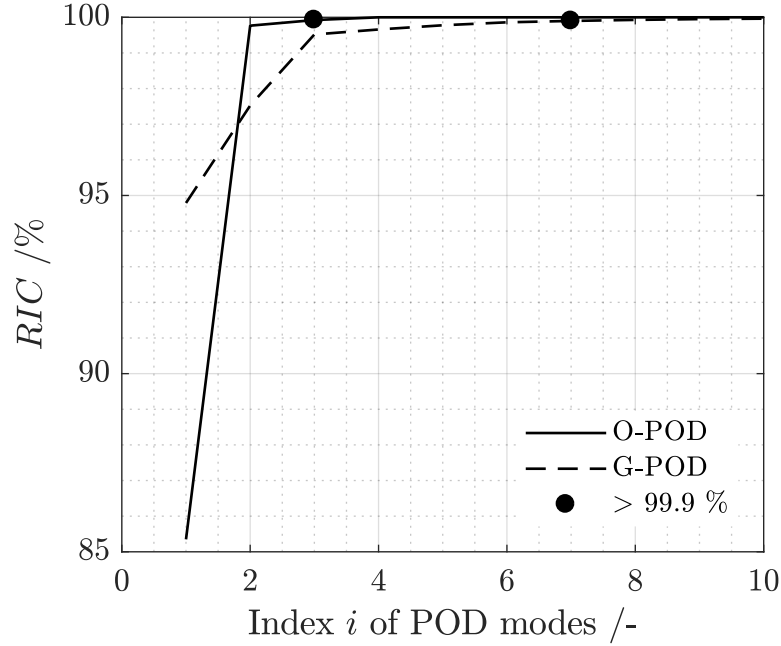


Figure 4.10: Eigenvalue spectrum

The numerical data set used as input for the POD is applied for an evaluation. For this data set, the exact weighting coefficients are available from Eq. 2.7 in section 2.1. Thus, a deviation of the reconstructed integral enthalpy flow rates from the CFD reference can be accounted to the number of modes used. The error of the respective model is given by

$$\epsilon^{H^+} = \sum_{n=1}^N |\dot{H}_{n,\text{Model}}^+ - \dot{H}_{n,\text{CFD}}^+|, \quad (4.9)$$

where $\dot{H}_{n,\text{Model}}^+$ denotes the modeled enthalpy flow rate at the outlet and $\dot{H}_{n,\text{CFD}}^+$ refers to the reference value from the CFD simulation. In Fig. 4.11 the truncation error of the reconstructed integral enthalpy flow rates for both procedures are shown. For this purpose, the mean error μ_ϵ and maximum error is calculated. The mean error follows as

$$\mu_\epsilon = \frac{1}{N_s} \sum_{m=1}^{N_s} \epsilon^{\dot{H}^+}(m). \quad (4.10)$$

The mean error of the O-POD method is < 0.02 by using only 2 modes. In con-

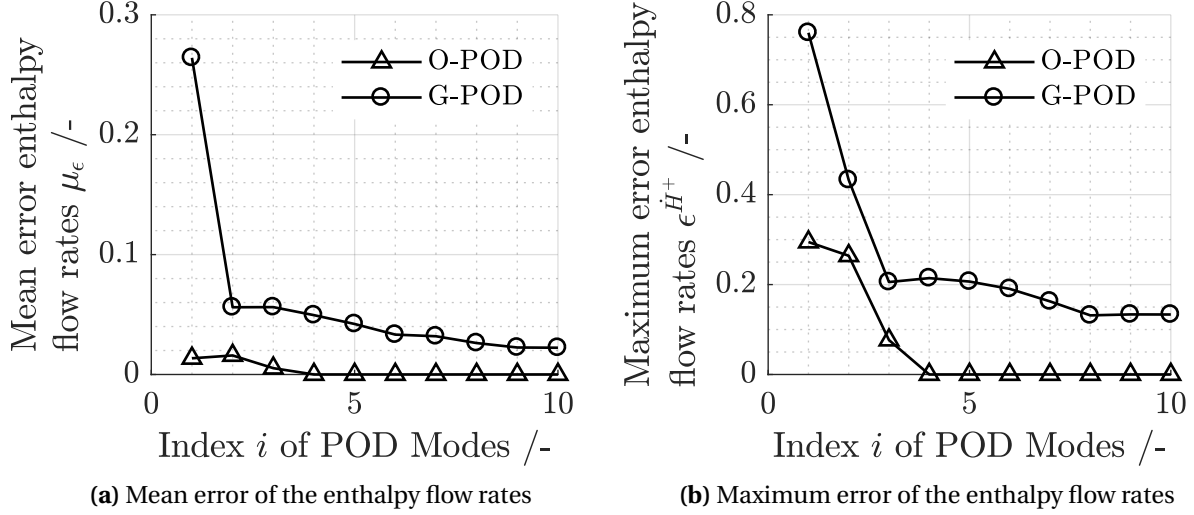
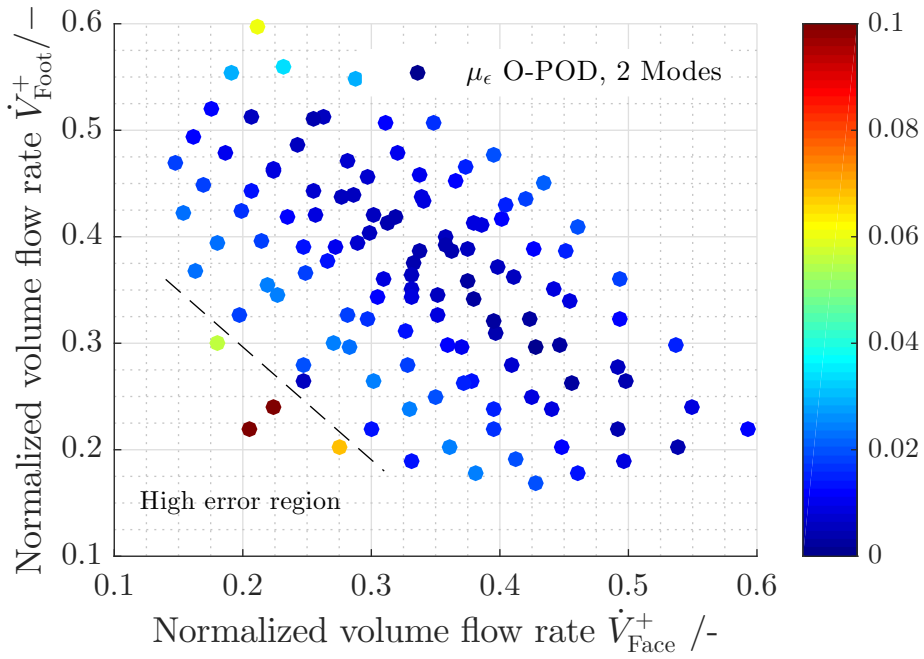


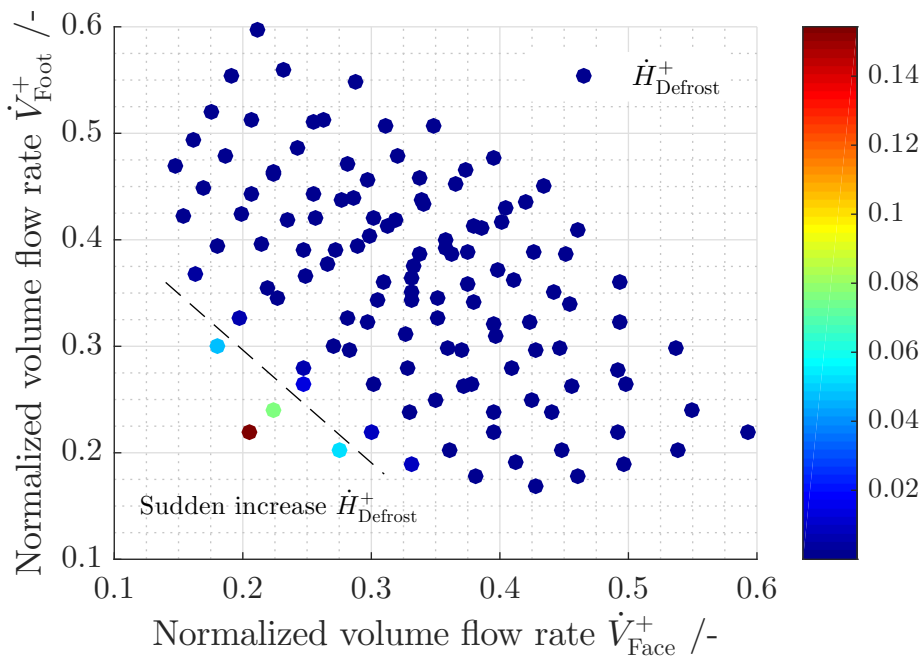
Figure 4.11: Maximum and mean truncation error of the observations for the enthalpy flow rates by O-POD procedure and Galerkin method

trast, the G-POD procedure requires 9 modes to reach a similar error margin. With 4 modes all observations of the O-POD approach are reconstructed exactly. With the G-POD procedure even 10 modes are not sufficient to exactly represent the input data set. As for the RIC vs. mode result, this can be explained by the higher dimensionality of the G-POD modes covering the complete flow field and not only the outlet region of the mixing cavity. Comparing Fig. 4.11a and 4.11b for the O-POD method, it is seen that the modes contribute differently to the accuracy of the reconstructed enthalpy flow rates. Between 1 and 2 modes, only the maximum error decreases slightly. The mean error is almost unaffected. Increasing the number of modes to 3, the maximum error decreased significantly. Additionally, it is seen that for both procedures the maximum error is high in comparison to the mean error.

The error distribution of the O-POD method using 2 modes is illustrated in Fig. 4.12a for a detailed analysis. The error $\mu_\epsilon^{H^+}$ is shown in colors for the combinations of volume flow rates at the face and foot outlets. The overall error distribution is low (< 0.03). Larger errors are seen only at low volume flow rates at the face and foot outlets. The operating condition with the maximum error is the same for both POD models. For this operating condition the flow resistances at the outlets were prescribed as $\zeta_{\text{Defr}} = 0$, $\zeta_{\text{Face}} = 540$ and $\zeta_{\text{Foot}} = 540$.



(a) Error distribution of the O-POD procedure with 2 modes



(b) Dimensionless enthalpy flow rate at the defrost outlet

Figure 4.12: Error distribution of the O-POD procedure and dimensionless enthalpy flow rate at the defrost outlet for varying volume flow rates

The resistances at the face and foot outlets are high while the resistance at the defrost outlet is low. The defrost outlet is mostly fed by the cold bypass because of the small distance between the bypass inlet and defrost outlet and the two-dimensional domain. But for this operating condition, the enthalpy flow rate at the defrost outlet increases suddenly as shown in Fig. 4.12b. In this figure the dimensionless enthalpy flow rate is illustrated for varying volume flow rates at the face and foot outlets. The volume flow rate at the defrost outlet is fed by both the hot air flow from the HX and the cold air flow from the bypass due to the high resistances at the other outlets. This significant change of the systems output behavior for few operating conditions is not predicted accurately by neither the O-POD nor G-POD procedure. Fig. 4.12b also indicates an important mechanism of the mixing process of the two-dimensional cavity. The enthalpy flow rate at the defrost outlet remains very small for almost all observations. Consequently, a change of the volume flow rates particularly has an influence on the enthalpy flow distribution at the face and foot outlets. This is in good agreement with the analysis of the O-POD modes. As stated above, the first O-POD mode reveals this mechanism and is crucial for the mixing process. This demonstrates the strength of the O-POD method for data analysis.

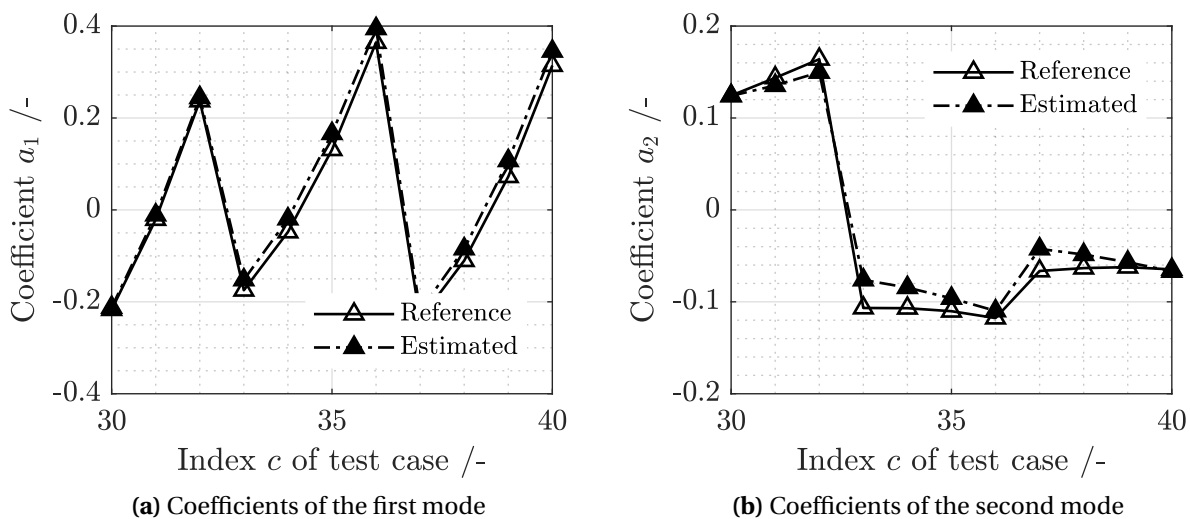


Figure 4.13: Reference coefficients and estimated weighting coefficients by the O-POD procedure of the first (4.13a) and second mode (4.13b)

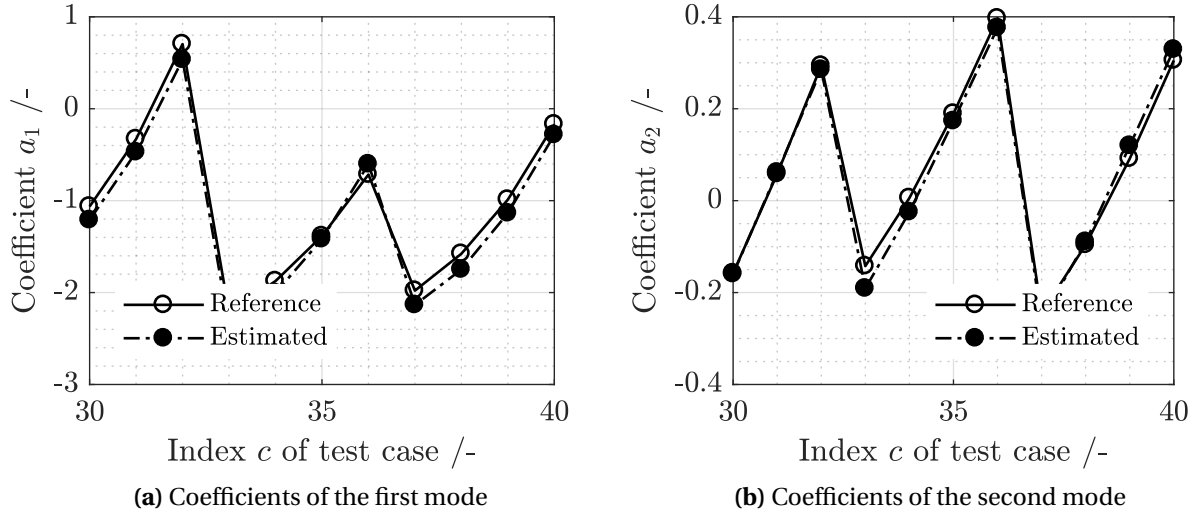


Figure 4.14: Reference coefficients and estimated weighting coefficients by the G-POD procedure of the first (4.14a) and second mode (4.14b)

Prediction accuracy

The accuracies of both ROM approaches are now compared with each other using the test data set. This data set includes numerical simulations of valve combinations different to the POD input. In Fig. 4.13 and 4.14 the estimated weighting coefficients of the O-POD procedure and the G-POD approach are shown. For the comparison, the exact weighting coefficients are computed as reference by using the test data set. It can be seen that both approaches predict the coefficients with good accuracy. This indicates that reliable results can be expected.

The mean error of the enthalpy flow rates is shown in Fig. 4.15 for the O-POD method and G-POD procedure to compare the accuracy. The G-POD procedure requires 7 POD modes for a similar accuracy while only 2 modes are needed using the O-POD method. As described in chapter 2, the number of POD modes used with the O-POD is limited by the degree of freedom (DOF) of the provided equation system. Applied to the benchmark model shown in Fig. 4.1, the DOF is 2 because only at two outlets the volume flow rates can vary independently due to mass conservation. The error increases significantly exceeding the permissible number of modes because the equation system is overdetermined.

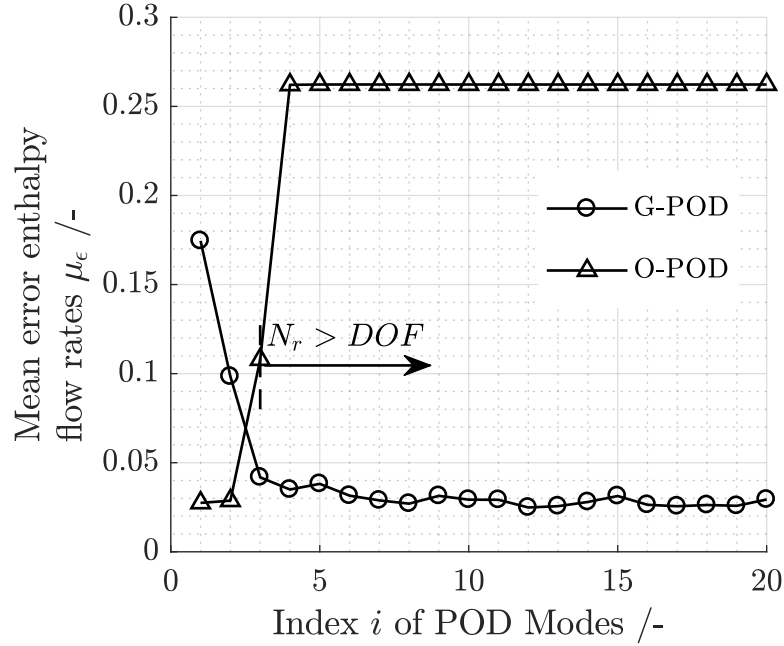


Figure 4.15: Comparison of the error for the test cases between the O-POD method and the G-POD approach

This can be seen in Fig. 4.15 where the error increases using more than 2 modes. This limitation of the POD modes is not a major drawback since few dominant modes describe the system with high accuracy (< 0.04).

The number of modes has an impact on the computational effort to calculate the enthalpy flow rates. The mean prediction time \bar{t} is calculated to give an estimate for the computational effort

$$\bar{t} = \frac{1}{N_c} \sum_{c=1}^{N_c} t_c, \quad (4.11)$$

where N_c denotes the numbers of test cases and t_c is the required time to solve the equation system and reconstruct the the flow variables for a specific test case. The computation is conducted with a single core at 2.7 GHz and 32 Gb RAM on a 64 bit platform. The mean prediction time is compared for both methods in Fig. 4.16. While the O-POD method requires 0.02s to estimate the enthalpy flow rates with two modes, for the same number of modes 0.03s are needed with the G-POD procedure. However, the G-POD method models the

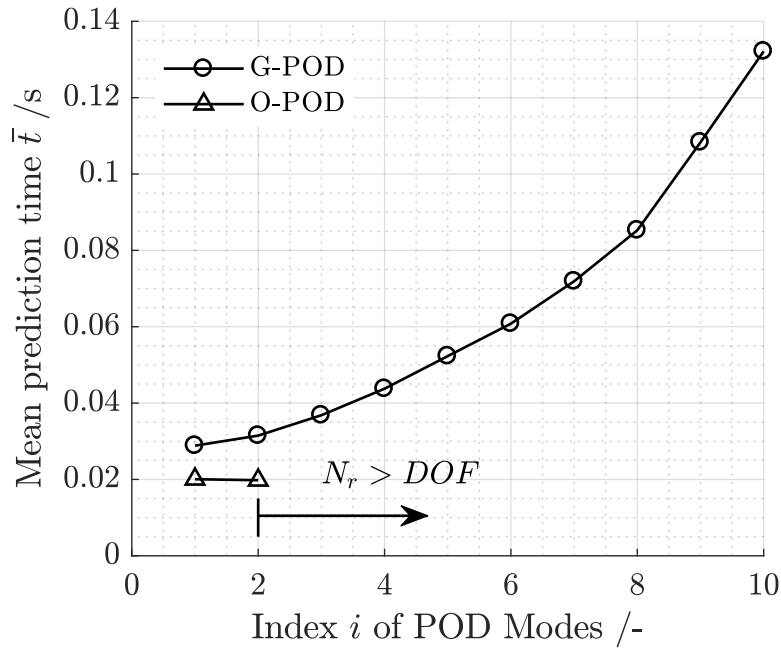


Figure 4.16: Average time to reconstruct enthalpy and volume flow rates at the outlets

full complexity of the flow field and provides results with high accuracy. Considering that numerical simulations of the real HVAC unit require approximately 5 hours[55], the G-POD method can be seen as a powerful method if distributed flow variables are needed.

Based on these results, the following conclusions from the comparison can be made to model the integral outlet values of the benchmark model:

- Significant changes of the system behavior, which are not sufficiently represented by the data set for the POD, lead to an increased error by both O-POD and G-POD. The data selection is therefore important for an accurate low dimensional description.
- The G-POD procedure requires more modes for a similar accuracy of the enthalpy flow rates at the outlets. Each mode carries less information of the output values than the O-POD method due to the high-dimensionality of the spatial flow field.

- Both procedures require low computational effort to estimate the weighting coefficients. Considering that the G-POD method generates a ROM for the complete flow field, this method can be seen as an efficient alternative to numerical simulations.
- Due to different outlet temperatures, the enthalpy flow rates scale non-linearly with the volume flow rates. Inherent physical features of the relation between volume flow rates and enthalpy flow rates can be obtained by analyzing the modes of the O-POD method. The series expansion includes the mean distribution and variational modes. Each variational mode corresponds to an individual deviation from the mean distribution. The variational modes of the volume flow rates and enthalpy flow rates are linked with each other by the weighting coefficients. Due to this link, the change of volume flow rates can be directly related to a change of the enthalpy flow rates.

The O-POD procedure shows good performance to model the integral enthalpy flow rates at the outlets of HVAC units. The resulting ROM has high accuracy. Furthermore, experimental data can be applied as input for the POD, which is shown in the following section to generate the O-POD model for the real HVAC unit.

4.2 HVAC Model

The O-POD procedure was applied to model the real HVAC unit studied experimentally as detailed in chapter 3. In the first subsection, the system model and the integration of the O-POD model is described. This is followed by an assessment of the resulting HVAC model in the second subsection.

4.2.1 Modeling Approach

The aim of the system model was to describe the remaining components of the HVAC unit and to integrate the O-POD approach.

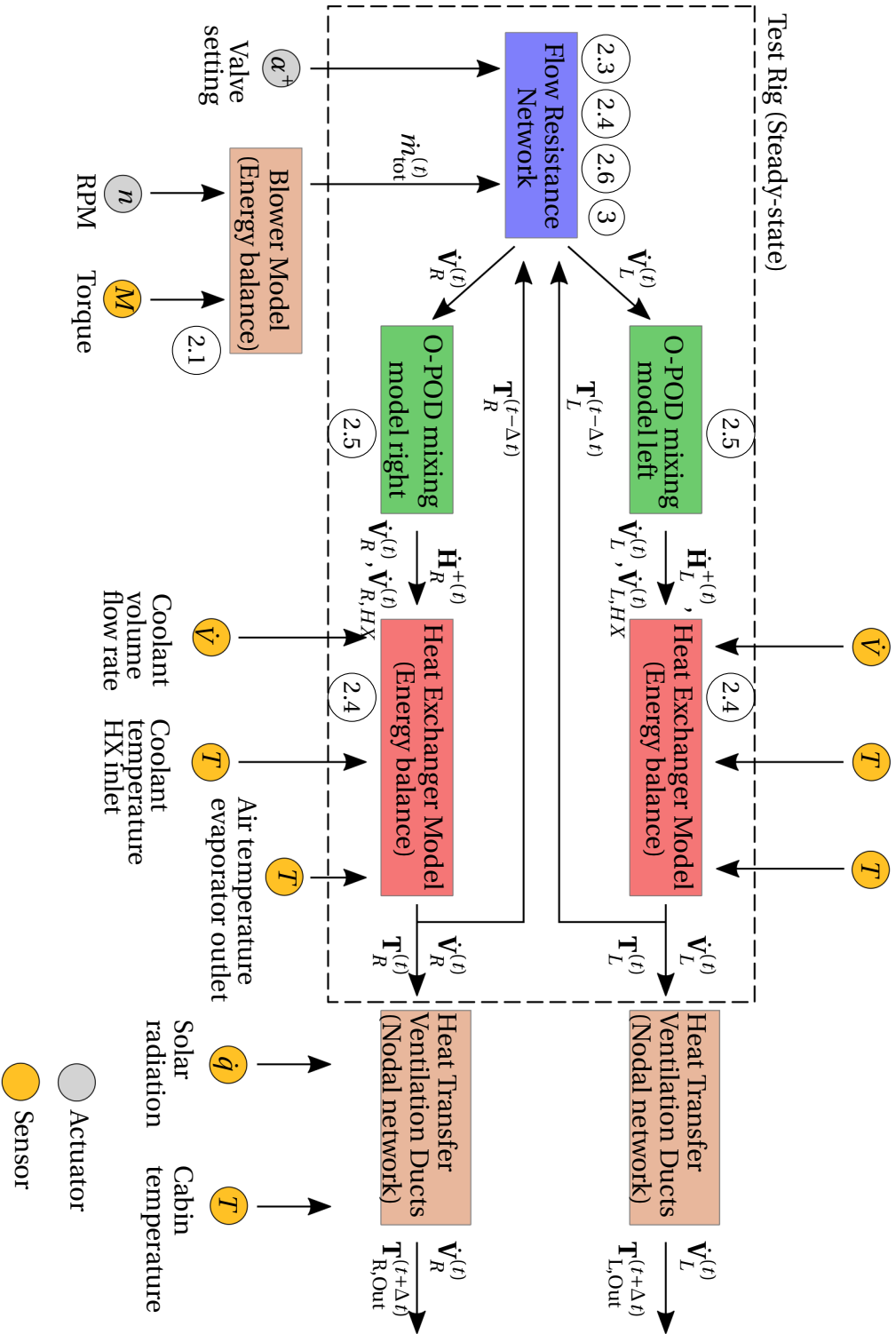


Figure 4.17: Sub-models and signal flow of the HVAC unit model (the numbers refer to the components in Fig. 3.1 modeled by the respective sub-model).

These components were the blower, the heat exchanger and the ventilation ducts with heat transfer. They are discussed below.

The signal flow between these sub-models is illustrated in Fig. 4.17. The evaporator was not included in the modeling approach since the air temperature downstream of the evaporator is generally measured in vehicles to protect the evaporator from icing. This temperature value was applied as bulk temperature of the total air inflow. The system simulation and sub-models are explained below following Fig. 4.17. A description of the sub-models is given in the appendix A. The numbers in Fig. 4.17 are equivalent to the numbers in Fig. 3.2 to highlight the components modeled by the respective sub-model.

The total mass flow rate \dot{m}_{tot} was determined experimentally at the test rig. But this was not possible in the test vehicle because of missing measuring hardware (see section 3.2). Therefore, the total inflow was calculated by a blower model for the application of the HVAC model to the car. This blower model was based on an energy balance using performance data of the blower, the RPM and the torque M .

The total mass flow rate calculated was then provided as input for the FR network model. This network model represented the air distribution system and is shown in Fig. 4.18. It was used to compute the distribution of the air volume flow rate through HX, bypass and the outlets based on the valve positions.

The resistance network had two major flow branches. Each flow branch referred to the left or right climate zone and contained the individual losses induced by the bypass or flow through the HX (1) and the valves and ducts of the air distribution system (2). Since changes of density had influence on the air distribution, inner iterations of the HVAC model were performed until the difference of the volume flow rates at all outlets between the last and actual iteration felled below 10^{-5} . Usually, 2 iterations were sufficient to reach this criterion. The density of the last time step was used as initial value.

These mass flow rates were provided as input values for the O-POD model following the approach developed in chapter 2. The HVAC unit had two mixing cavities (see chapter 3).

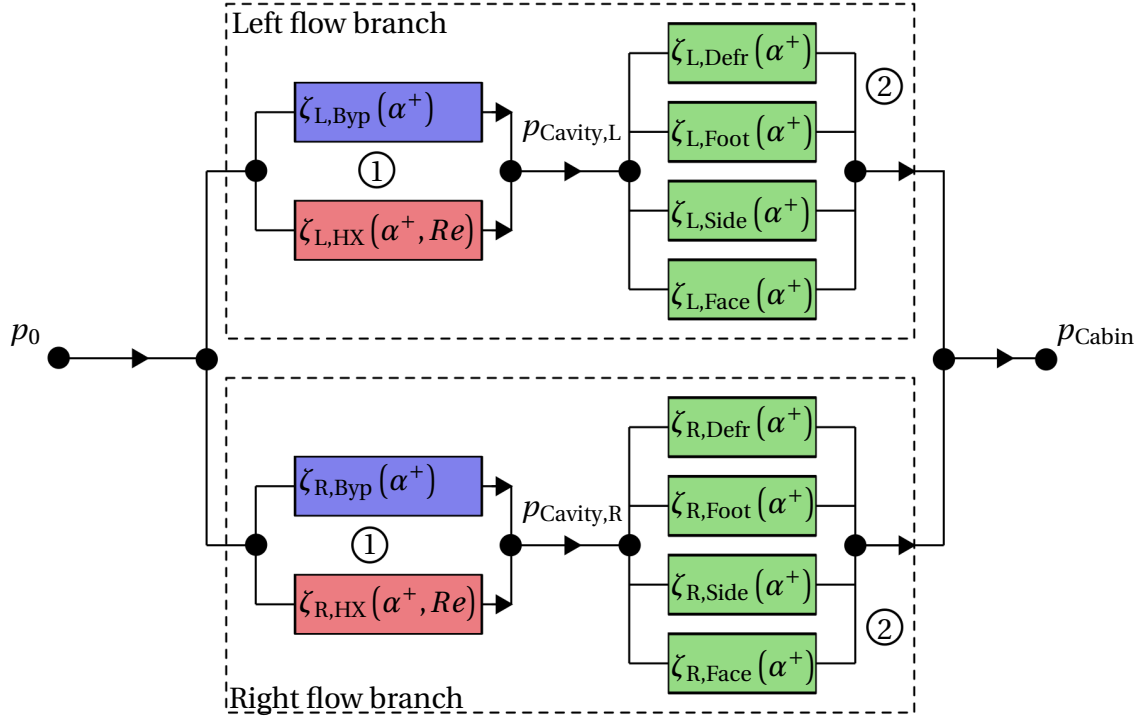


Figure 4.18: Flow resistance network of the HVAC unit

An individual O-POD model was generated for each mixing cavity. These O-POD models calculated the dimensionless enthalpy flow rates at the outlets, which were needed in the next step by the HX model.

The HX model computed the total heat transfer in the HX by using an energy balance together with a look-up table for the HX efficiency. For this purpose, the air mass flow rate through the HX, the volume flow rate of the coolant and the coolant temperature at the HX inlet was provided by sensors. Then, the outlet temperatures of the HVAC unit were evaluated from the total heat transfer, the mass flow rates at the outlets and the dimensionless mass flow rates. The outlet temperatures were fed back to the FR network to account for variations in density.

A nodal network of the discretized ventilation ducts and surrounding dashboard geometry modeled heat transfer in the left and right side ducts. Mod-

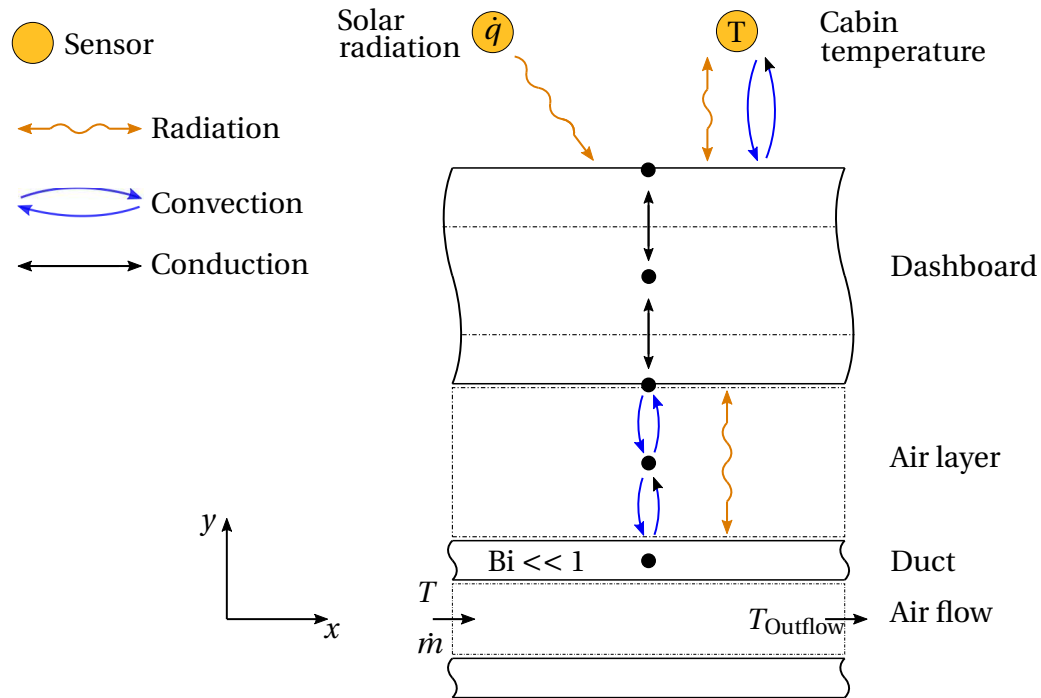


Figure 4.19: Nodal network of the ventilation ducts and surrounding material layers

eling the heat transfer was in particular important for the application of the HVAC model to the vehicle in section 5.1. In the car, the ducts had no thermal insulation and heat transfer was expected. The nodal network is shown in Fig. 4.19. The dashboard was discretized by three volumes and an explicit finite-difference scheme was applied. Heat transfer in the defrost, foot and face ducts was not considered because of their small length. Nusselt correlations from literature ([39, 40, 64]) were used for the convective heat transfer. The thermal properties of the dashboard and the duct were applied from Flieger [30] and Ghebru [31], respectively.

The O-POD model generated from the test rig measurements can easily be applied to different vehicles due to this hybrid, i.e. physical FR network coupled with O-POD mixing model, approach. An identical HVAC unit is frequently utilized for different vehicle versions for economy of makers. With the pro-

Table 4.4: Modifications to apply the HVAC model from the test rig to different vehicles using the same HVAC unit

	Test Rig	Vehicle A	Vehicle B
Blower Model	\dot{m}_{tot} measured (see subsection 3.1.2)	No modifications required	
Fluid Resistance Network	Loss coefficients measurement channels	Loss coefficients ventilation ducts A	Loss coefficients ventilation ducts B
O-POD Model	No modifications required		
Heat Exchanger Model	No modifications required		
Nodal Network	Not required due to measurement channels	Geometrical parameters ventilation ducts A	Geometrical parameters ventilation ducts B

posed combination of modeling procedures only those models need to be modified, which depend on the specific vehicle configuration. Hence, minor parameter adaptations may be required for the FR network and the nodal network while keeping the O-POD description of the mixing cavity. As a consequence, the test rig measurements are obtained only once for a specific HVAC unit to generate the O-POD model. This O-POD model can then be used for different vehicle versions with an identical HVAC unit. In Tab. 4.4 the required model modifications to apply the proposed HVAC model to different vehicles are summarized.

4.2.2 Model Assessment

The model quality is assessed comparing model results with measurements from the test rig. Similar to the numerical benchmark model, an experimental test data set was acquired. This test data set was used as reference. It included operating conditions, which were different to the experimental data provided as POD input. In particular, the temperature control curve (TCC) [77] is used for the comparison. The TCC is a characteristic measurement procedure commonly applied in the design process of HVAC units. To obtain the TCC, the air distribution valves have a constant position and only the angle of the mix-

Table 4.5: Test cases for the model validation

Parameter	Case 1	Case 2
Left/Right defrost position	31 % / 31 %	
Left/Right face position	45 % / 45 %	45% / 0 %
Left/Right side position	100 % / 100 %	
Left/Right foot position	67 % / 67 %	
Total air mass flow rate \dot{m}_{tot}	4 kg min ⁻¹	
Air temperature outlet evaporator T_{Evap}	10 °C	
Coolant temperature inlet HX T_{HX}	70 °C	
Coolant volume flow rate HX T_{HX}	25 L min ⁻¹	

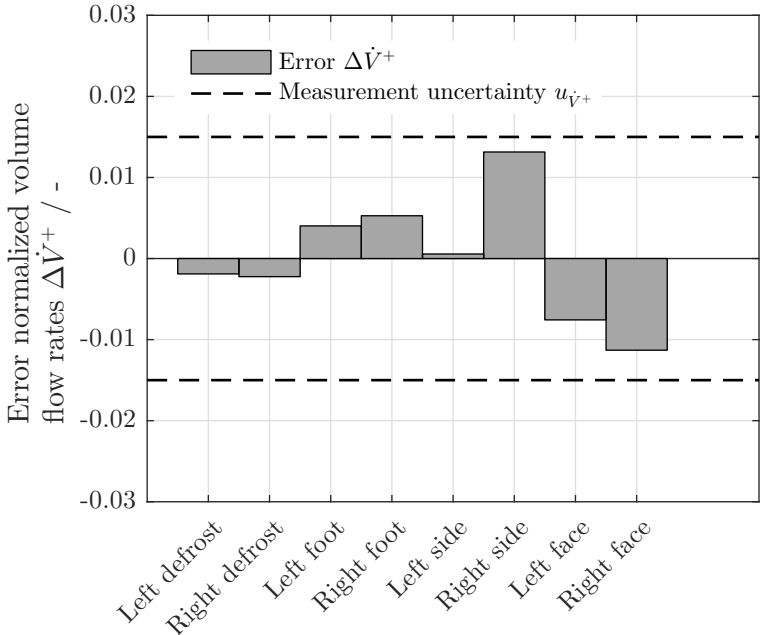
ing valves is varied. This results in a specific change of the temperatures at the cabin outlets due to the non-trivial mixing phenomena in the mixing cavity. In Tab. 4.5 the two test cases used for the model assessment are shown. In Case 1 the positions of the air distribution valves are symmetrical for both climate zones of the HVAC unit. In the second test case, the valve face right is closed and the rest of the parameters is identical. For these two operating conditions, the positions of the mixing valves varies in steps of 5%. The second case reflects in particular the complex operating conditions resulting from individual passenger input who might shut off one of the outlets for their personal comfort.

Fluid Resistance Network

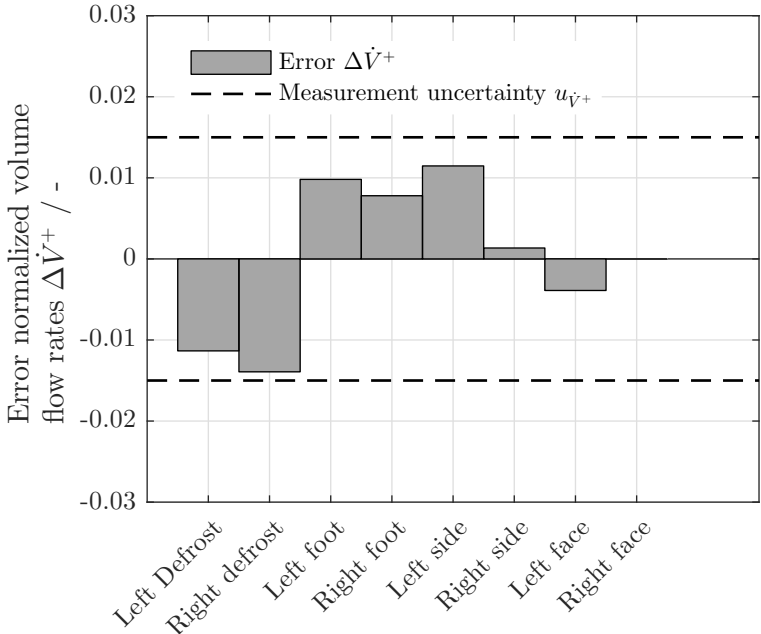
In Fig. 4.20 the error of dimensionless volume rates at the outlets are shown for case 1 and case 2, respectively. The error is calculated by

$$\Delta \dot{V}_n^+ = \dot{V}_{Exp.,n}^+ - \dot{V}_{FR,n}^+, \quad (4.12)$$

where $\dot{V}_{Exp.,n}^+$ refers to the measured value and $\dot{V}_{FR,n}^+$ to the modeled value from the FR network. Furthermore, the measurement uncertainty $u_{\dot{V}^+}$ of the volume flow rates at the outlets is illustrated in these figures. The error of the volume flow rates is less than the measurement uncertainty for both operating conditions. The accumulated absolute error at the outlets results in 0.05 for test case 1 and 0.06 for test case 2. Hence, the FR network provides accurate results and input values for the O-POD model and HX model.



(a) Test case 1



(b) Test case 2

Figure 4.20: Error of the dimensionless volume flow rates at the outlets

O-POD Model

Two experimental databases, an original and an extended data set, were available as input for the O-POD model. The extended data set was introduced in subsection 3.1.4 to improve the accuracy over a large operating range of the HVAC unit and to capture asymptotic behavior. The RIC of the POD modes for both data sets is shown in Fig. 4.21. The POD modes from the extended data set carry less information in comparison to the modes generated with the original data set. The Degree of Freedom (DOF) of the equation system of the O-POD model is 4, because the volume flow rates at the 3 outlets and the flow through the HX can be varied independently. The RIC of both databases are above 99.9% for this mode number. Based on the RIC, the databases are equivalent in their information content at 4 modes. The prediction performance of the O-POD models generated from these two data bases are compared with each other in Fig. 4.22 and Fig.4.23. The accumulated error is computed for this comparison according to

$$\epsilon^{\dot{H}^+} = \sum_{n=1}^N \left| \dot{H}_{Exp,n}^+ - \dot{H}_{POD,n}^+ \right|. \quad (4.13)$$

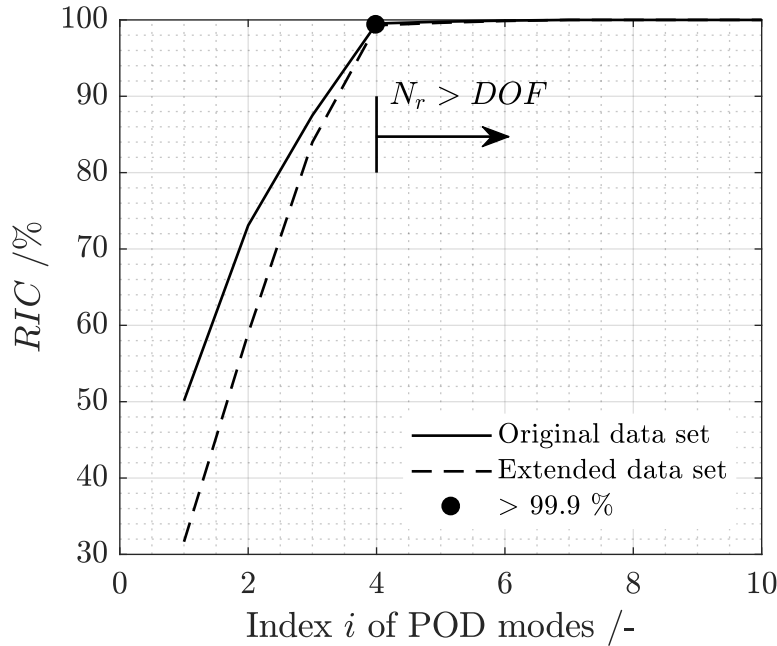


Figure 4.21: RIC using the original and extended data set

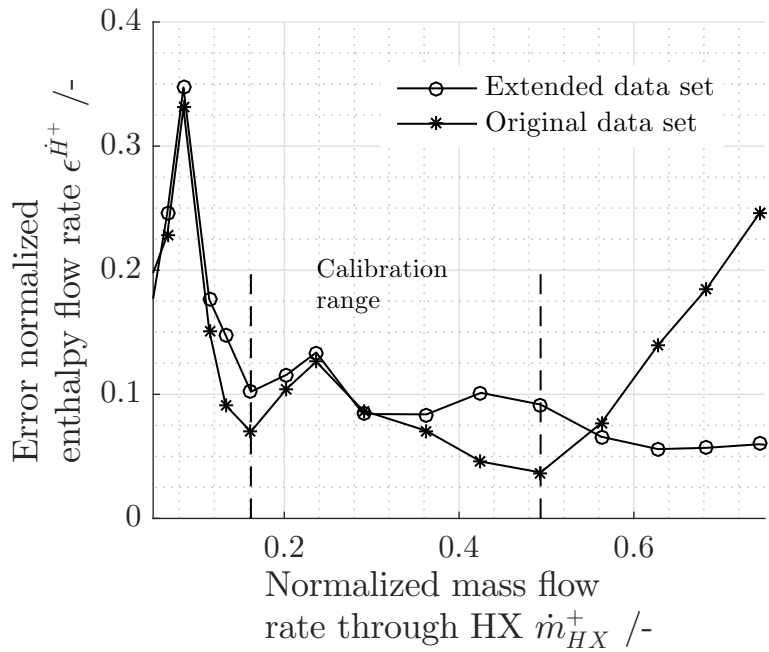


Figure 4.22: Error of the enthalpy flow rates for test case 1

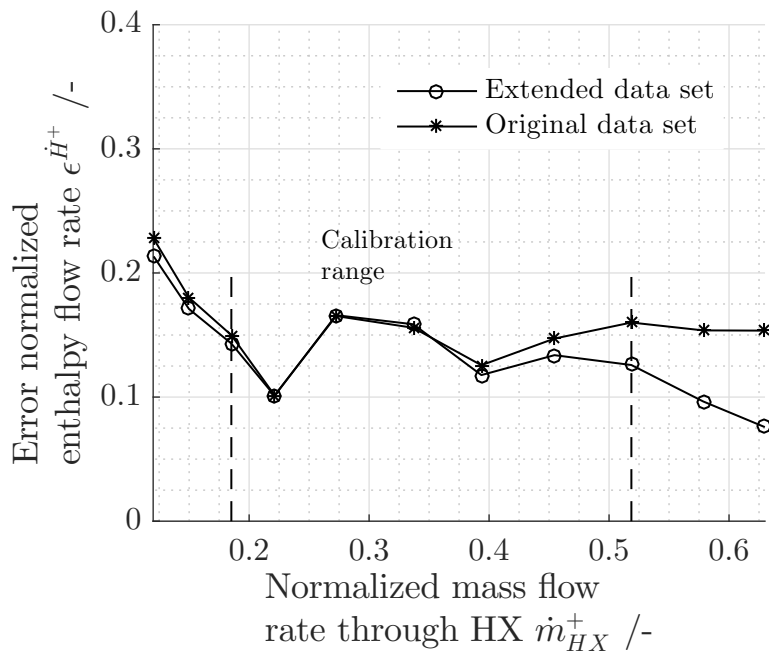


Figure 4.23: Error of the enthalpy flow rates for test case 2

Outside of calibration range at low mass flow rates through the HX, the error is high for both models. But this is not a major drawback, because most of the

air flows through the bypass and the heat input Q_{HX} is very low. The error remains low for the extended data base outside of calibration range at high flow rates through the HX while the error increases significantly using the original data set. This reflects the observations made above in the simplified numerical benchmark simulation (Fig. 4.12a) and motivates manipulating the original data set based on physical assumptions. This ensures the proper asymptotic behavior of the ROM. Hence, the POD modes from the extended experimental data set are used for further modeling. The general error margin of both test cases is approximately 0.1 over a wide operating range.

In Fig. 4.24 the absolute error of predicted and measured enthalpy flow rate at the outlets is illustrated. Similar to the accumulated error, high error margins (> 0.05) occur at low flow rates through the HX outside of calibration range. For the rest of the operating conditions ($\dot{m}_{HX}^+ > 0.18$), the error is less than 0.05 at each outlet. The error is evenly distributed between the outlets. This is important to avoid high temperature error occurrence at the outlets.

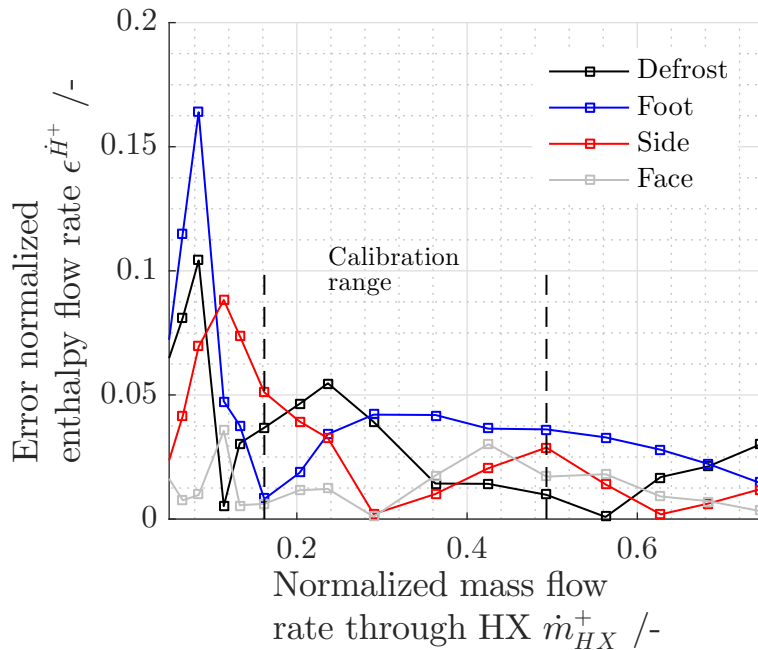


Figure 4.24: Absolute error of the enthalpy flow rates at the right climate zone outlets for test case 1 using the extended data set

The POD modes from the extended data set for the left climate zone of the HVAC unit are

$$\begin{aligned}
 & \begin{pmatrix} \dot{\tilde{V}}_{\text{HX}}^+ \\ \dot{\tilde{V}}_{\text{Defr}}^+ \\ \dot{\tilde{V}}_{\text{Foot}}^+ \\ \dot{\tilde{V}}_{\text{Side}}^+ \\ \dot{\tilde{V}}_{\text{Face}}^+ \end{pmatrix} = \underbrace{\begin{pmatrix} 0.47 \\ 0.19 \\ 0.24 \\ 0.24 \\ 0.33 \end{pmatrix}}_{\text{Mean distribution}} + \underbrace{\begin{pmatrix} 0.70 \\ -0.02 \\ -0.02 \\ 0 \\ 0.04 \end{pmatrix}}_{\text{Change flow through HX}} + a_1 + \underbrace{\begin{pmatrix} 0.07 \\ 0.11 \\ 0.25 \\ 0.24 \\ -0.60 \end{pmatrix}}_{\text{Change flow distribution outlets}} + a_2 + \underbrace{\begin{pmatrix} -0.03 \\ 0.29 \\ -0.49 \\ 0.3 \\ -0.1 \end{pmatrix}}_{\text{Change flow distribution outlets}} + a_3 + \underbrace{\begin{pmatrix} -0.05 \\ -0.50 \\ -0.05 \\ 0.51 \\ 0.04 \end{pmatrix}}_{\text{Change flow distribution outlets}} + a_4 \\
 & \hspace{15em} (4.14)
 \end{aligned}$$

and

$$\begin{aligned}
 & \begin{pmatrix} \dot{\tilde{H}}_{\text{Defr}}^+ \\ \dot{\tilde{H}}_{\text{Foot}}^+ \\ \dot{\tilde{H}}_{\text{Side}}^+ \\ \dot{\tilde{H}}_{\text{Face}}^+ \end{pmatrix} = \underbrace{\begin{pmatrix} 0.20 \\ 0.29 \\ 0.20 \\ 0.31 \end{pmatrix}}_{\text{Mean distribution}} + \underbrace{\begin{pmatrix} -0.05 \\ -0.09 \\ 0.06 \\ 0.08 \end{pmatrix}}_{\text{Change flow through HX}} + a_1 + \underbrace{\begin{pmatrix} 0.09 \\ 0.31 \\ 0.19 \\ -0.59 \end{pmatrix}}_{\text{Change flow distribution outlets}} + a_2 + \underbrace{\begin{pmatrix} 0.39 \\ -0.58 \\ 0.29 \\ -0.1 \end{pmatrix}}_{\text{Change flow distribution outlets}} + a_3 + \underbrace{\begin{pmatrix} -0.5 \\ -0.05 \\ 0.47 \\ 0.08 \end{pmatrix}}_{\text{Change flow distribution outlets}} + a_4 \\
 & \hspace{15em} (4.15)
 \end{aligned}$$

It can be seen in Eq. 4.14, that the value of the flow through the HX for the first volume flow rate mode $\theta_1^{\dot{\tilde{V}}^+}$ is high (0.7) in comparison with the value of the other modes (0.07, -0.03 and -0.05). This indicates that the first mode describes particularly the influence of the volume flow rate through the HX on the volume flow rate distribution and enthalpy flow rate distribution at the outlets. Changing the volume flow rate through the HX does not significantly

affect the flow rate distribution at the outlets. This is because the flow rates at the outlets are mainly determined by the valves at the outlets and not by the mixing valves. For this reason, the values corresponding to the volume flow rates at the outlets of the first mode $\theta_1^{\dot{V}^+}$ are very small (-0.02, -0.02, 0 and 0.04). In contrast, the influence on the enthalpy flow rate distribution is higher. Varying the flow rate through the HX results in a change of the enthalpy flow rates from the defrost and foot outlets to the side and face outlets. The POD modes θ_2 to θ_4 contain the influence of the flow distribution on mixing.

It can be expected that the weighting coefficient of the first mode scales with the mass flow rate through the HX, since a change of the hot inflow requires particularly a different weighting of this mode. In Fig. 4.25 and Fig. 4.26 the weighting coefficients are shown. The value of the first coefficient varies almost linearly with the mass flow rate through the HX. The coefficient a_1 crosses 0 at a normalized mass flow rate through the HX \dot{m}_{HX} of approximately 0.47. This flow rate is almost equal to the value from the mean distribution $\theta_0^{\dot{V}^+}$. The deviation from the mean distribution is very small and the weighting coefficient a_1 results in 0.

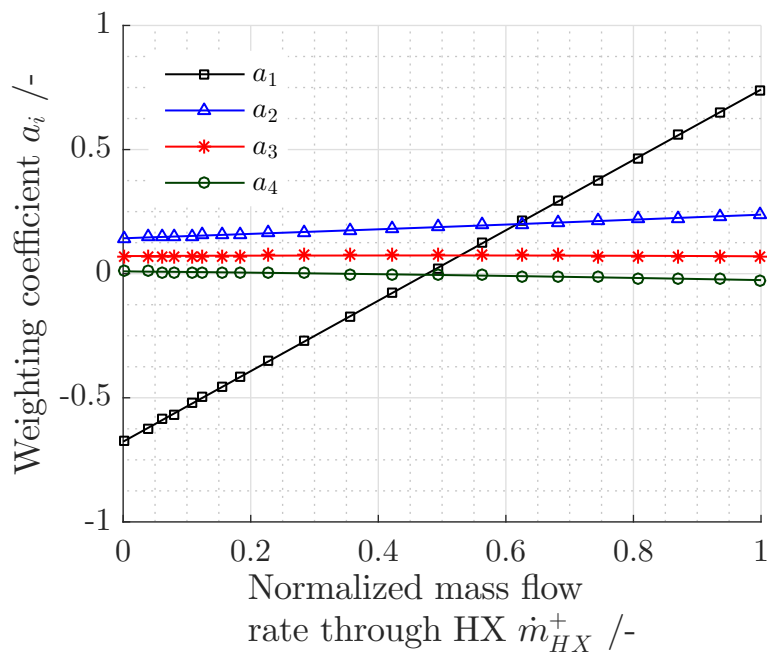


Figure 4.25: Weighting coefficients a_i of the right climate zone for test case 1

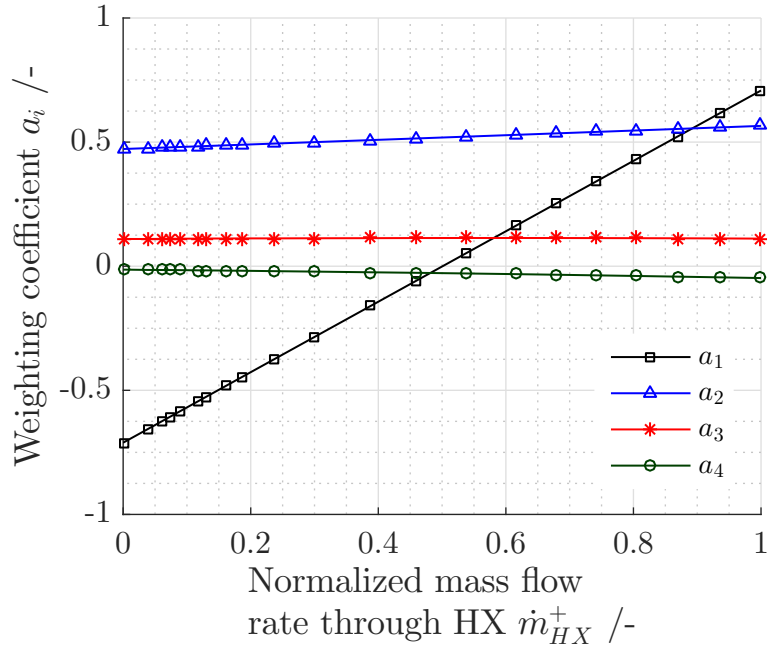


Figure 4.26: Weighting coefficients a_i of the right climate zone for test case 2

Furthermore, it is seen in Fig. 4.25 and in Fig. 4.26 that the weighting coefficient a_1 is almost identical for both test cases although the flow distribution at the outlets is different. Since the first mode describes particularly the change of the flow rate through the HX, this coefficient is almost independent of the flow distribution and operating condition of the air distribution valves. Changing the inflow of the HX has consequently no significant impact on the modes 2 to 4. Therefore, these coefficients remain almost constant as illustrated in Fig. 4.25 and Fig. 4.26. But the weighting coefficients a_2 to a_4 vary between the different test cases, because the flow distribution at the outlets is different. This has an impact on the weighting coefficients a_2 to a_4 . Particularly the coefficient a_2 is influenced by the face outlet valve, which is different in test cases 1 and 2. The change of the enthalpy flow rates at the outlets introduced by the flow rate through the HX is depicted in Fig. 4.27. The individual change of the enthalpy flow rates by the first mode is calculated from

$$\Delta \dot{H}_1^+ = a_1 \boldsymbol{\theta}_1^{\dot{H}^+}. \quad (4.16)$$

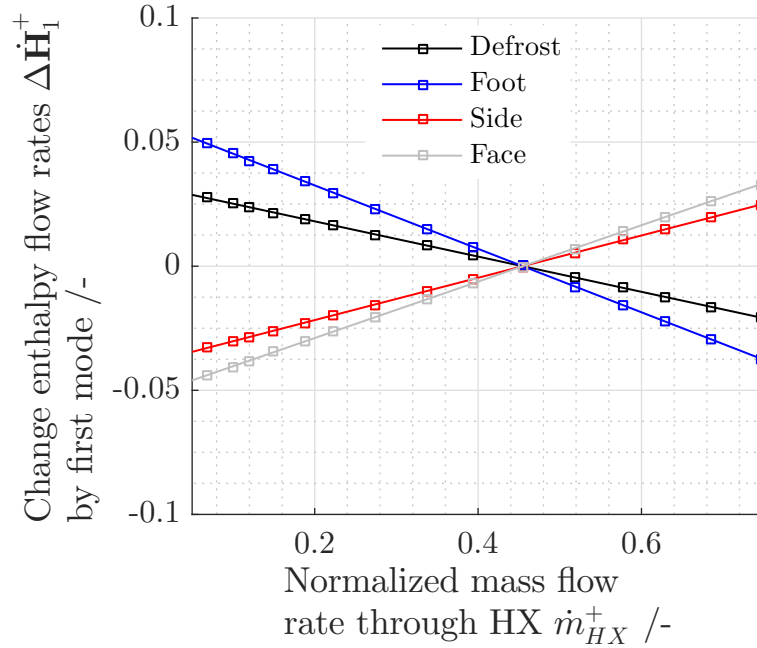


Figure 4.27: Influence of the flow through the HX on the mixing process

It can be seen that the influence of the flow through the HX on the enthalpy flow rate distribution is < 0.06 and linear. If the mixing process would depend non-linearly on the HX inflow at least two modes would be required to model this process. For this reason, three POD modes (2,3,4) reflect the influence of the flow distribution at the outlets on the mixing process. The relation between flow distribution and enthalpy flow rates at the outlets is non-linear due to different outlet temperatures and more POD modes are required for modeling.

Heat Exchanger Model

The heat transfer in the HX is illustrated for test case 1 and test case 2 in Fig. 4.28 and Fig. 4.29, respectively. The experimental value is calculated from the flow distribution, total mass flow rate and temperatures at the outlets

$$\dot{Q}_{HX} = \sum_{n=1}^N \dot{m}_{tot} \dot{m}_n^+ c_p (T_{n,Exp} - T_{Evap}). \quad (4.17)$$

It can be seen that the heat transfer in the HX is overestimated for all test cases.

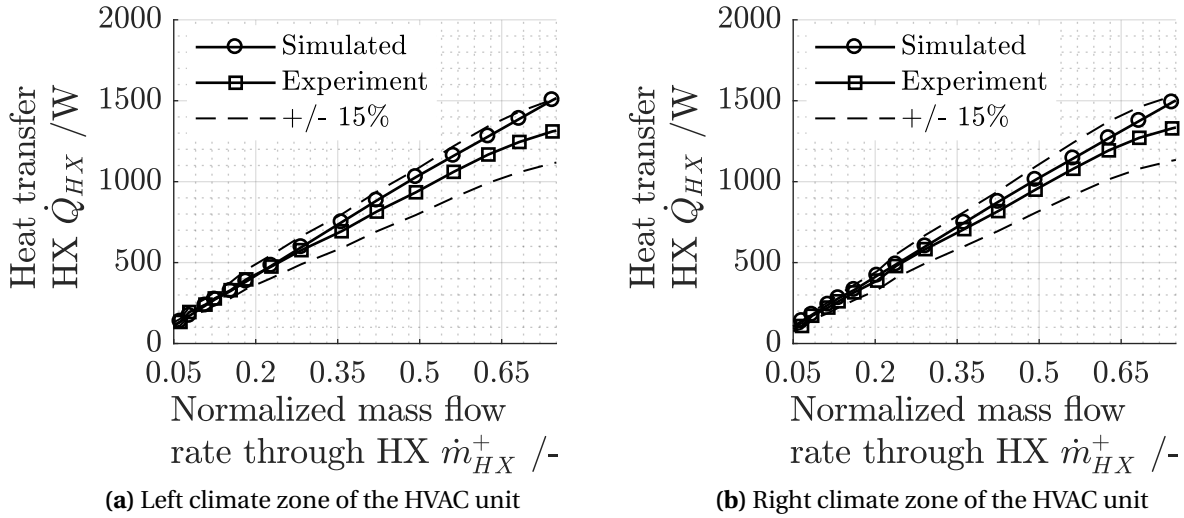


Figure 4.28: Heat transfer \dot{Q}_{HX} in the HX at the left and right climate zone of the HVAC unit for test case 1

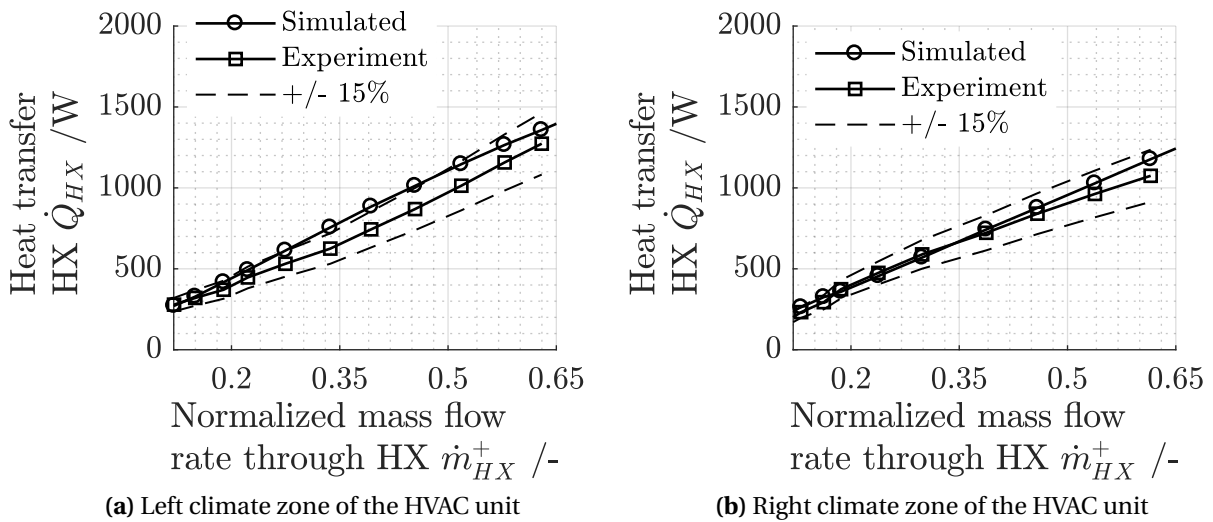


Figure 4.29: Heat transfer \dot{Q}_{HX} in the HX at the left and right climate zone of the HVAC unit for test case 2

This is a result of the different valve positions for this operating condition. The right face valve is closed. Thus, the mass flow rate and the heat transfer at the right zone drop. The error of the predicted heat transfer is < 15 % of the measured value. However, heat transfer in the HVAC unit before entering the

measurement channels is not considered in Eq. 4.17. This might explain an overestimated heat transfer by the HX model.

System Model

The absolute error between the outlet temperatures predicted by the HVAC unit model and the experiment are illustrated in Fig.4.30 for test case 1 and in Fig.4.31 for test case 2.

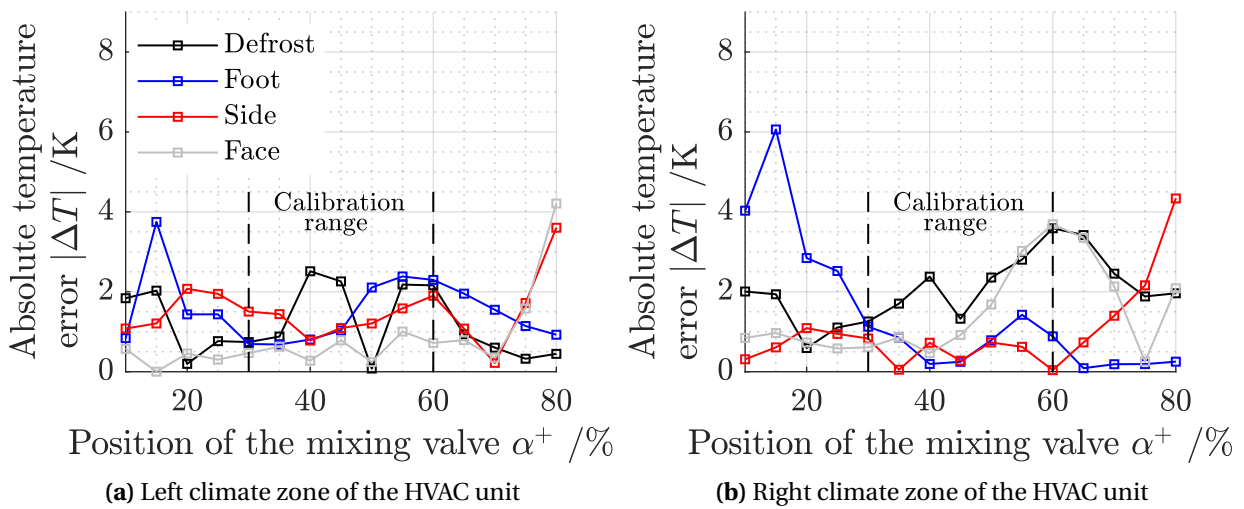


Figure 4.30: Temperature error for test case 1 using the extended data set

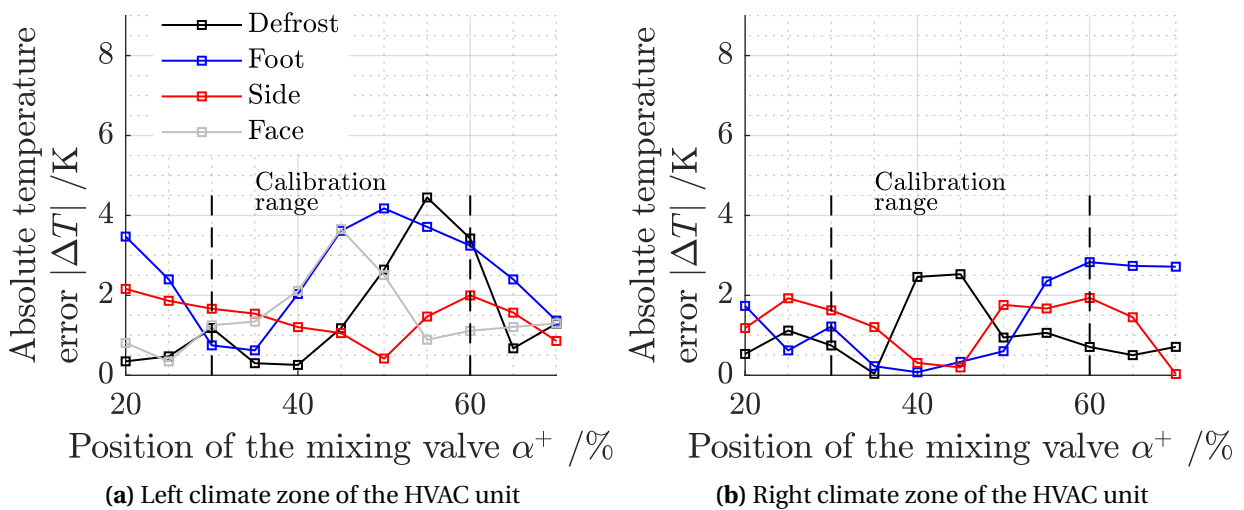
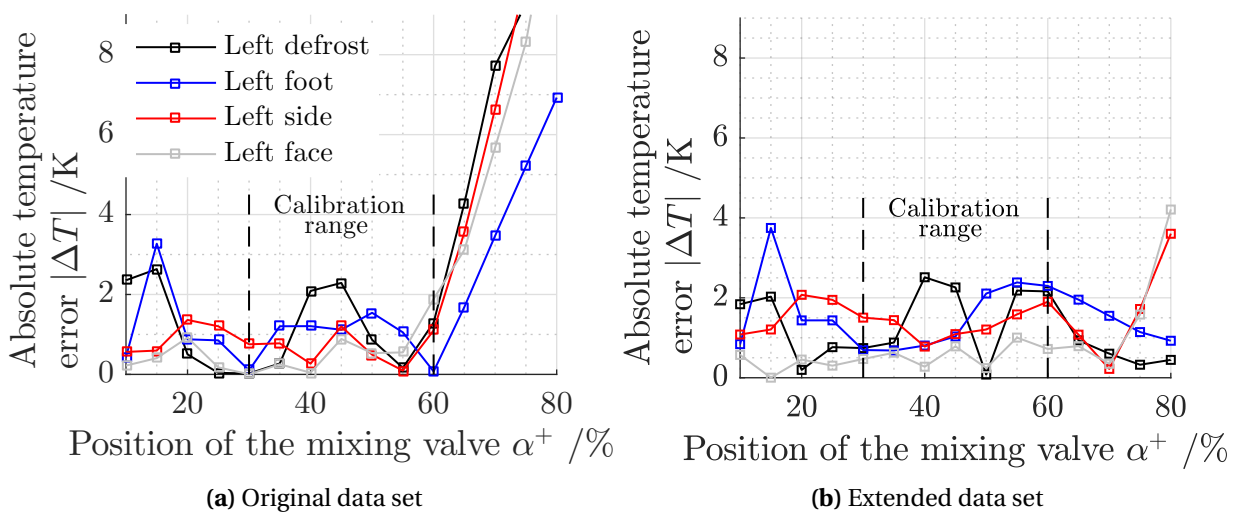


Figure 4.31: Temperature error for test case 2 using the extended data set

Table 4.6: Error evaluation of the outlet temperatures modeled

Outlet	Test case 1		Test case 2	
	Mean error $\mu_{ T }$ /K	Max. error $ \Delta T $ /K	Mean error $\mu_{ T }$ /K	Max. error $ \Delta T $ /K
Left defrost	1.2	2.5	1.5	4.4
Left foot	1.5	3.7	2.5	4.2
Left side	1.5	3.6	1.4	2.1
Left face	0.8	4.2	1.5	3.7
Right defrost	2	3.6	1	2.5
Right foot	1.4	6	1.4	2.8
Right side	1	4.3	1.2	1.9
Right face	1.5	3.6	Closed	Closed

In these figures, the extended data set has been used for the O-POD model. Although the O-POD model performs worse at low mixing valve positions outside the calibration range, this has not a significant impact on the accuracy of the outlet temperatures. The error remains low ($< 3\text{K}$) at almost all outlets. Only at the foot outlet, higher error margins can be observed. A summary of the mean temperature error and maximum temperature error is given in Tab. 4.6.

**Figure 4.32:** Comparison of the absolute temperature error for test case 1 using the extended and the original data set

From this table it can be seen that the mean error is very low and below 1.5 K for almost all test configurations. In general, the maximum error is smaller than 4.4 K.

In Fig.4.32 the predicted outlet temperatures are compared for the HVAC model with the original and extended data set with each other. Using the POD modes generated from the extended experimental data set leads to higher accuracy over a wide operating range. Hence, extending the observations based on physical assumptions can be seen as reliable strategy to enhance the robustness of the HVAC model.

As a major outcome of this chapter, it is shown that the HVAC model provides the temperatures and volume flow rates at the outlets with high accuracy. The following conclusions can be made from the model assessment:

- The error of the flow rates at the outlets predicted by the FR network is less than the measurement uncertainty (0.015) of the test rig data. The accumulated absolute error is smaller than 0.06 for both operating scenarios.
- The mixing process can be analyzed by inspection of the POD modes. The enthalpy flow rates depend linearly on the flow through the HX. This linear dependency is described by the first mode. An increased volume flow rate through the HX leads to a change of the enthalpy flow rate distribution from the defrost and foot outlets to the side and face outlets.
- The enthalpy flow rates at the outlets change non-linearly with the flow distribution at the outlets due to different outlet temperatures. This is described by three modes (2 - 4). The second mode reflects the most important effect, which is a change from the face outlet to the other outlets. Hence, the POD procedure is capable to identify linear and non-linear mechanisms between the flow rate distribution and the enthalpy flow rates at the outlets.

- The O-POD model generated with the extended data set remains accurate over a larger operating range than the model from original data set. The extended data set includes an additional observation to capture asymptotic behavior. Especially at high flow rates through the HX outside of calibration range, the O-POD model remains quite accurate. Extending the data set can be seen as an appropriate measure to increase the robustness of the O-POD model.
- The mean temperature error of the complete HVAC model is almost equal to the measurement uncertainty of the thermocouples (1.5 K). The maximum absolute error is below 4 K for almost all experiments. Both, maximum and mean error are considered to be sufficiently small for an application of the model to climate control.

5 Application of the HVAC Model

The application to a real driving cycle and the accuracy of the derived HVAC model are demonstrated in the first part of this chapter. Then in section 2, a model-based control scheme is discussed and evaluated for both the test rig and the real car.

5.1 Vehicle Application

The HVAC model was applied to a real vehicle since the ultimate goal is to predict the outlet temperatures during driving. A challenging driving cycle was selected to test the performance of the model. This driving cycle is described in the first subsection before the accuracy of the predicted outlet temperatures is evaluated.

5.1.1 Driving Cycle

The HVAC unit was controlled by the ACC using standard settings and sensors during the driving cycle. All temperatures, valve positions, coolant flow rates etc. were recorded using the additional measurement hardware. The experimental driving data was then provided to the HVAC model as input. In comparison to the test rig, the HVAC model was extended by a nodal network of the discretized dashboard to account for the transient behavior of the vehicle structure. This nodal network was applied at the left and right side outlets (see subsection 4.2.1). Afterwards, the calculated outlet temperatures were compared with the measured values.

In reality, the temperature changes of the vehicle structure are highly transient. A typical operating scenario of the car, representing this transient behavior, is the heat up of the vehicle cabin. Therefore, the driving cycle included a heat up scenario as well as urban and highway driving. The heat up scenario was particularly interesting because unsteady thermal boundary conditions have not been considered in the model validation with the test rig. The influence of time varying input parameters on the prediction capability was analysed. Due to the heat up of the vehicle cabin, different operating conditions were prescribed by the ACC. This resulted in large variations of the valve positions and operating conditions for the heating loop and refrigerant cycle.

Ambient and Vehicle Condition

In Fig. 5.1 the cabin temperature is shown over driving time. The cabin temperature is measured by a standard sensor and is used for climate control by the ACC. This temperature reaches 20 °C at the end of the driving cycle. The cabin temperature is almost equal to the ambient temperature at the beginning of the driving cycle, which is approximately 0 °C. Since the thermal radiation \dot{q} was low $< 50 \text{ W m}^{-2}$, the initial temperature of the vehicle structure used for the heat transfer model of the dashboard is considered to be $T_{\text{Amb}}(t = 0)$.

The vehicle velocity U over cycle time is shown in Fig. 5.2. The first 30 min correspond to the urban cycle and the following 30 min to highway driving. The

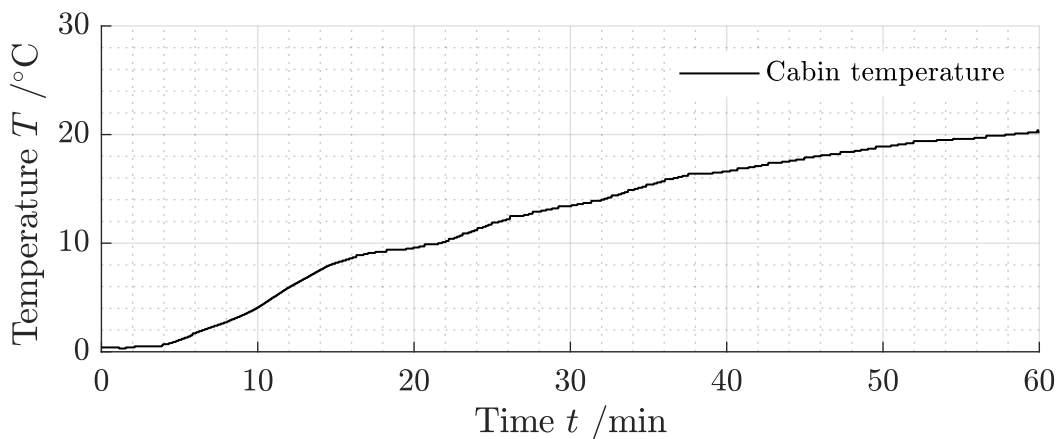


Figure 5.1: Ambient temperature and cabin temperature during the driving cycle

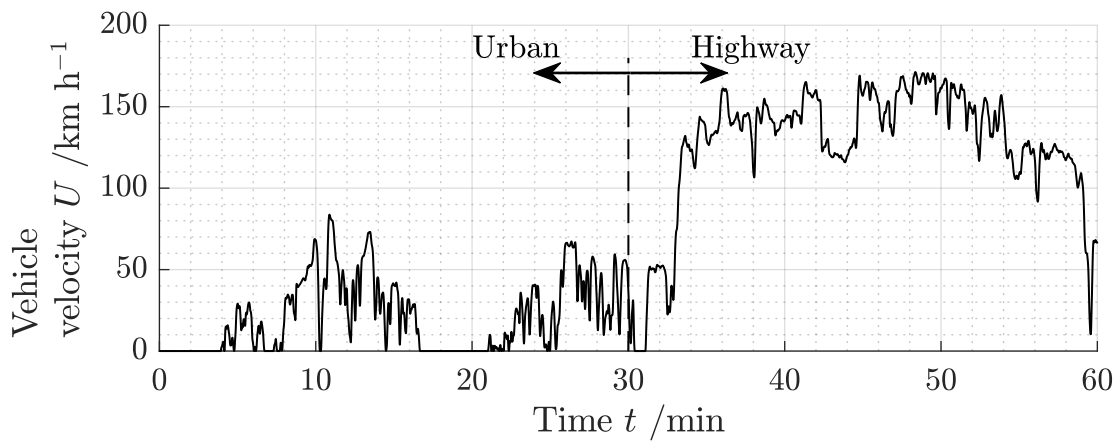


Figure 5.2: Driving velocity during the driving cycle

urban driving cycle is characterized by moderate velocities (50 km h^{-1}) and time intervals where the vehicle comes to halt. The highway cycle includes high velocities ($>100 \text{ km h}^{-1}$) and no halt.

Operating Conditions of the HVAC Unit

The vehicle velocity leads to different operating conditions of the vehicles engine and of the flow conditions at the exterior of the vehicle. This has only minor influence on the total coolant mass flow rate to the heat exchanger or the air mass flow rate moved by the blower while the ACC is active. The coolant mass flow rate remains almost constant at 8 L min^{-1} and the total air mass flow rate seen in Fig. 5.3 shows only small fluctuations of the supplied air flow.

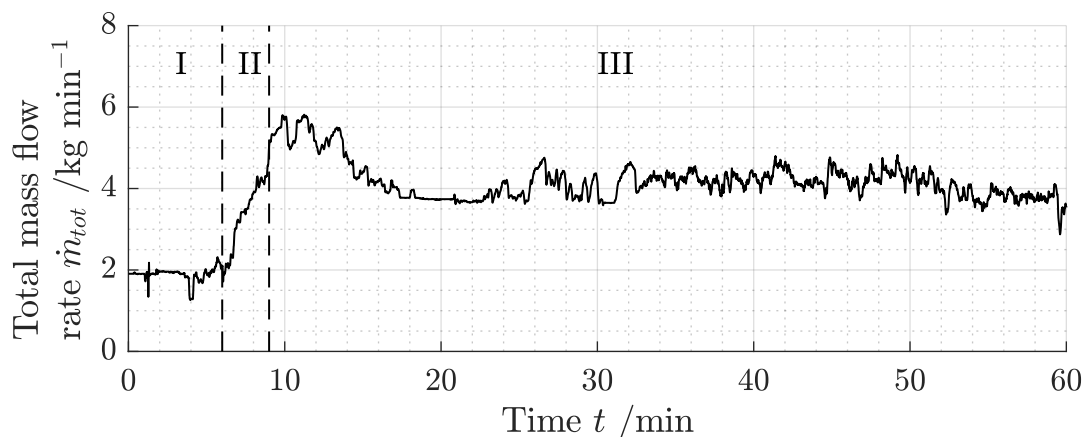


Figure 5.3: Total air mass flow rate during the driving cycle

This is because the ACC aims to maintain a constant mass flow rate by regulating the blower's speed. The total air mass flow rate is low (2 kg min^{-1}) during the first 6 minutes. Then from 6 to 10 minutes, the mass flow is ramped up to 5 kg min^{-1} and reduces afterwards to 4 kg min^{-1} . The total mass flow rate remains at this value for the rest of the driving cycle. In Fig. 5.3 three time intervals are highlighted. These time intervals refer to three significantly different operating conditions of the air distribution valves.

These operating conditions are as follows

- I: Ventilation mode (0 minutes to 6 minutes),
- II: Defog mode (6 minutes to 9 minutes),
- III: Heater mode (9 minutes to 60 minutes).

The valve positions for these operating conditions and the resulting dimensionless mass flow rates are shown in Fig. 5.4 for the left zone, which is the same as the right zone in this test. During the ventilation mode (I), the total mass flow rate is approximately 2 kg min^{-1} . This operating condition might be seen as an idle mode for the first few minutes while the coolant temperatures are still low. The valves change to the defog mode (II) with increasing coolant temperature. In the defog mode most of the air flow is blown through the defrost outlet into the cabin to avoid fogging on the windshield. The dimensionless mass flow rates at the other outlets are low. Then the HVAC unit switches to the heater mode (III). In the heater mode the defrost, foot and side outlet are all opened. This indicates that air flow through the defrost outlet is still required to maintain good view through the windshield without fogging. As the air stream from the face outlet usually passes the passengers closely, the high outlet temperatures during the cabin heat up might lead to thermal discomfort. So, the face outlets are closed.

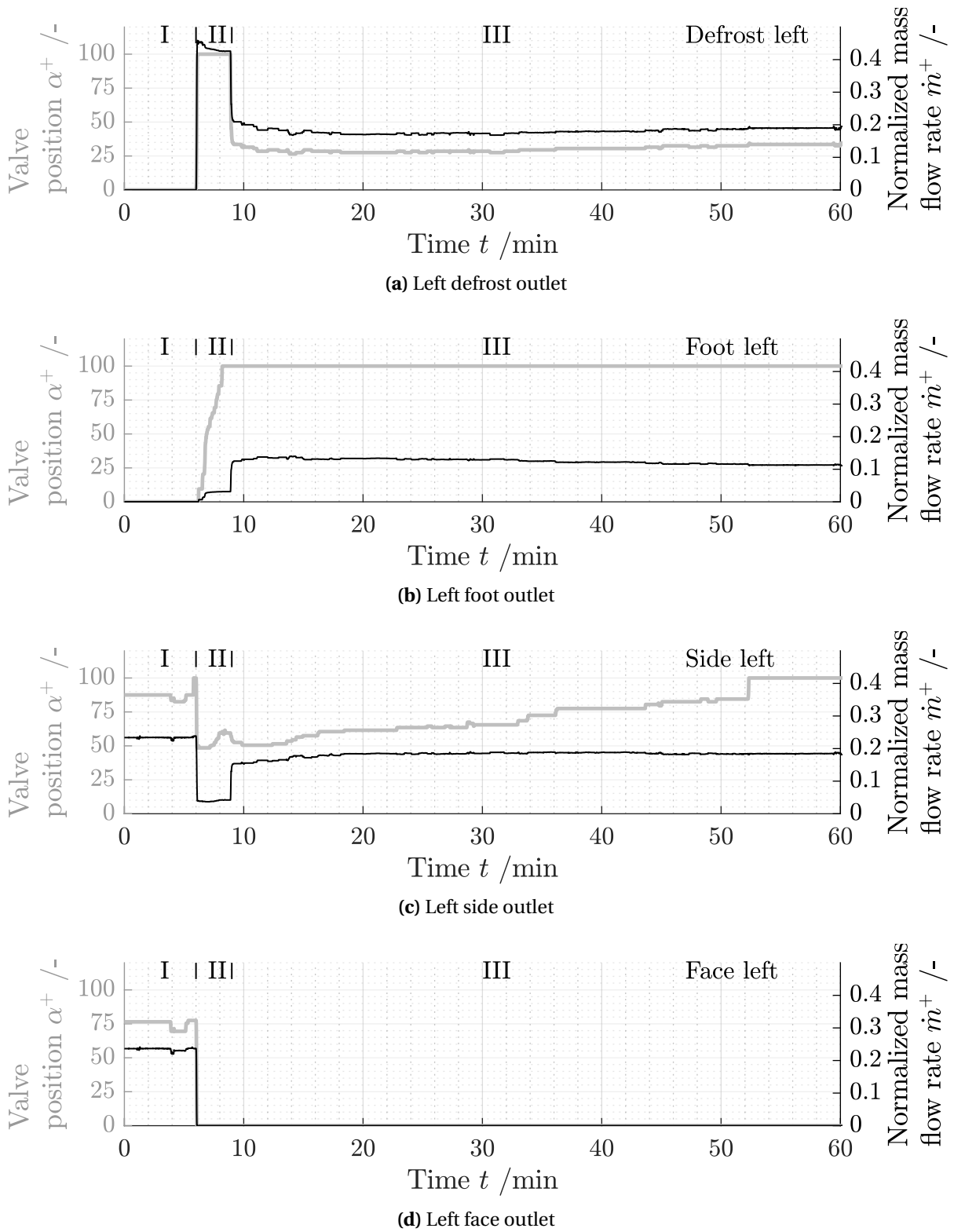
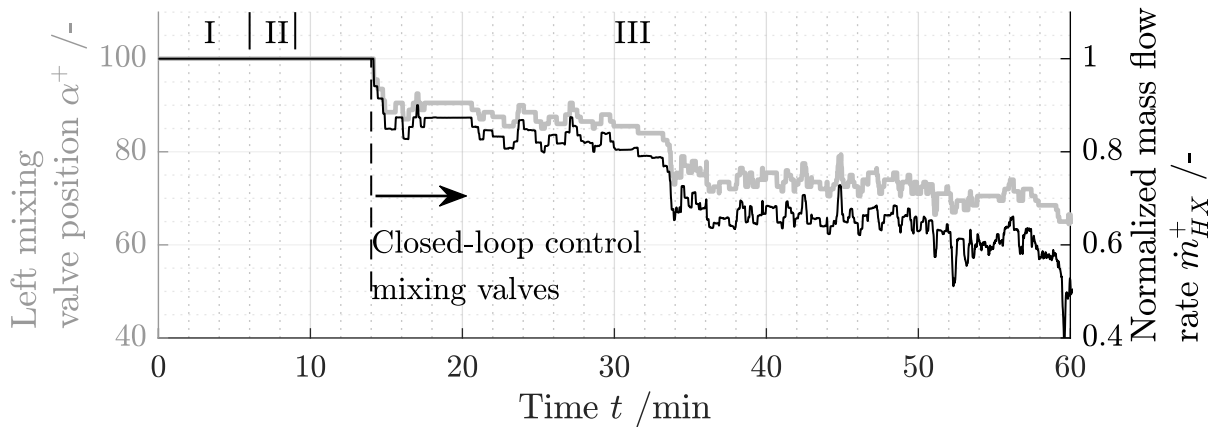
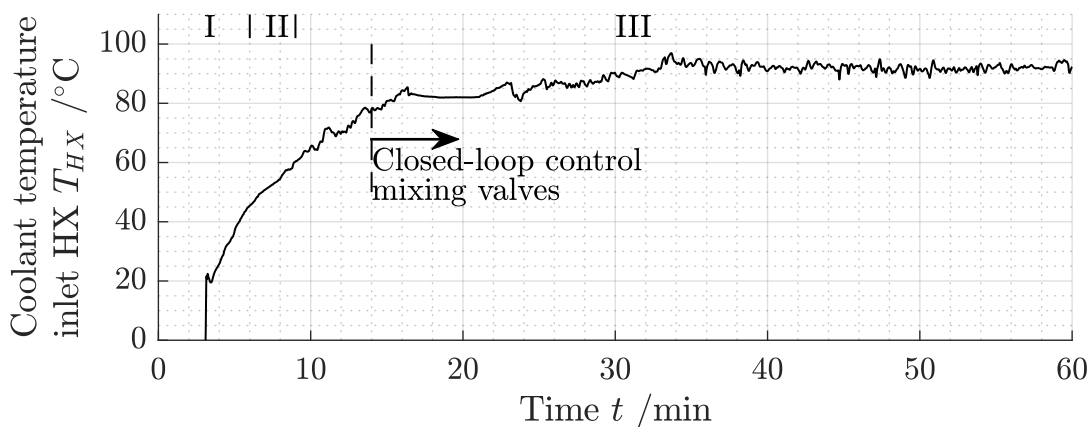


Figure 5.4: Valve positions and mass flow rates in the left climate zone

The high outlet temperatures result from the position of the mixing valves, which are illustrated in Fig. 5.5a. No temperature regulation is required for the first 14 minutes of the cycle due to low coolant temperature at the inlet of the HX. The inlet temperature of the HX is shown in Fig. 5.5b. Once the engine coolant temperature is higher than the desired outlet temperatures, the mixing valve is used to control the outlet temperatures as highlighted in Fig. 5.5. As a consequence, the bypass of the HX is closed for the first 14 minutes and the dimensionless mass flow rate through the HX results in 1.



(a) Position of the mixing valve and air mass flow rate through the HX



(b) Coolant inlet temperature of the HX

Figure 5.5: Position of the mixing valve of the HVAC unit and the coolant inlet temperature of the HX

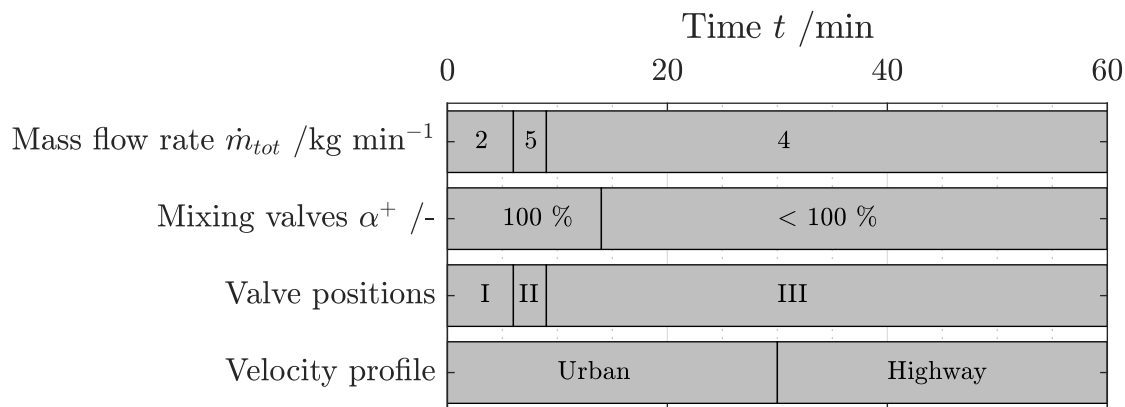
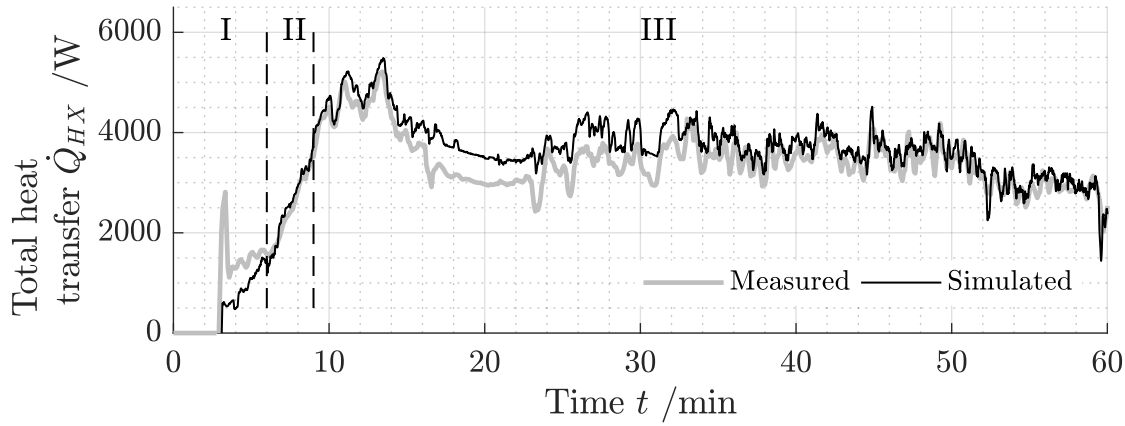


Figure 5.6: Summary of the different operating conditions during the driving cycle

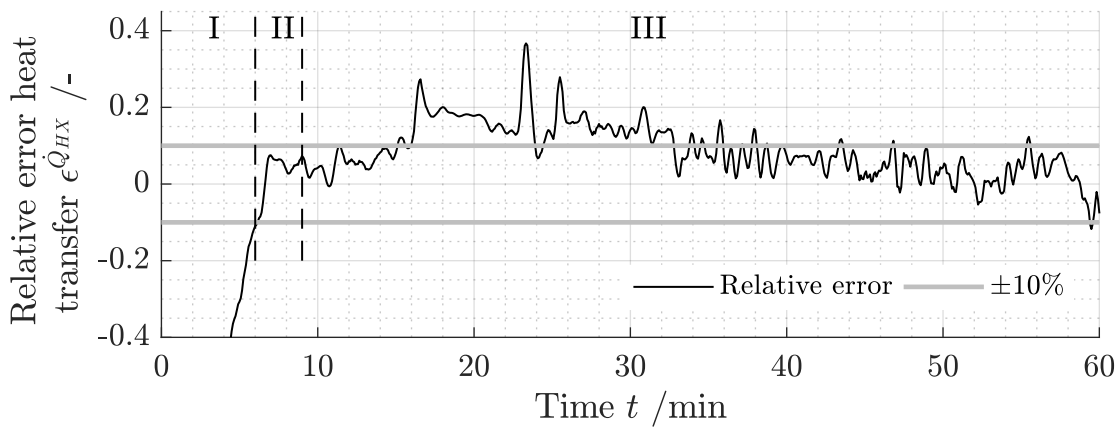
After 90 °C has been reached the temperature remains constant for the rest of the driving cycle (33 min to end). The air temperature at the outlet of the evaporator is approximately 1 °C and slightly higher than the ambient temperature because of heat transfer upstream of the evaporator. Temperature differences at the outlet of the evaporator are small (<1 K) and the outlet temperature is considered to be homogeneous. A summary of the different operating conditions are given in Fig. 5.6.

5.1.2 Results and Accuracy of the HVAC Model

The measured and simulated total heat transfer of the HX are compared with each other in Fig. 5.7. The experimental value is derived from an energy balance applied to the coolant of the HX. The simulated value is the heat transfer to the air in the HX. During the highly transient heating period from 3 to 6 minutes, large deviations can be observed between the simulated and measured heat transfer. In this time period the relative error is larger than 40% of the measured value as shown in Fig. 5.7b. The error becomes low (<10%) after this highly transient time interval (3 to 6 minutes) until the mixing valves are regulated at 14 minutes. Major deviations (700 W) are observed between 14 minutes to 33 minutes. The HVAC model overpredicts the heat transfer as seen before in Fig. 4.28. This time interval refers to the urban driving cycle.



(a) Total heat transfer HX



(b) Relative error total heat transfer HX

Figure 5.7: Comparison of the measured and simulated total heat transfer of the HX

The total heat transfer is predicted with high accuracy ($<10\%$) for the rest of the driving cycle (33 minutes to end). The overpredicted heat transfer from 14 minutes to 33 minutes shows that the efficiency of the HX η_{HX} used to predict the heat transfer is wrong. The efficiency η_{HX} used in the model was determined for almost homogeneous air flow conditions at the inlet of the HX. But in the HVAC unit, the mixing valves upstream of the HX lead to inhomogeneous flow conditions at the HX inlet. This indicates a drop of efficiency η_{HX} at valve positions $<100\%$.

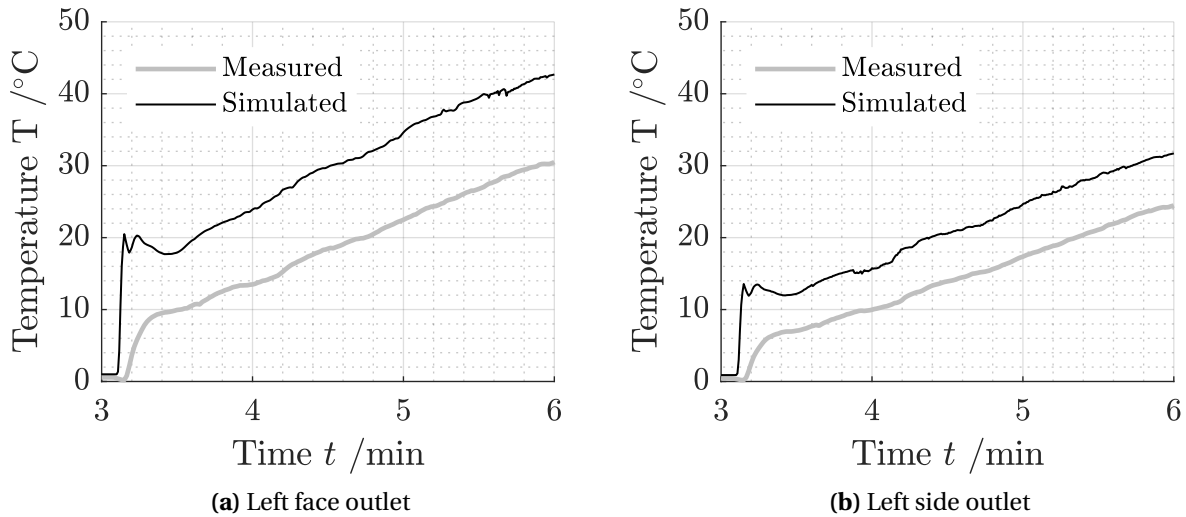
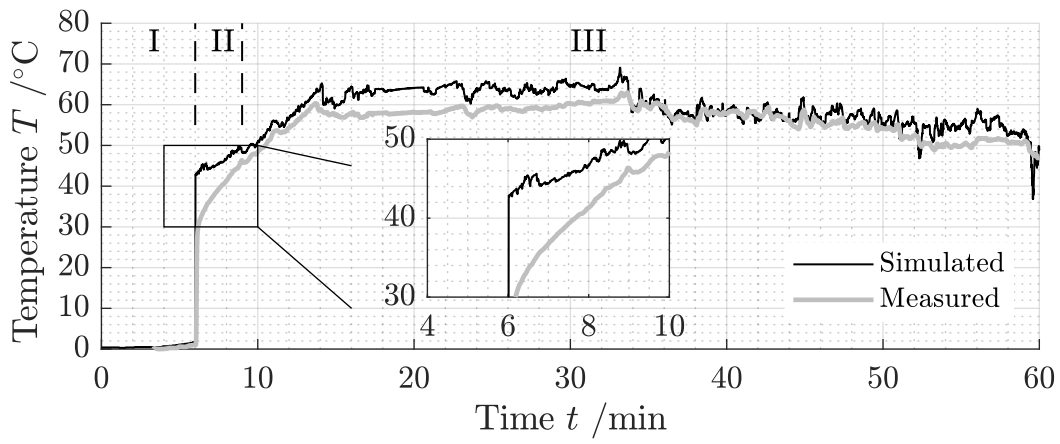
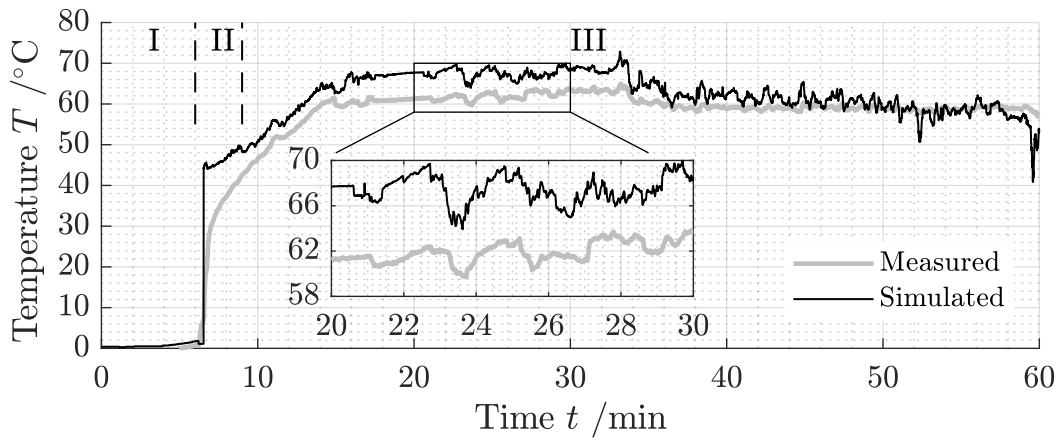


Figure 5.8: Face and side outlet temperatures during the driving cycle in the left climate zone of the HVAC unit

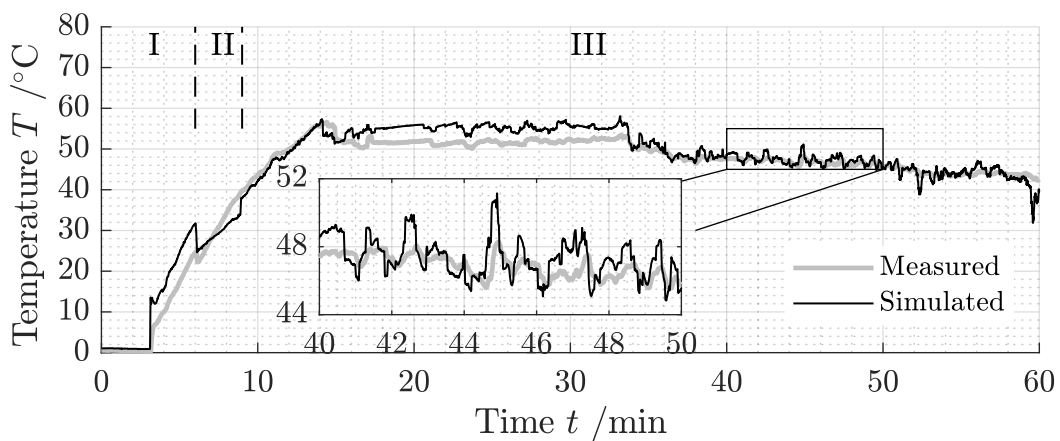
The highly transient behavior in the beginning of the driving cycle (3 to 6 minutes) reflects a particular weakness of the current HVAC model structure. It results from the missing description of heat transfer upstream of the outlet ducts. The quasi-steady energy balance of the HX and the steady POD model of the mixing chamber result in higher enthalpy flow rates at the outlets of the HVAC unit. In turn, the outlet temperatures are overpredicted. This is shown in Fig. 5.8 from 3 to 6 minutes for the side and face outlets. The measured value corresponds to the mean average of the five thermocouples. This period refers to the ventilation mode (I) and only the face and side outlet are opened. The simulated face outlet temperature is the air temperature at the outlet of the HX because no heat transfer is considered for this flow path and the bypass is closed. Although a nodal network models the heat conduction in the side duct, an absolute temperature error up to 6 K remains. This shows that the heat capacity of the HX and the heat conduction in the mixing chamber have a significant influence during highly transient heating or cooling.



(a) Left defrost outlet



(b) Left foot outlet



(c) Left side outlet

Figure 5.9: Outlet temperatures during the driving cycle in the left climate zone of the HVAC unit

The outlet temperatures of the other outlets are presented in Fig. 5.9. The face outlet is not shown because it is only opened for the first 6 minutes. The highly transient behavior at the beginning of the driving cycle leads again to increased errors. In the defog mode (II), the defrost valve and the foot valve open. Approximately 3 minutes are required until the approximate steady state temperatures at these outlets are reached as depicted in Fig. 5.9a. The transient temperature difference of the defrost and foot outlets show the typical temperature response of transient conduction, which has the form

$$\frac{T - T_{\infty}}{T_0 - T_{\infty}} = \exp\left(-\frac{t}{\tau}\right). \quad (5.1)$$

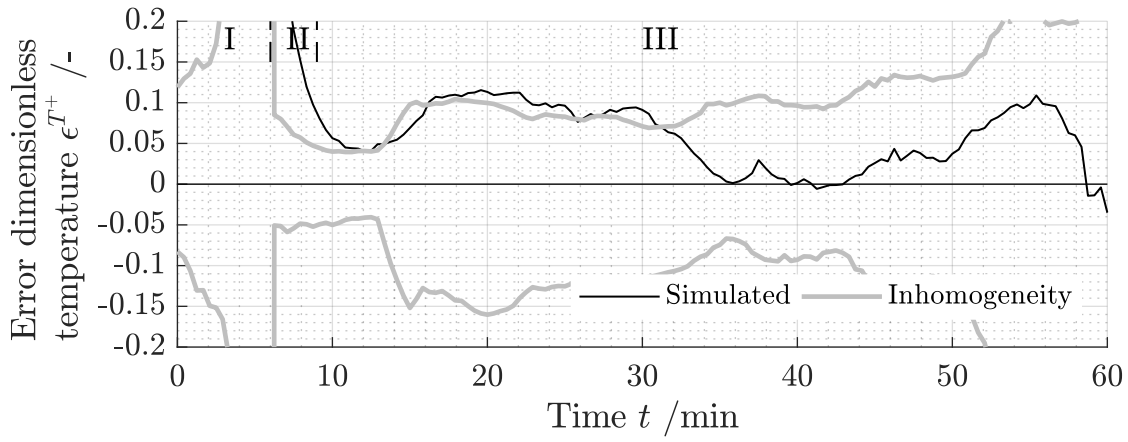
In Eq.5.1, τ is the thermal time constant. Only minor deviations (<3 K) are observed once steady state is reached. The small error between measured and simulated outlet temperatures corresponds with the small error of the total heat transfer in the HX for this time period. Similarly, the temperature error increases from 14 to 33 minutes where larger errors of the calculated heat transfer can be seen. The HVAC model overestimates the temperature at all outlets for this time interval. The temperature differences (<5 K) are highlighted in Fig. 5.9b and can be traced back to the error of the predicted heat transfer in the HX. In the time period of highway driving (33-60 minutes), the HVAC model predicts the outlet temperatures at high accuracy. The model performance is almost equal to the error of the standard sensor used by the ACC (<1.5 K).

To evaluate the absolute temperature deviations, the relative temperature error is computed as

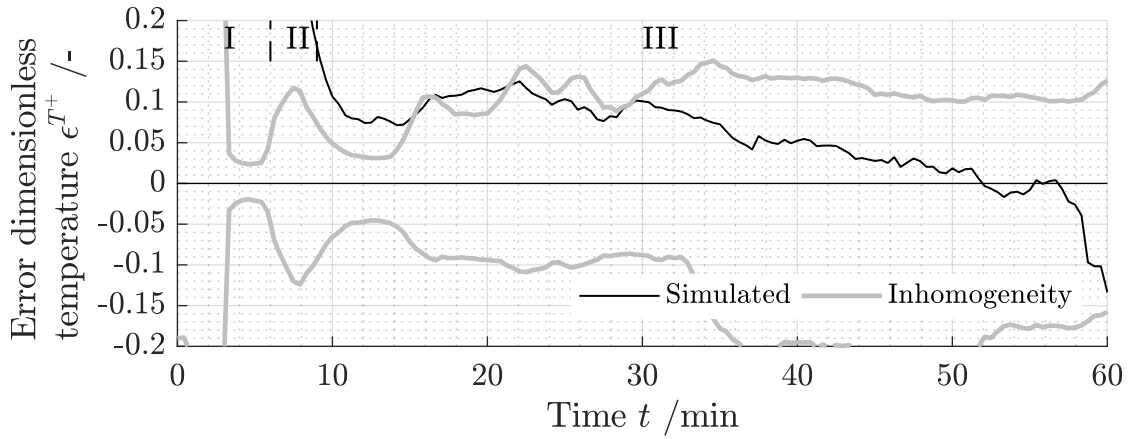
$$\epsilon^{T^+} = \frac{T_{Sim} - \bar{T}_{Exp}}{\bar{T}_{Exp} - T_{Evap}}, \quad (5.2)$$

where \bar{T}_{Exp} refers to the mean averaged value of the five thermocouples and T_{Sim} is the simulated value. Furthermore, the maximum and minimum temperature inhomogeneity IH is calculated from the measured data as

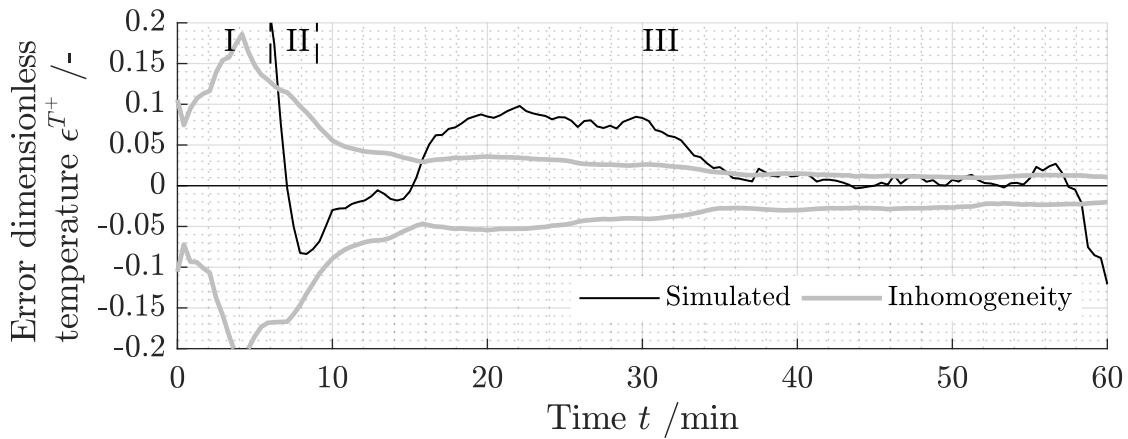
$$IH = \frac{\max / \min (\mathbf{T}_{Exp} - \bar{T}_{Exp})}{\bar{T}_{Exp} - T_{Evap}}. \quad (5.3)$$



(a) Left defrost outlet



(b) Left foot outlet



(c) Left side outlet

Figure 5.10: Relative temperature error during driving cycle in the left climate zone of the HVAC unit

It serves to show the difficulty to determine the caloric mean temperature using only one standard temperature sensor. It can be seen in Fig. 5.10 that the relative temperature error is less than 0.1 for almost the complete driving cycle. The error exceeds 0.1 only during the highly transient time interval from 0 to 10 minutes. The measured inhomogeneity indicates huge temperature differences in the air flow at the defrost and foot outlets. This demonstrates the difficulty to provide accurate feedback to the ACC with the standard sensor. The air flow is homogeneous at the side outlet compared with the other outlets. The length and topology of this ventilation duct leads to a better homogenization of the air flow. A model error ϵ^{T^+} of less than 0.1 is considered to be sufficiently low.

In summary, the results show that the HVAC model applied to real driving data of the test vehicle delivers reliable results and high accuracy for the outlet temperatures. Based on the comparison of measured and simulated data, the following conclusions can be made:

- In steady state, the heat transfer is predicted with satisfying accuracy. This indicates also that the total air mass flow rate \dot{m}_{tot} is computed with minor deviations since this value is an input signal for the HX model. Inhomogeneous air flow at the inlet of the HX may lead to deviations between model and measurements. An improved HX efficiency model would be required to increase accuracy
- The absolute maximum error of the outlet temperatures is less than 5 K for almost the complete driving cycle. Higher deviations result from the transient behavior of the mixing chamber and the HX during the first minutes of the driving cycle. It was shown that the accuracy of the outlet temperatures is directly related to the calculated heat transfer in the HX. Further effort might be spend in modeling the HX and heat conduction to increase the prediction performance. However, the error between measured and simulated outlet temperatures is less than 10% of the total temperature increase at the corresponding outlet of the HVAC unit when quasi steady state is reached.

- The HVAC model was calibrated using an experimental data set from the test rig. Only minor parameters variations were sufficient for a transfer of the model to the vehicle according to the model approach in section 4.2.1. The results show high prediction accuracy. This demonstrates the applicability to vehicles, which have a HVAC unit identical to the test rig.

5.2 Model-based Control

The derived HVAC model is used for climate control in this section to eliminate the need for temperature sensors while saving money and increasing comfort. Therefore, a model-based open loop control approach is presented as an alternative to the standard feedback control. First, the application to the test rig is demonstrated. The approach is then extended to the real vehicle.

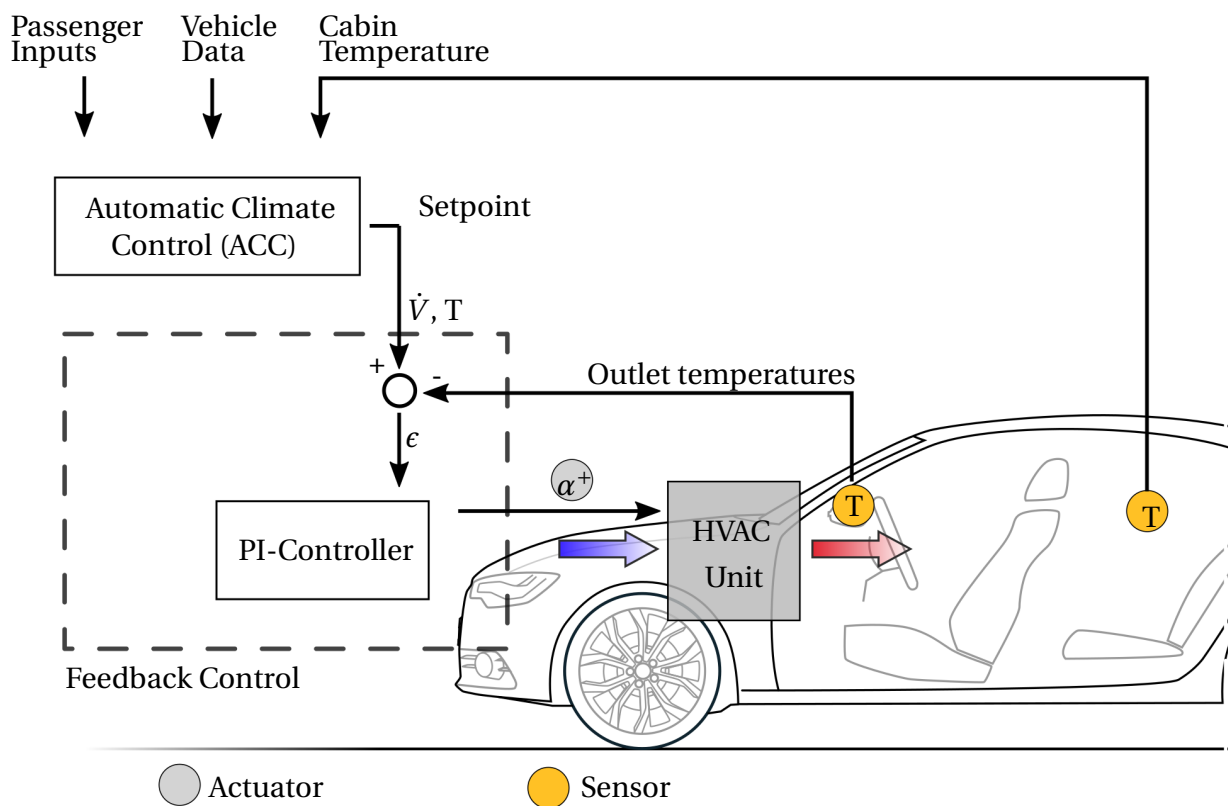


Figure 5.11: Standard feedback control of the HVAC unit [95]

The aim of the Automatic Climate Control (ACC) is to provide pleasant thermal conditions for the passengers of the car. The ACC receives the measured cabin temperature, inputs from the passenger and additional driving data as shown in Fig. 5.11. Based on these inputs, desired outlet temperatures and volume flow rates are determined by the ACC to obtain thermal comfort. These outlet values are the setpoint (SP) for the standard feedback control procedure of the HVAC unit. The valve positions are regulated based on temperature measurements in the outlet ducts to meet the specified outlet temperatures. Typically, Proportional-Integral (PI) controllers are applied in the feedback loop.

To avoid the costly temperature sensors in the outlet ducts an open-loop model-based control procedure is proposed as illustrated in Fig. 5.12. The input for the proposed control scheme is the setpoint for the outlet tempera-

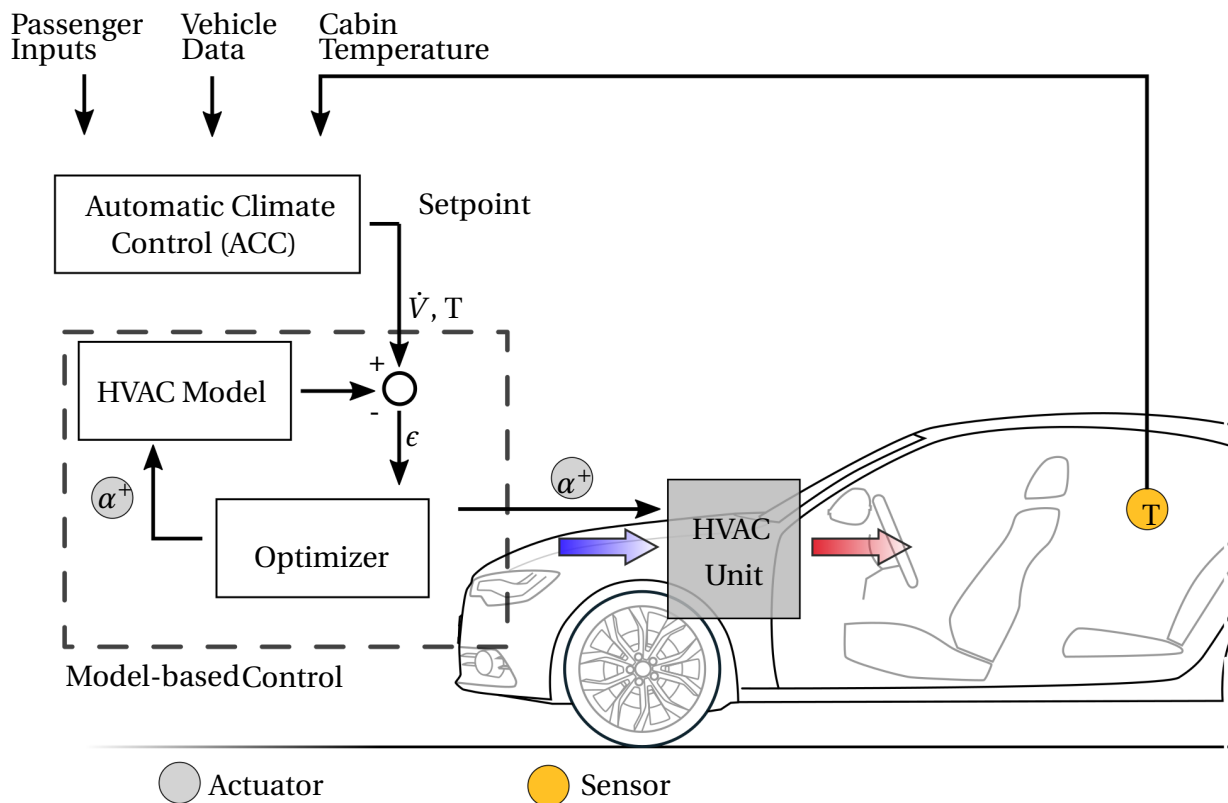


Figure 5.12: Model-based control approach of the HVAC unit

tures and volume flow rates. Subsequently, the difference between these setpoints and the modeled values are computed. Based on the difference, an optimizer changes the valve positions used as input for the HVAC model until the error is sufficiently low. The optimizer calculates the error by

$$\min_{\alpha^+ \in [0,100]} \left([(\dot{\mathbf{V}}_{SP}^+ - \dot{\mathbf{V}}_{Sim}^+) W]^2 + [\mathbf{T}_{SP} - \mathbf{T}_{Sim}]^2 \right), \quad (5.4)$$

where the subscripts SP and Sim denote the prescribed setpoint and simulated value, respectively. Eq. 5.4 is solved in a least square sense. The weighting factor W can be modified to increase or decrease the influence of the volume flow rates on the optimization procedure.

5.2.1 Test Rig

The model-based control of the test rig is demonstrated in the following. Three operating conditions were selected. The prescribed values are shown in Tab. 5.1 and Tab. 5.2 for the dimensionless mass flow rates and temperatures at the outlets, respectively.

Table 5.1: Selected setpoints for the volume flow rates $\dot{\mathbf{V}}_{SP}^+$

Outlet	Case 3 / -	Case 4 / -	Case 5 / -
Left/Right defrost	0.2 / 0.2	0.1 / 0.1	0 / 0
Left/Right foot	0.175 / 0.175	0 / 0	0 / 0
Left/Right side	0.125 / 0.125	0.175 / 0.175	0.25 / 0.25
Left/Right face	0 / 0	0.225 / 0.225	0.25 / 0.25

Table 5.2: Selected setpoints for the outlet temperatures \mathbf{T}_{SP}

Outlet	Case 3 /°C	Case 4 /°C	Case 5 /°C
Left/Right defrost	39 / 39	24 / 24	Valve closed
Left/Right foot	41 / 41	Valve closed	Valve closed
Left/Right side	38 / 38	13 / 13	44 / 44
Left/Right face	Valve closed	15 / 15	40 / 40

Table 5.3: Estimated valve positions α^+ for the specified operating conditions

Valve / %	Case 3	Case 4	Case 5
Left/Right defrost	41 / 41	21 / 21	0 / 0
Left/Right foot	100 / 100	0 / 0	0 / 0
Left/Right side	51 / 52	77 / 73	100 / 100
Left/Right face	0 / 0	100 / 71	76 / 62
Left/Right mixing valve	61 / 62	20 / 24	64 / 66

These operating conditions correspond to a typical application in the vehicle. For example, case 3 is a heating scenario. The face outlet is closed since the hot air flow from the outlet may lead to local discomfort in the head region of the passenger. Furthermore, deviations of the selected temperatures between the cases are large (> 20 K) to ensure that the model-based approach provides good results over a wide operating range. The total mass flow rate \dot{m}_{tot} was set to 4 kg min^{-1} . The parameters of the refrigerant and heating loop were identical to those from the test cases in Tab. 4.5 in subsection 4.2.2. The coefficient W was 100 as this value leads to good results as shown at the end of this section. The computed valve positions by the model-based approach are summarized in Tab. 5.3. Measurements with the test rig were conducted using these valve positions.

The experimental results for the left climate zone are compared in the following with the specified setpoints and simulated values in Fig. 5.13 and Fig. 5.14. The operating condition from 0 to 20 minutes refers to case 3. In the following 20 minutes, case 4 was measured and the last 20 minutes correspond to operating case 5.

Volume Flow Rates

Only minor deviations can be observed for the dimensionless volume flow rates between the setpoints, experimental value and predicted quantity from the HVAC model. The maximum difference to the measured mass flow rates of both SP and simulation is less than 0.015. This is considered to be accurate regarding a measurement accuracy of 0.015.

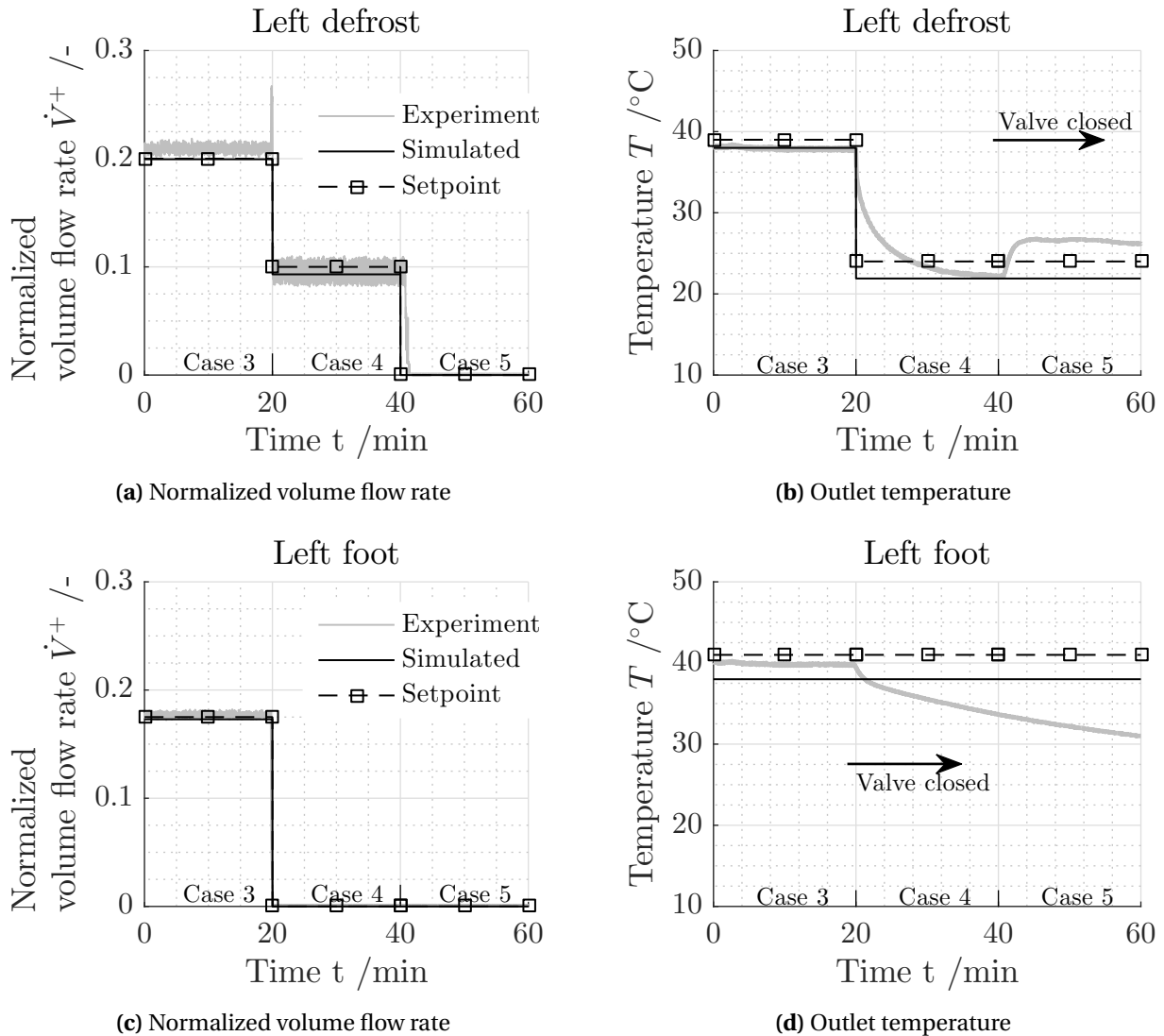


Figure 5.13: Comparison of the simulated and measured values with the setpoints for the left defrost and foot outlets

Outlet temperatures

The maximum difference of simulated and measured outlet temperatures is < 2 K. However, larger deviations of the simulated values from the specified temperatures can be seen. The maximum errors are 3 K for case 3 and 4, while deviations up to 5 K can be observed for case 5. These differences can be traced back to the arbitrarily specified setpoints. As the heat transfer is coupled to the mass flow rate, certain combinations of flow distribution and outlet tempera-

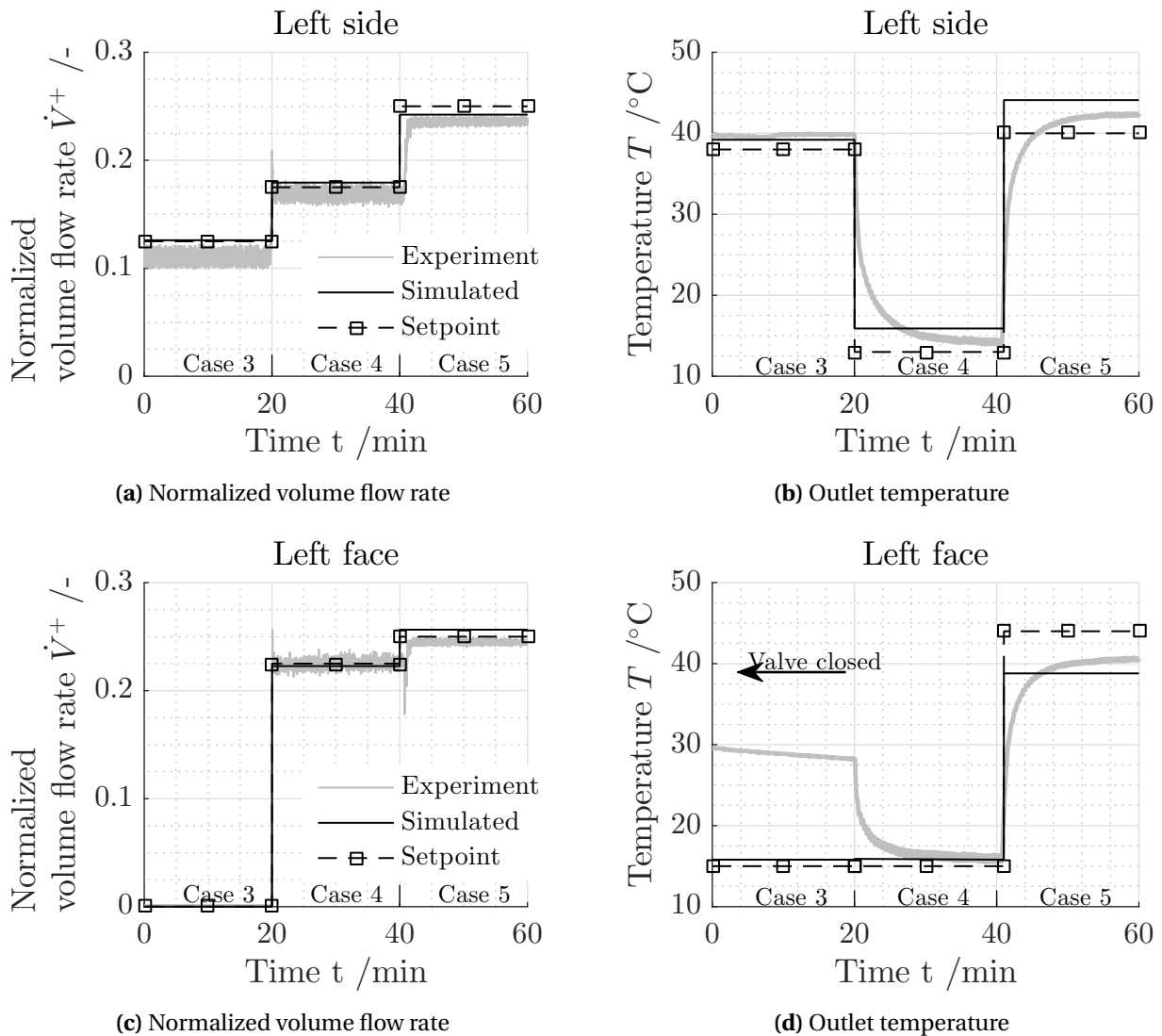


Figure 5.14: Comparison of the simulated and measured mass flow rates and outlet temperatures with the setpoints for the left side and face outlets

tures might not be possible to obtain. The optimizer aims to balance the error between the volume flow rates and temperatures in a least square sense. This also results in deviations from the setpoint for both quantities. Therefore, the outlet values should be chosen in a reasonable range.

Table 5.4: Measured volume flow rates and outlet temperatures at steady state

	Case 3	Case 4	Case 5
Measured volume flow rates \dot{V}_{Exp}			
Left/Right defrost	0.21 / 0.21	0.1 / 0.09	0 / 0
Left/Right foot	0.18 / 0.18	0 / 0	0 / 0
Left/Right side	0.11 / 0.11	0.17 / 0.17	0.24 / 0.25
Left/Right face	0 / 0	0.23 / 0.24	0.24 / 0.27
Measured outlet temperatures T_{Exp}			
Left/Right defrost	37.8 / 38.6	22.3 / 22.4	Valve closed
Left/Right foot	39.8 / 42.9	Valve closed	Valve closed
Left/Right side	39.8 / 36.8	14.2 / 15	42.2 / 39.3
Left/Right face	Valve Closed	15.9 / 16.3	40.5 / 46.1

The influence of the model accuracy and weighting factor W on the predicted valve positions was assessed. For this purpose, the measured values for the volume flow rates and temperatures from Tab. 5.4 were prescribed as setpoints

$$\dot{V}_{Exp}^+ = \dot{V}_{SP}^+ \text{ and } T_{Exp} = T_{SP}. \quad (5.5)$$

The difference between the real and estimated valve positions from Tab. 5.3 can be subjected to the model accuracy. Furthermore, the procedure was performed for weighting coefficients W of 10, 100, and 1000. The predicted positions are summarized in Tab. 5.5 for these three weighting coefficients. Factors of $W = 10$ and 1000 lead to major deviations between the actual and predicted operating condition. Especially in case 4, the model-based control approach is not capable to provide good values. In contrast, a weighting factor of $W = 100$ is a good compromise and accurate valve positions are estimated. The difference of the predicted and real valve angles using $W=100$ leads to a temperature deviation of 1 K for the investigated operating conditions.

The major outcome from these results can be summarized as follows:

- The deviations between the simulated and the experimental values are similar to the errors observed before in subsection 4.2.2. The valve positions are optimized in a least square sense for the specified setpoints. Therefore, differences of the simulated outlet quantities and the specified values are inevitable for arbitrarily selected values.

Table 5.5: Estimated valve positions α^+ using the outlet quantities measured as setpoint

	Case 3		Case 4		Case 5	
	Estimated	Reference	Estimated	Reference	Estimated	Reference
W=10						
Left/Right defr	25 / 25	41 / 41	22 / 22	21 / 21	0 / 0	0 / 0
Left/Right foot	6 / 56	100 / 100	0 / 0	0 / 0	0 / 0	0 / 0
Left/Right side	52 / 96	51 / 52	1 / 96	77 / 73	71 / 100	100 / 100
Left/Right face	0 / 0	0 / 0	74 / 100	100 / 71	50 / 24	67 / 72
Left/Right mix	66 / 57	61 / 62	40 / 20	20 / 24	63 / 67	64 / 66
W=100						
Left/Right defr	42 / 42	41 / 41	20 / 20	21 / 21	0 / 0	0 / 0
Left/Right foot	83 / 100	100 / 100	0 / 0	0 / 0	0 / 0	0 / 0
Left/Right side	54 / 48	51 / 52	62 / 60	77 / 73	87 / 100	100 / 100
Left/Right face	0 / 0	0 / 0	88 / 69	100 / 71	66 / 64	67 / 72
Left/Right mix	60 / 62	61 / 62	22 / 27	20 / 24	65 / 66	64 / 66
W=1000						
Left/Right defr	41 / 41	41 / 41	16 / 16	21 / 21	0 / 0	0 / 0
Left/Right foot	97 / 97	100 / 100	0 / 0	0 / 0	0 / 0	0 / 0
Left/Right side	42 / 42	51 / 52	47 / 46	77 / 73	88 / 100	100 / 100
Left/Right face	0 / 0	0 / 0	59 / 56	100 / 71	67 / 66	67 / 72
Left/Right mix	61 / 62	61 / 62	20 / 30	20 / 24	65 / 66	64 / 66

- Three different coefficients W have been applied to change the relative influence of the volume flow rates and the outlet temperatures on the optimization procedure. A coefficient of 100 shows the best results as the valve positions are predicted precisely.

5.2.2 Vehicle

The model-based control procedure was applied to the real vehicle. In the vehicle, the HX was connected to the cooling loop of the vehicle engine. Hence, the coolant volume flow rate and temperature depended on the engines operating condition. Furthermore, only the temperatures were measured in the vehicle, but not the volume flow rates.

Table 5.6: Valve positions applied for model-based control in the vehicle

Valves	Operating condition				
	I	II	III	IV	V
Defrost	0	0	0	0	0
Foot	60	100	100	100	100
Side	100	0	60	0	60
Face	60	100	100	100	100
Mixing valve	50	50	50	50	50
Operation	Stationary			Driving	

Therefore, vehicle measurements were conducted at specified valve positions and with deactivated ACC. The resulting experimental data was used as input for the HVAC model to compute the volume flow rates at the outlets. Subsequently, the simulated volume flow rates and the outlet temperatures measured were selected as setpoints

$$\dot{\mathbf{V}}_{Sim}^+ = \dot{\mathbf{V}}_{SP}^+ \text{ and } \mathbf{T}_{Exp} = \mathbf{T}_{SP}. \quad (5.6)$$

Three different valve positions have been selected during stationary operation of the vehicle and two operating conditions were applied during driving. These valve positions were identical for the left and right climate zone of the vehicle and are realistic for a real driving scenario. They are summarized in Tab.5.6. As a consequence, the volume flow rates at the outlets were almost equal for both climate zones. The dimensionless volume flow rates for the left climate zone are depicted in Fig 5.15b. The blower speed has been set to 2000 RPM during the complete driving cycle. Fluctuations of the total mass flow rate can be observed due to different vehicle velocities as shown in Fig. 5.15a

The outlet temperatures were set to an almost equal value than the cabin temperature and ambient temperature to reduce heat transfer in the ducts and mixing chamber. This resulted in a mixing valve position of 50 %. The air temperature at the outlet of the evaporator was approximately 4 °C and the coolant temperature was 90 °C. The first operating condition was set for 40 minutes to obtain the measured values at quasi-steady state. Afterwards, each operating condition was measured at least for 12 minute since the mixing valve was not varied for temperature regulation.

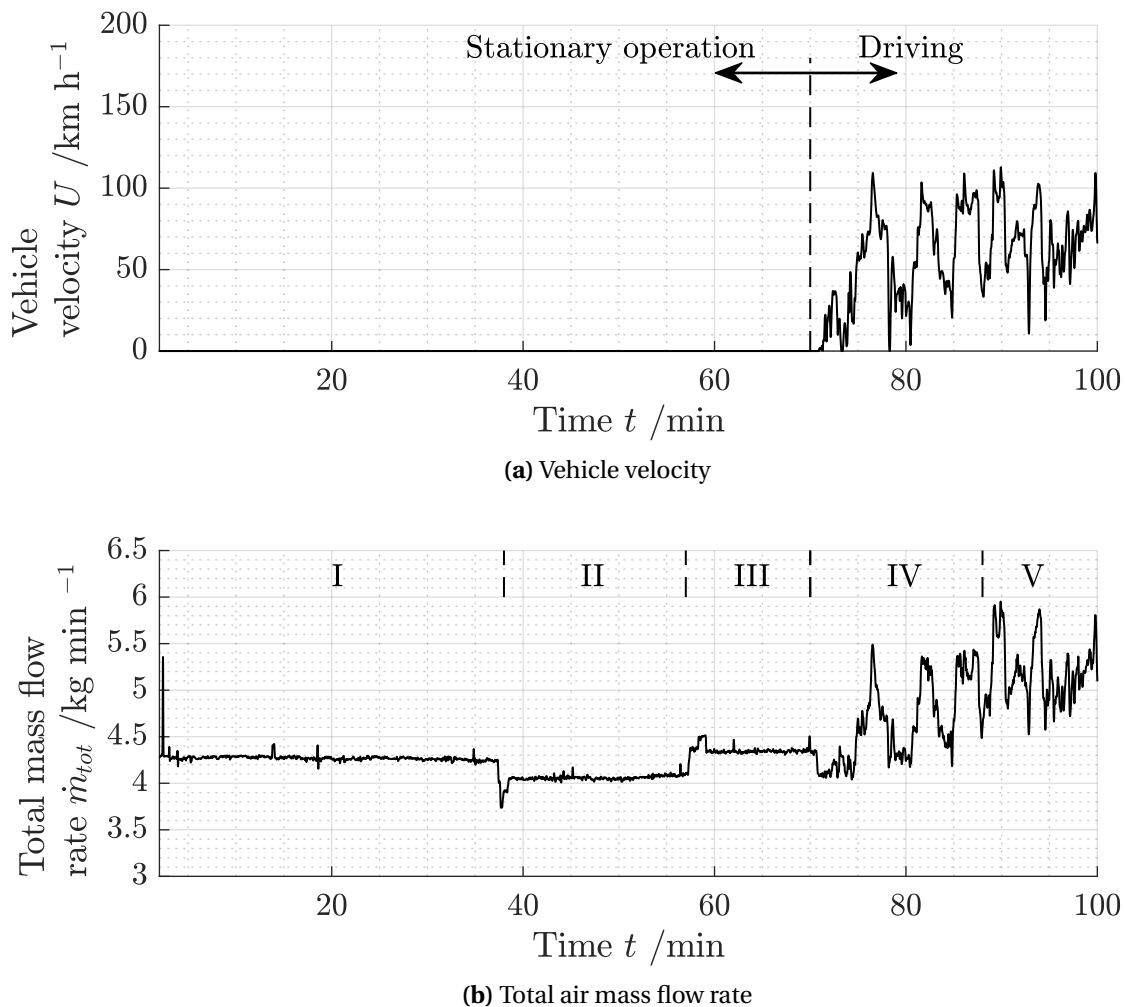


Figure 5.15: Velocity profile and total mass flow rate for model-based control

The estimated and reference mixing valve positions are presented in Fig. 5.16 for the specified operating conditions. Only minor differences from the reference operating conditions can be observed. While the reference position remains constantly at 50 % as prescribed, the estimated values are approximately 52 % during the stationary operation of the car. This corresponds to a difference of 0.02 regarding the dimensionless volume flow rate through the HX. Minor deviations can be seen for the operating condition IV and V, which refer to the transient driving of the vehicle.

The total mass flow rate is influenced by the velocity of the vehicle since the ACC is deactivated and the total mass flow rate was not controlled. This leads

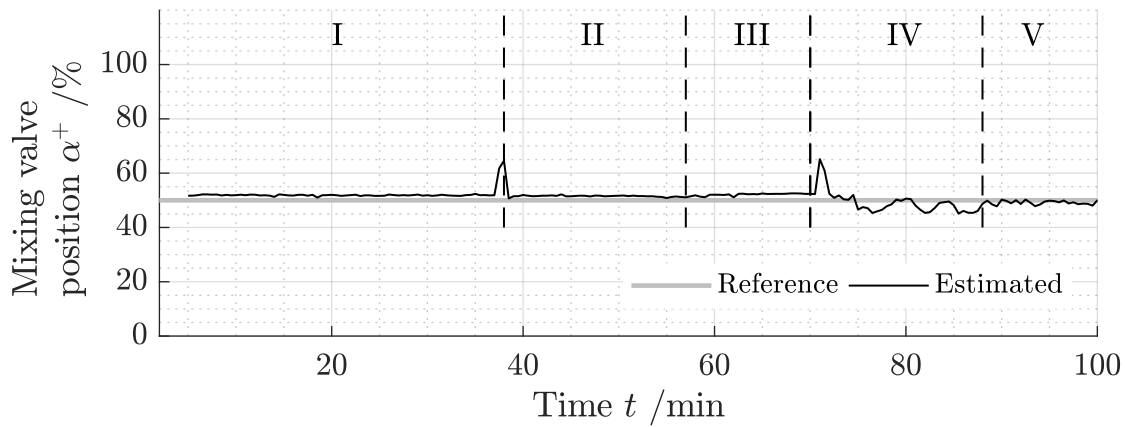
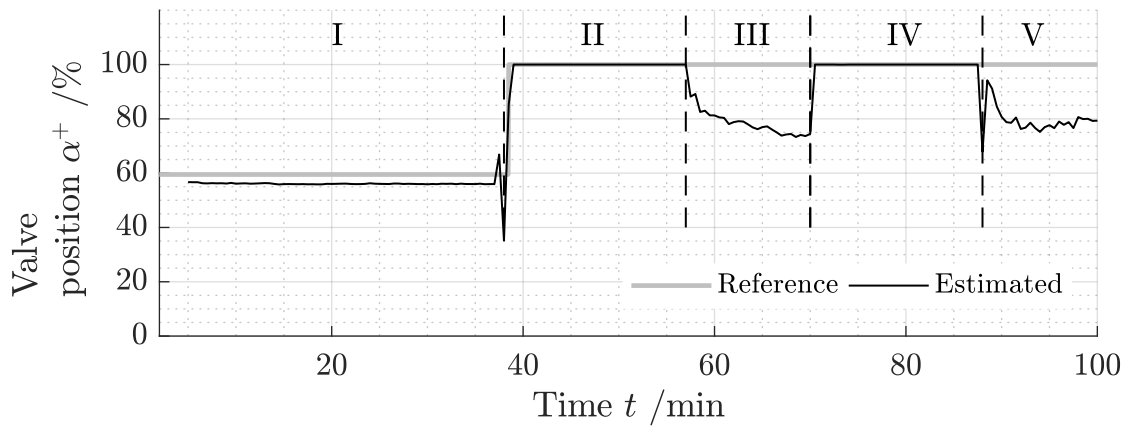


Figure 5.16: Estimated mixing valve positions α^+

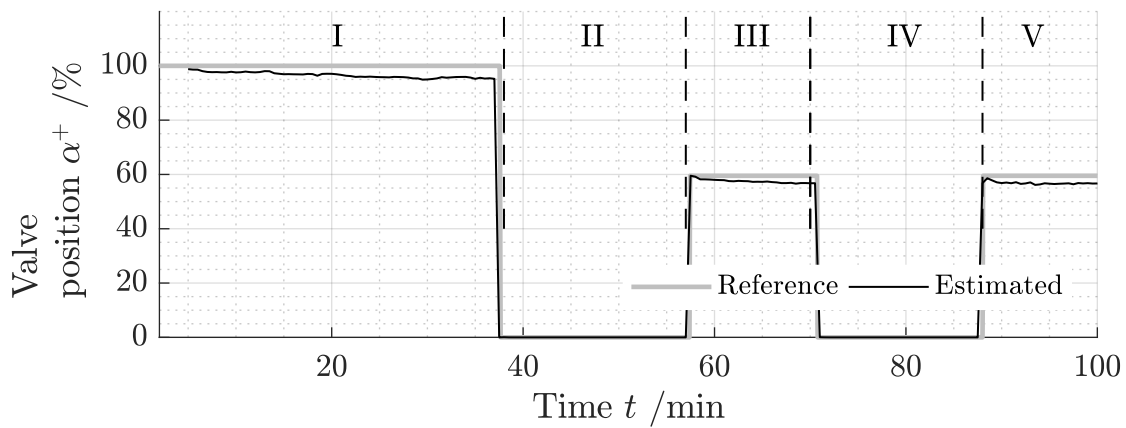
to fluctuations of the total mass flow rate introduced by transient driving as shown in Fig 5.15b. The model-based control approach aims to compensate the fluctuating flow rates by varying the mixing valve positions.

The valve positions of the air distribution valves are depicted in Fig 5.17. The model-based approach is capable to track the variations of the valve angles for both stationary operation and driving of the vehicle. Typical deviations from the real valve positions are $\Delta\alpha^+ < 20\%$. This corresponds only to a difference of the dimensionless volume flow rates < 0.015 . Major deviations occur only during the transition between the different operating conditions. The estimated positions remain also accurate under transient driving and good results are delivered.

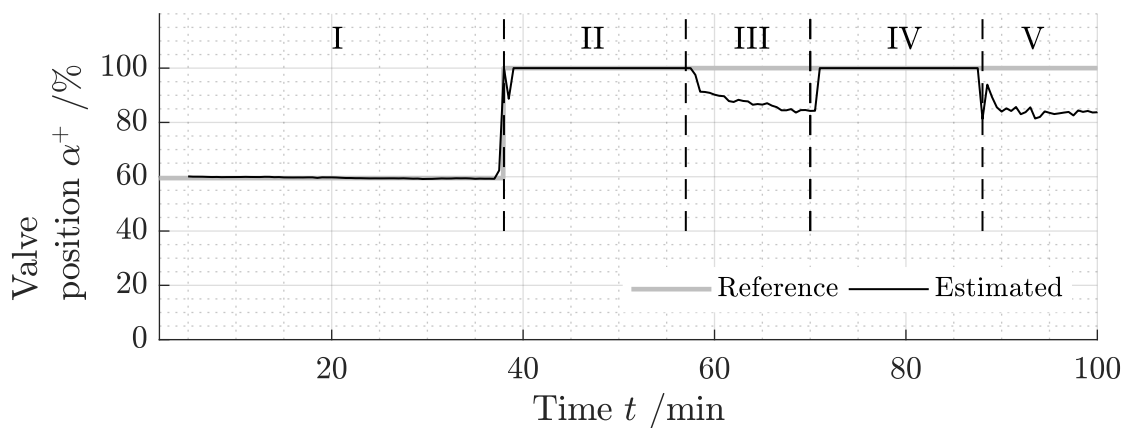
In Fig. 5.18 the simulated and measured outlet temperatures are compared with the temperatures predicted by the model based approach. The simulated outlet temperatures refer to the values which are computed from the real valve positions of Tab. 5.6. It can be seen that the absolute temperature error is less than 4 K at all outlets. This corresponds approximately to 0.1 of the total temperature increase at the respective outlet. As expected, the temperature differences between the measured outlet temperatures and the temperatures predicted by the model-based approach are smaller. This is a result from the minimization procedure, which aims to meet the measured values.



(a) Left foot

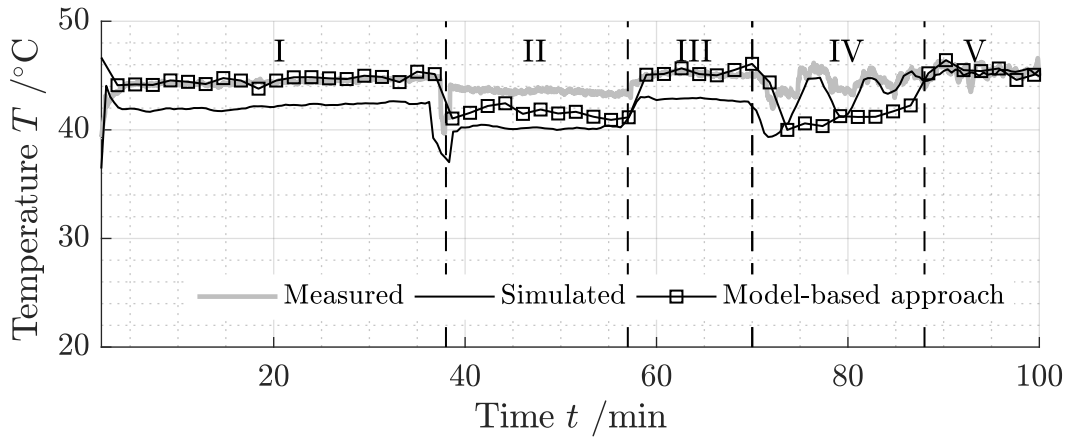


(b) Left side

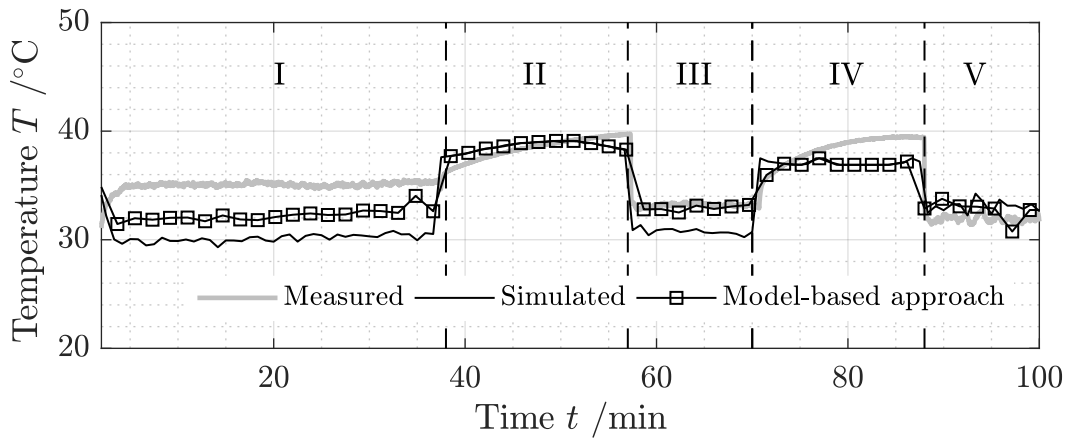


(c) Left face

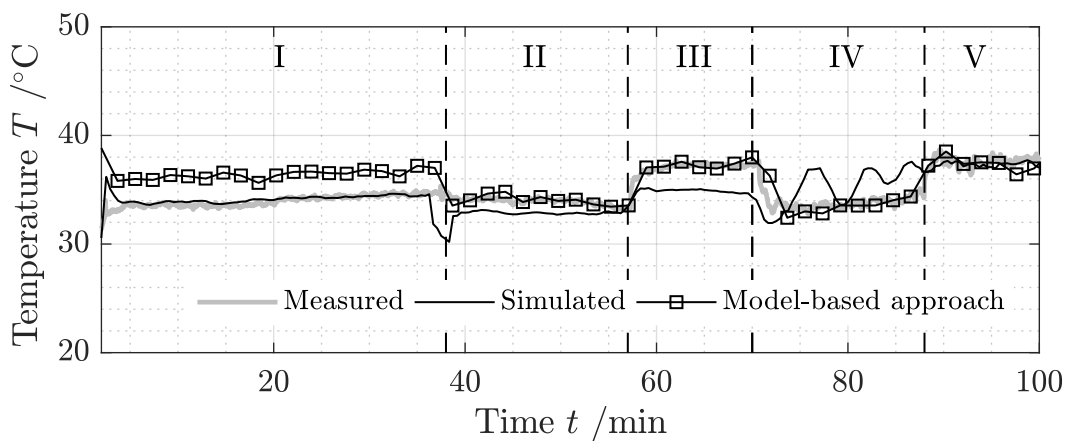
Figure 5.17: Estimated valve positions α^+ using the outlet quantities measured as setpoints



(a) Left foot outlet



(b) Left side outlet



(c) Left face outlet

Figure 5.18: Estimated valve positions α^+ using the outlet temperatures measured as setpoints

According to these results, it can be concluded that the model-based approach is also applicable to the real vehicle. The procedure tracks the changes of the valve positions accurately and provides good estimates for the operating conditions. These estimated parameters result in the prescribed outlet temperatures of the HVAC unit. The application of the model-based procedure eliminates the need of temperature sensors since the input values for the HVAC unit are computed by using the HVAC model.

6 Summary and Conclusions

A modeling approach for HVAC units was developed to predict the outlet temperatures aiming at model-based climate control. Proper Orthogonal Decomposition (POD) was used together with a novel weighting procedure to model the mixing process in the HVAC unit. The proposed weighting procedure is a combination of well-established physical models with POD to generate an accurate Reduced Order Model.

Based on the literature review it was shown that physical models perform with high accuracy and are easy to generalize. This is in particular important to integrate the model procedure in the industrial development process. A physical model was applicable for most of the components of the HVAC unit. Only the mixing process in the mixing cavity could not be described by these methods. To overcome this issue, Proper Orthogonal Decomposition was proposed for Reduced Order Modeling of the mixing process. POD has been widely applied to fluid mechanics. Traditionally, it is used to extract orthogonal eigenfunctions or so-called POD modes from spatial flow fields. By incorporating the Navier Stokes Equations, a Reduced Order Model can be generated. This application of the POD is known as POD-Galerkin (G-POD) procedure. The high dimensional flow field is modeled by the G-POD method and afterwards the integral outlet values can be computed for climate control. However, the G-POD procedure is in particular suitable if distributed flow variables, e.g. the temperature distribution at the outlet, are required. In addition, high computational effort is needed to obtain the numerical input data set for the G-POD method. For example, one CFD simulation of the investigated HVAC unit requires 5 hours using 120 CPU cores. The same operating condition is measured in 0.3 hours using the experimental setup from chapter 3. The time to obtain data for a parameter combination of the HVAC unit is important, because the input for the POD is a data set acquired at selected operating conditions covering the relevant operating range.

Therefore, a novel application of the POD was proposed to eliminate the need for numerical simulations while increasing accuracy. The developed POD approach focused solely on the control-relevant output parameters, which were the volume flow rates and enthalpy flow rates at the outlets. Instead of incorporating the Navier Stokes Equations, the POD model was combined with a traditional fluid resistance network model. This network model provided the volume flow rates at the outlets. From the flow distribution, the weighting coefficients for the POD modes were estimated. Afterwards, the integral enthalpy flow rates were computed using these estimated coefficients. The strength of this method is that not observed output values are estimated from observed states. This is known as Output-based POD (O-POD). O-POD was compared with the traditional Galerkin method to predict the integral outlet values. A numerical benchmark model of a two-dimensional mixing cavity was used to gather an adequate data set for both POD methods. Based on these results, the following conclusions were made from the two-dimensional benchmark case:

- Operating conditions, which lead to a significantly different system behavior and are not sufficiently represented by the input data set, can not be predicted accurately. Therefore, the selection strategy of the data set is important to guarantee model robustness.
- The POD-Galerkin method models the high dimensional flow field. Consequently, G-POD needs more modes than O-POD for a similar prediction accuracy of the integral outlet values. For climate control, the increased information of the complete flow field has no significant advantage since only integral values are required. However, in comparison with CFD simulations, G-POD is a powerful alternative to obtain distributed values of the flow field.
- The modes from the O-POD method reflect important mechanisms of mixing. These mechanisms can be analyzed by inspecting the modes. Since the outlet temperatures are different at the outlets, the mode values of the flow distribution and enthalpy flow rates are different too. Each mode corresponds to an individual change of the outlet values. For example, the first mode reflects a change of the flow distribution from the

foot outlet to the defrost and face outlets. Due to different outlet temperatures, this leads only to a change of the enthalpy flow rates between the foot and face outlets.

The O-POD procedure showed good performance to model the mixing process of the numerical benchmark model. Next, the approach was integrated into a system simulation of a real HVAC unit. The HVAC model consisted of 4 sub-models, beside the O-POD model. These sub-models covered the blower, the air distribution system, the heat exchanger and the heat transfer in the ventilation ducts. Two experimental data sets were acquired by a laboratory test rig as input for the O-POD to generate a model of the real mixing process of the HVAC unit. The first data set is known as original data set and included only measured values. This original data set was extended based on physical assumptions to increase the accuracy over a wide operating range of the model and to cover asymptotic behavior. An individual O-POD model was generated from each data set. To compare the models generated from the original data set and extended set with each other, parameter configurations different to the POD input were measured with the test rig. The measurements used for the model assessment are known as test data set. Additionally, real driving data was obtained by a test vehicle. Finally, the derived and calibrated HVAC model was compared with the measured test data set from the test rig and measurements of the real driving scenario. The main findings can be summarized as follows:

- The results show that the performance of the POD models generated by the original and the extended data set are equivalent in the calibrated range of the model. Outside of calibration range, the POD model from the extended data set remains accurate (accumulated error < 10 %). In contrast, the error of the model from original data set increases (accumulated error > 20 %) significantly. Introducing data on physical assumptions can be seen as a good strategy to improve the robustness of the procedure. The POD model generated from the extended data set was utilized for further investigations.

-
- As expected, the physical models exhibit high accuracy. The accumulated absolute error of the volume flow rates at the outlets is less than 6 %. The heat transfer in the heat exchanger can be predicted with an accuracy of 15 %. On the system level, the mean error of the outlet temperatures is approximately 1.5 K. The maximum error is below 4 K for almost all test configurations. The model provides accurate values also under real driving conditions. Typical deviations of the outlet temperatures are around 2 K and the maximum error is less than 5 K. This is equivalent to a relative error below 10% at the outlets. Only during the first minutes of transient heating, temperature errors up to 10 K occur.
 - Linear and non-linear relations of the mixing process are revealed by analysing the POD modes. This a strength of the POD applied to output values. A change of the flow through the heat exchanger has almost a linear influence on the enthalpy flow rates at the outlets. In contrast, a deviation of the flow distribution from the mean distribution results in a non-linear shift of the enthalpy flow rates among the outlets due to different outlet temperatures.

The system simulation of the HVAC model was further integrated into a model-based control approach. This approach was proposed as an alternative to the standard feedback control approach used in vehicles. Instead of measuring the outlet temperatures as feedback, the HVAC model provided the valve positions for the outlet values prescribed by the Automatic Climate Control (ACC). To evaluate the model-based control scheme, different setpoints for the outlet temperatures and volume flow rates were selected. These setpoints corresponded to typical operating conditions of the HVAC unit in the vehicle. As output of the model-based control approach, valve positions were obtained. Subsequently, the temperatures and volume flow rates for these valve positions had been measured with the test rig. Furthermore, the control approach was assessed with real driving data from the test vehicle. Finally, the experimental data acquired from the test rig and the vehicle was compared with the setpoints.

The following findings were obtained:

- The results from the test rig show that the predicted valve positions lead in general to the specified volume flow rates and steady temperatures at the outlets. The errors of the flow rates at the outlets are lower than the measurement accuracy (0.015). The differences between the modeled and measured outlet temperatures are smaller than 2 K.
- Deviations up to 4 K between specified outlet temperatures and measured values are seen, because the model-based control approach aims to meet all outlet values in a least square sense.
- Also in the vehicle, good results are delivered by the model-based control scheme at quasi-steady state. The predicted valve positions lead to differences around 3 K. Thus, the proposed control approach eliminates the need for costly sensors.

Outlook

The elimination of the temperature errors identified during highly transient operation could be in the focus of a future work. It is expected that these deviations can be reduced by introducing a suitable description of the transient heat transfer upstream of the ventilation ducts.

It is recommended to study different structures of the experimental data set provided as input for the POD as this was identified to be important for the model robustness. It can be expected that a suitable selection procedure enhances the accuracy of the POD model and reduces the amount of experimental data needed. Both aspects are important for the industrial application.

While in this work the elimination of sensors was discussed using model-based control, it could also be applied for system diagnostics of the utilized sensor equipment. Unexpected differences between measured and predicted values resulting from hardware failure could be detected. This would increase the robustness of the ACC.

In future work, the POD could also be applied to other application fields to reveal relevant system dynamics for a deeper understanding of dominant pro-

cesses and physical phenomena. The approach is in particular suitable if only a moderate amount of data is available.

A Sub-Models of the HVAC Unit

Blower Model

The blower provides the total mass flow rate for the HVAC unit. A simplified sketch of the blower is shown in Fig. A.1.

The system is considered to be steady state and incompressible. Changes in the potential and kinetic energy are neglected and the energy balance reads

$$2\pi M n \eta_{\text{tot}} = \dot{V}_{\text{tot}} (p_2 - p_1), \quad (\text{A.1})$$

where M denotes the torque of the blower and η_{tot} is the efficiency. The torque

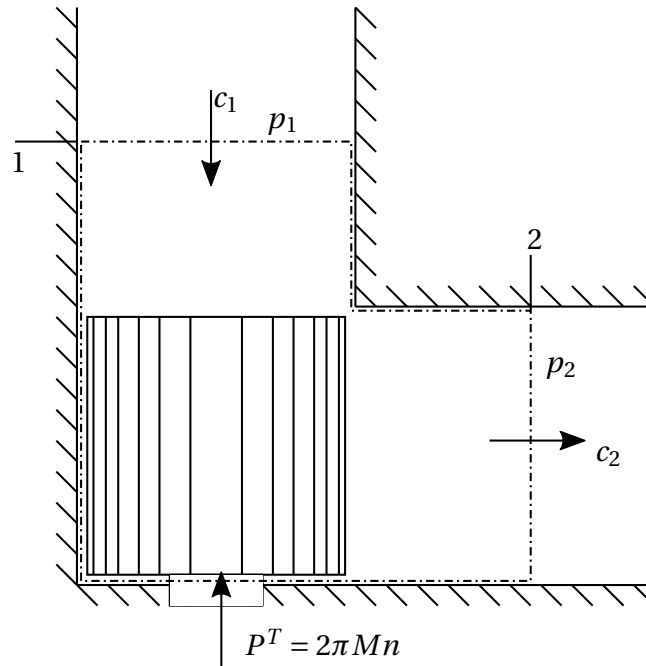


Figure A.1: Energy balance applied to the blower

M is available from the Electric Control Unit (ECU) in the vehicle. The differential pressure $\Delta p = (p_2 - p_1)$ and the efficiency η_{tot} can be described by a function of the RPM and the volume flow rate \dot{V}_{tot}

$$\Delta p = f(n, \dot{V}_{\text{tot}}), \quad (\text{A.2a})$$

$$\eta_{\text{tot}} = f(n, \dot{V}_{\text{tot}}). \quad (\text{A.2b})$$

The functions in Eq. A.2 are substituted in Eq. A.1 and can be solved for the volume flow rate \dot{V}_{tot} .

Fluid Resistance Network

The fluid resistance network contains two parallel major flow branches, which correspond to the left and right climate zone of the HVAC unit. These branches and the complete network are shown in Fig. 4.18. The pressure p_0 corresponds to the pressure at outlet of the evaporator while the nodal pressure p_{cabin} denotes the cabin pressure. The pressure in the mixing cavity p_{cavity} is considered to be constant. Each flow branch consists of the bypass, the air flow path through the HX (1) and the air distribution system (2).

As the result of the network model, the dimensionless mass flow rate at a specific outlet of the left climate zone is calculated from [61]

$$\dot{m}_{L,n}^+ = \frac{1}{1 + \frac{\sqrt{R_{L,M}^2 + R_{L,D}^2}}{\sqrt{R_{R,M}^2 + R_{R,D}^2}}} \cdot \frac{R_{L,D}}{\frac{1}{A_{L,n}} \sqrt{\frac{\zeta_{L,n}}{2\rho_{L,n}}}} \quad (\text{A.3})$$

and for the right zone from

$$\dot{m}_{R,n}^+ = \frac{1}{1 + \frac{\sqrt{R_{R,M}^2 + R_{R,D}^2}}{\sqrt{R_{L,M}^2 + R_{L,D}^2}}} \cdot \frac{R_{R,D}}{\frac{1}{A_{R,n}} \sqrt{\frac{\zeta_{R,n}}{2\rho_{R,n}}}}. \quad (\text{A.4})$$

The coefficients $R_{L,M}$ to $R_{R,D}$ are summarized in Tab. A.1.

Inner iterations i of the FRN are performed to account for the dependence of the Reynolds number on the resistance of the HX. The FR network is solved

Table A.1: Summarized coefficients of the FR network model

	Mixing valves and HX	Air distribution valves and ventilation ducts
Left	$R_{L,M} = \frac{\frac{1}{\sqrt{2}}}{A_{L,Byp} \sqrt{\frac{\rho_{L,Byp}}{\zeta_{L,Byp}}} + A_{L,HX} \sqrt{\frac{\rho_{L,HX}}{\zeta_{L,HX}}}}$	$R_{L,D} = \frac{\frac{1}{\sqrt{2}}}{\sum_{n=1}^4 \left(A_{L,n} \sqrt{\frac{\rho_{L,n}}{\zeta_{L,n}}} \right)}$
Right	$R_{R,M} = \frac{\frac{1}{\sqrt{2}}}{A_{R,Byp} \sqrt{\frac{\rho_{R,Byp}}{\zeta_{R,Byp}}} + A_{R,HX} \sqrt{\frac{\rho_{R,HX}}{\zeta_{R,HX}}}}$	$R_{R,D} = \frac{\frac{1}{\sqrt{2}}}{\sum_{n=1}^4 \left(A_{R,n} \sqrt{\frac{\rho_{R,n}}{\zeta_{R,n}}} \right)}$

Table A.2: Loss coefficients of the FRN

Loss Coefficient	Individual losses	Description	Data
$\zeta_{n,k}$	$= \zeta_{Valve} (\alpha^+)$	Air distribution valve	Idelchik and Fried [39] and Massoud [64]
k= Left/Right n= Defrost, ... ,Foot	$+ \zeta_{Duct}$ $+ \zeta_{Emp}$	Ventilation duct Empirical	Measurements Minimization problem Eq. 4.3
$\zeta_{n,Bypass}$	$= \zeta_{Valve} (\alpha^+)$	Valve	Idelchik and Fried [39] and Massoud [64]
	$+ \zeta_{Emp}$	Empirical	Minimization problem Eq. 4.3
$\zeta_{n,HX}$	$= \zeta_{Valve} (\alpha^+)$	Mixing valve	Idelchik and Fried [39] and Massoud [64]
	$+ \zeta_{HX} (Re)$	Heat Exchanger	Measurements

from an initial guess of the loss coefficients and the mass flow rates are calculated. The updated mass flow rates are subsequently applied to update the loss coefficients. Afterward the FRN is solved again with the updated coefficients. This iteration procedure is performed until the difference between the actual and updated resistances is

$$\sum |\zeta (Re)^i - \zeta (Re)^{i-1}| < 10^{-5}. \quad (\text{A.5})$$

Usually 3 iterations are required to meet the criterion from Eq. A.5. The loss coefficients of the FR network are summarized in A.2.

Heat Exchanger Model

The heat exchanger in the HVAC unit is separated into three sections. These sections are front left, front right and rear as shown in Fig. A.2.

Usually single component measurements are conducted during the design process of HVAC units. From these measurement, look up tables are gener-

ated for the efficiency of the HX. The efficiency η_{HX} is given by

$$\eta_{\text{HX}} = \frac{\dot{Q}_{\text{HX}}}{\dot{m}_{\text{Air}} c_{p,\text{Air}} (T_{\text{Coolant,In}} - T_{\text{Air,In}})}. \quad (\text{A.6})$$

It is the ratio of transferred energy scaled by the maximum permissible energy transfer. The efficiency is shown in Fig. A.3 for varying coolant volume flow rates and air mass flow rates. This data is gathered for homogenous inflow conditions for the entire inlet cross section of the HX.

The mass flow through the respective section n is scaled with an effective mass flow rate to compute the air temperature at the outlet of the HX. The effective mass flow rate reads

$$\dot{m}_{n,\text{HX}}^{\text{eff}} = \dot{m}_{n,\text{HX}} \frac{A_{\text{HX}}}{A_n}, \quad (\text{A.7})$$

where A_{HX} denotes the entire inlet area of the HX and A_n refers to the area of the respective section of the HX, e.g. front left. It is considered that the efficiency of the HX is also applicable to a specific section of the HX. Thus, the efficiency is computed for the effective mass flow rate by linear interpolation. The actual air temperature at the outlet of the HX is determined from the effi-

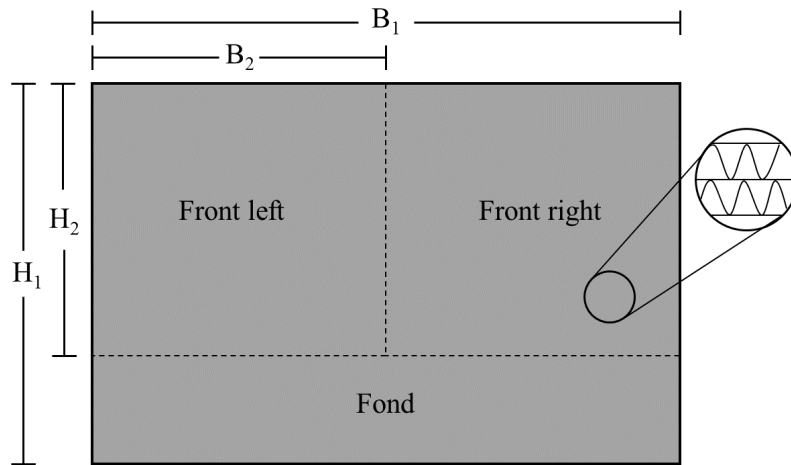


Figure A.2: Sections of the heat exchanger

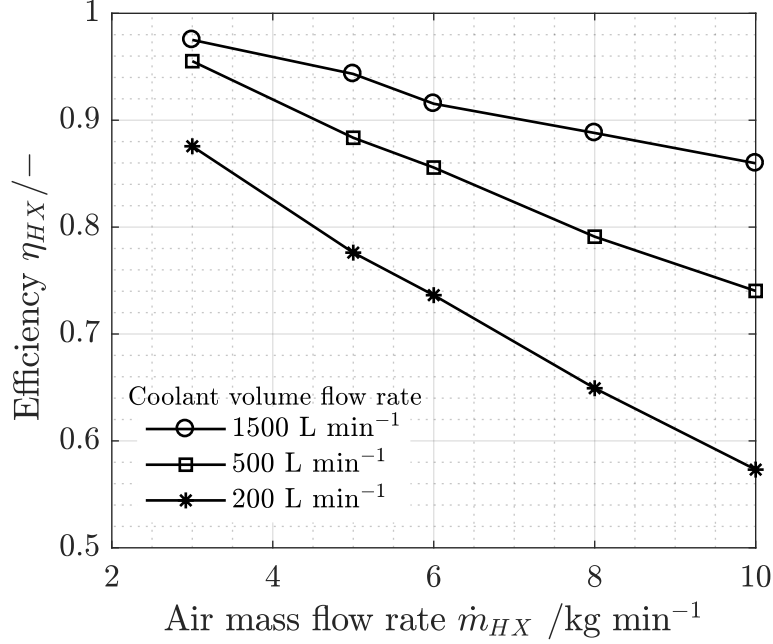


Figure A.3: Efficiency of the heat exchanger

ciency. Furthermore the heat transfer in the HX can be computed

$$T_{Air,n,HX} = \eta_{HX} (T_{Coolant,In} - T_{Air,In}) + T_{Air,In}, \quad (\text{A.8a})$$

$$\dot{Q}_{n,HX} = \dot{m}_{n,HX} c_{p,Air} (T_{Air,n,HX} - T_{Air,In}). \quad (\text{A.8b})$$

Heat Transfer in the Ventilation Ducts

The heat transfer in the ventilation ducts is modeled with a nodal network as shown in Fig. 4.19. The temperatures of the nodes correspond to the ventilation duct, the surrounding air layer of the duct and the discretized dashboard [57, 96]. It is assumed that the heat transfer of the vehicle structure can be simplified to that of a one dimensional plane wall and that temperature gradients of the vehicle structure in axial direction are negligible $\frac{dT}{dx} \approx 0$. An explicit discretization scheme is applied, which results in a linear set of equations

$$\mathbf{T}^{t+\Delta t} = [\mathbf{K}\mathbf{T}^t + \dot{\mathbf{Q}}] \Delta t + \mathbf{T}^t. \quad (\text{A.9})$$

where the matrix \mathbf{K} includes the resistances introduced by forced convection and thermal conduction. The non-linear terms, e.g. radiative heat transfer, are

included in the matrix $\dot{\mathbf{Q}}$ and calculated from the actual temperatures \mathbf{T}^t . For the driving data in chapter 5, it was considered that the vehicle structure temperature, cabin temperature and ambient temperature are almost equal because of low solar radiation and a large time interval (≈ 12 hours) without operating the vehicle. Therefore, the cabin temperature $T_C(t=0)$ has been prescribed as initial temperature of the vehicle structure at $t=0$ for the driving cycle. The nodal network is only applied for the left and right side outlets. Model the heat transfer in the other ducts is not considered to be necessary due to their small length and thus low heat transfer.

B Measurement Instrumentation

B.1 Detailed Error Analysis of the Test Rig

To estimate uncertainties, a propagation method is used which reads for the total mass flow rate

$$u_{\dot{m}_{tot}} = \sqrt{\left(\frac{\partial \dot{m}_{tot}}{\partial \Delta p}\right)^2 u_{\Delta p}^2 + \left(\frac{\partial \dot{m}_{tot}}{\partial \rho}\right)^2 u_{\rho}^2 + \left(\frac{\partial \dot{m}_{tot}}{\partial D}\right)^2 u_D^2}. \quad (\text{B.1})$$

The propagation equation links the partial derivatives of Eq. B.1 with the measurement error of the differential pressure sensor, the expected errors of the diameter and the error of the ambient air density. The density is calculated by [40]

$$\rho = \frac{p}{R_s T}, \quad (\text{B.2})$$

where p is the ambient pressure, R_s the specific gas constant and T the ambient temperature. The specific gas constant is given by

$$R_s = \frac{R_d}{1 - \frac{\varphi p_v}{p} \left(1 - \frac{R_d}{R_v}\right)}. \quad (\text{B.3})$$

In Eq. B.3 R_s denotes the specific gas constant for dry air with $287.058 \text{ J kg}^{-1}\text{K}^{-1}$, $p_v=23.385 \text{ Pa}$ is the pressure of water vapor, $R_v=461.523 \text{ J kg}^{-1}\text{K}^{-1}$ corresponds to the specific gas constant for water vapor and φ refers to the relative air humidity. The fluctuations of these quantities are expected to be small (see Tab. B.1) since the measurements are performed in an air-conditioned laboratory.

Table B.1: Expected fluctuations of the ambient air

Quantity	Value
Relative humidity φ	0.2 ± 0.1
Ambient pressure	102000 Pa
Ambient temperature	$23^\circ\text{C} \pm 3^\circ\text{C}$

Thus, an average density of $\rho=1.2 \text{ kgm}^{-3}$ has been used for the calculation of the total mass flow rates. According to the expected fluctuations of the ambient air from Tab.B.1 the uncertainty of the density u_ρ results in 2 %. The partial derivatives from Eq. B.1 lead to

$$\left(\frac{\partial \dot{m}_{tot}}{\partial \Delta p}\right) = \frac{\pi D^2}{4\sqrt{2}} \sqrt{\frac{\rho}{\Delta p}}, \quad (\text{B.4a})$$

$$\left(\frac{\partial \dot{m}_{tot}}{\partial \rho}\right) = \frac{\pi D^2}{4\sqrt{2}} \sqrt{\frac{\Delta p}{\rho}}, \quad (\text{B.4b})$$

$$\left(\frac{\partial \dot{m}_{tot}}{\partial D}\right) = \frac{\pi D}{\sqrt{2}} \sqrt{\rho \Delta p}. \quad (\text{B.4c})$$

In Fig. B.1 the relative error norm of total mass flow rate $u_{\dot{m}_{tot}}$ is shown for varying mass flow rates. It can be seen that relative error is comparatively high at low mass flow rates ($< 3 \text{ kg min}^{-1}$) because the measured differential pressure becomes less accurate. For the mass flow range from 3 kg min^{-1} to 10 kg min^{-1} the error is less than 2%, which is considered to be sufficiently accurate and covers a typical operating range of HVAC units. The error of the mass flow rates at the outlets is evaluated. The propagation equation for dimensionless mass flow rates at the outlets results in

$$u_{\dot{m}_{n,k}^+} = \sqrt{\sum_i^2 \sum_j^4 \left(\frac{\partial \dot{m}_{n,k}^+}{\partial \rho_{i,j}}\right)^2 u_{\rho_{i,j}}^2 + \sum_i^2 \sum_j^4 \left(\frac{\partial \dot{m}_{n,k}^+}{\partial u_{i,j}}\right)^2 u_{u_{i,j}}^2}. \quad (\text{B.5})$$

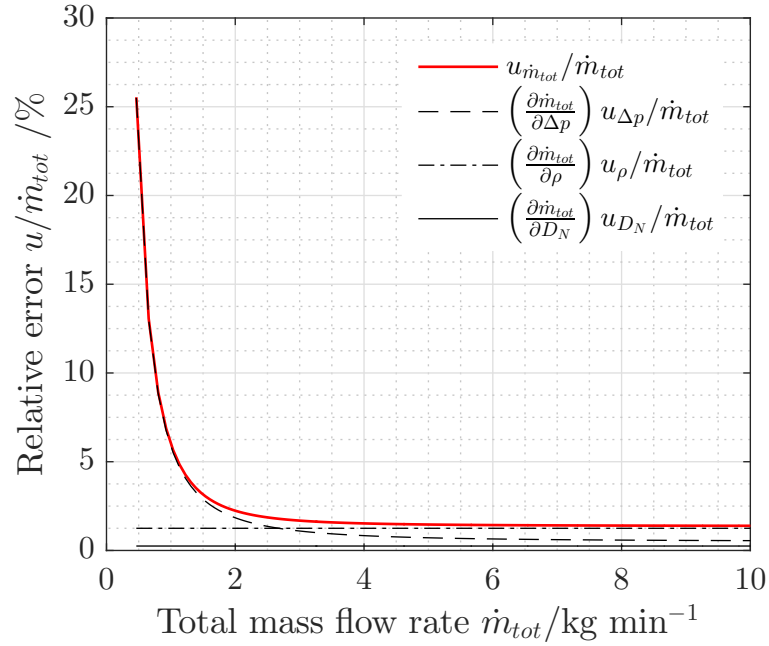


Figure B.1: Relative error of the total mass flow rate

with the partial derivatives

$$i = n, j = k: \quad \left(\frac{\partial \dot{m}_{nk}^+}{\partial u_{i,j}} \right) = \frac{\rho_{nk}}{\left(\sum_m^2 \sum_l^4 \rho_{m,l} u_{m,l} \right)} - \frac{\rho_{n,k}^2 u_{n,k}}{\left(\sum_m^2 \sum_l^4 \rho_{m,l} u_{m,l} \right)^2}, \quad (\text{B.6a})$$

$$i \neq n, j \neq k: \quad \left(\frac{\partial \dot{m}_{nk}^+}{\partial u_{i,j}} \right) = - \frac{\rho_{i,j} \rho_{n,k} u_{n,k}}{\left(\sum_m^2 \sum_l^4 \rho_{m,l} u_{m,l} \right)^2}, \quad (\text{B.6b})$$

$$i = n, j = k: \quad \left(\frac{\partial \dot{m}_{nk}^+}{\partial \rho_{i,j}} \right) = \frac{u_{nk}}{\left(\sum_m^2 \sum_l^4 \rho_{m,l} u_{m,l} \right)} - \frac{\rho_{n,k} u_{n,k}^2}{\left(\sum_m^2 \sum_l^4 \rho_{m,l} u_{m,l} \right)^2}, \quad (\text{B.6c})$$

$$i \neq n, j \neq k: \quad \left(\frac{\partial \dot{m}_{nk}^+}{\partial \rho_{i,j}} \right) = - \frac{\rho_{n,k} u_{n,k} u_{i,j}}{\left(\sum_m^2 \sum_l^4 \rho_{m,l} u_{m,l} \right)^2}. \quad (\text{B.6d})$$

To evaluate error of the mass flow rates at the outlets a representative operating condition of a HVAC unit is chosen. The error is calculated for each outlet with the uncertainties given in Tab B.2. The resulting absolute error and the relative error of $\dot{m}_{n,k}$ are summarized in Tab.B.3. From this table it can be seen that the error of the dimensionless mass flow rates is lower than 0.015 at almost all outlets. The relative error at a specific outlet is approximately 10%

Table B.2: Uncertainties of the measured quantities used to evaluate the error of the mass flow rates at the outlets of the HVAC unit

Quantity	Uncertainty	Value	Comment
Mean velocity	u_U	1% FS = 0.2 m s ⁻¹ + 1.5% MV	Datasheet
Density	u_ρ	2%=0.024 kg m ⁻³	Expected uncertainty

Table B.3: Errors of the mass flow rates at the outlets of the HVAC unit

Outlet	Uncertainty $u_{m_{nk}}$	Relative uncertainty $u_{m_{nk}}$
Defrost left	0.0122	0.0975
Defrost right	0.0123	0.0978
Foot left	0.0112	0.0927
Foot right	0.0116	0.0945
Side left	0.0164	0.1146
Side right	0.0141	0.1054
Face left	0.0088	0.0799
Face right	0.0106	0.0899

which is considered as sufficiently accurate.

For the error evaluation of the enthalpy flow rates the propagation equation reads

$$u_{\dot{H}_{n,k}^+} = \sqrt{\sum_i^2 \sum_j^4 \left(\frac{\partial \dot{H}_{n,k}^+}{\partial \dot{m}_{i,j}^+} \right)^2 u_{\dot{m}_{i,j}^+}^2 + \sum_i^2 \sum_j^4 \left(\frac{\partial \dot{H}_{n,k}^+}{\partial T_{i,j}} \right)^2 u_{T_{i,j}}^2}. \quad (\text{B.7})$$

with the derivatives according to

$$i = n, j = k: \quad \left(\frac{\partial \dot{H}_{nk}^+}{\partial \dot{m}_{i,j}^+} \right) = \frac{T_{nk}}{\left(\sum_m^2 \sum_l^4 \dot{m}_{m,l}^+ T_{m,l} \right)} - \frac{\dot{m}_{n,k}^+ T_{n,k}^2}{\left(\sum_m^2 \sum_l^4 \dot{m}_{m,l}^+ T_{m,l} \right)^2}, \quad (\text{B.8a})$$

$$i \neq n, j \neq k: \quad \left(\frac{\partial \dot{H}_{nk}^+}{\partial \dot{m}_{i,j}^+} \right) = - \frac{\dot{m}_{n,k}^+ T_{n,k} T_{i,j}}{\left(\sum_m^2 \sum_l^4 \dot{m}_{m,l}^+ T_{m,l} \right)^2}, \quad (\text{B.8b})$$

$$i = n, j = k: \quad \left(\frac{\partial \dot{H}_{nk}^+}{\partial T_{i,j}} \right) = \frac{\dot{m}_{n,k}^+}{\left(\sum_m^2 \sum_l^4 \dot{m}_{m,l}^+ T_{m,l} \right)} - \frac{\dot{m}_{n,k}^+ \dot{m}_{n,k}^+ T_{n,k}}{\left(\sum_m^2 \sum_l^4 \dot{m}_{m,l}^+ T_{m,l} \right)^2}, \quad (\text{B.8c})$$

$$i \neq n, j \neq k: \quad \left(\frac{\partial \dot{H}_{nk}^+}{\partial T_{i,j}} \right) = - \frac{\dot{m}_{i,j}^+ \dot{m}_{n,k}^+ T_{n,k}}{\left(\sum_m^2 \sum_l^4 \dot{m}_{m,l}^+ T_{m,l} \right)^2}. \quad (\text{B.8d})$$

As it is shown in Tab. B.3 the error of the dimensionless mass flow rates is similar at each outlet. Thus, a constant uncertainty $u_{\dot{m}_{n,k}^+}$ of 0.015 is assumed for further calculations. Since the deviation of the 4 thermocouples of the measurement channels from each other are not significant (≤ 0.2 K), it is considered that the temperature inhomogeneity has no major influence on the results. Thus, the measurement tolerance u_T of the temperature (see calibration protocol Fig. B.2 of the calibrated thermocouples type K) leads to 0.2 K. With these values the uncertainty of the measured dimensionless enthalpy flow rates $u_{\dot{H}_{n,k}^+}$ become 0.015.

B.2 Specification of Measurement Instrumentation

Table B.4: Technical specification of the differential pressure sensor sensirion SDP1000L provided by the manufacturer

Specification	Value
Measuring range	0 Pa to 500 Pa
Output signal	0.25 V to 4 V
Accuracy	0.1% from full scale (FS) + 1% from measured value (MV)
Operating temperature	-10 °C to 60 °C

Table B.5: Technical specification of the 3D printer and material of the printed components

Specification	Value
System	EOS P 396
Technique	Selective laser sintering (SLS)
Material	Polyamide PA2200

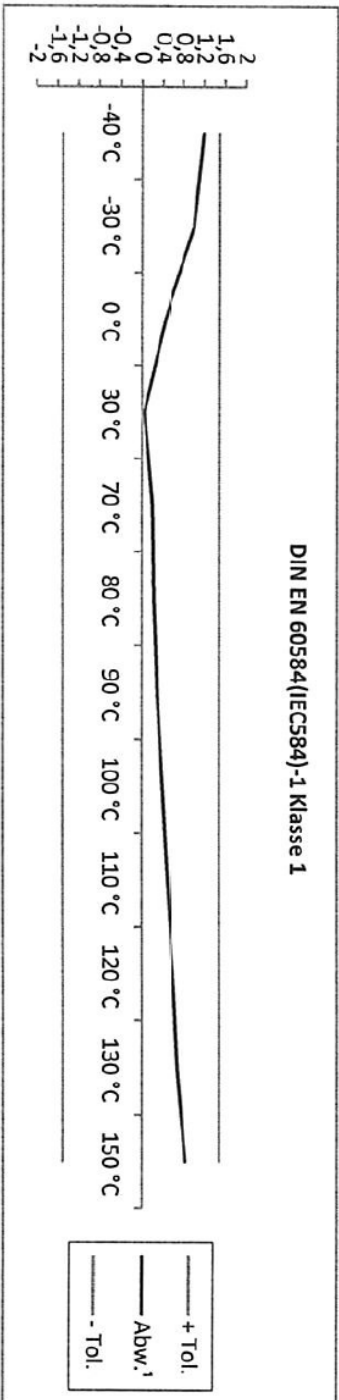
Table B.6: Technical specification of the anemometers Schiltknecht MiniAir6 Macro provided by the manufacturer

Specification	Value
Measuring range	0.2 m s^{-1} to 20 m s^{-1}
Output signal	0 V to 2 V
Accuracy	1% from full scale (FS) + 1.5% from measured value (MV)
Operating temperature	$-10\text{ }^{\circ}\text{C}$ to $80\text{ }^{\circ}\text{C}$
Response time of vane	8 s

Meßprotokoll des Elementes

Sollwert	Referenz [°C]	Prüf. [°C]	Prüf. [mV]	Abw. [K]	zul. Abw. [K]
-40	-39,85	-38,65	-1,4777	1,20	+/- 1,50
-30	-29,85	-28,84	-1,1125	1,01	+/- 1,50
0	0,18	0,63	0,0251	0,45	+/- 1,50
30	29,76	29,81	1,1952	0,05	+/- 1,50
70	68,34	68,54	2,7903	0,20	+/- 1,50
80	78,16	78,39	3,2003	0,23	+/- 1,50
90	87,99	88,28	3,6117	0,29	+/- 1,50
100	97,88	98,27	4,0260	0,39	+/- 1,50
110	107,76	108,25	4,4380	0,49	+/- 1,50
120	117,71	118,32	4,8513	0,61	+/- 1,50
130	127,66	128,35	5,2608	0,69	+/- 1,50
150	147,57	148,42	6,0734	0,85	+/- 1,50

Hiermit wird bestätigt, dass das/die ausgewiesene(n) Element(e) aus der angegebenen Charge hergestellt wurde(n). Auf geeignete Kompensationskontakte ist zu achten.



Kalibrierverfahren: Vergleichsmessung gegen Referenzelement im Kalibrierbad

Einbaulänge: ca. 80 mm

Umgebungsbedingungen (Klimaraum) :

Temperatur : 23 °C +/- 2K

Luftfeuchte : ca. 55 % rel.F.

Figure B.2: Calibration protocol of the thermocouples

Previous Publications

Teile dieser Dissertation wurden von dem Autor bereits vorab als Konferenz- und Zeitschriftenbeiträge veröffentlicht. Alle Vorveröffentlichungen sind entsprechend der gültigen Promotionsordnung ordnungsgemäß gemeldet und anschliessend aufgeführt. Sie sind deshalb nicht zwangsläufig im Detail einzeln referenziert. Vielmehr wurde bei der Referenzierung eigener Vorveröffentlichungen Wert auf Verständlichkeit und inhaltlichen Bezug gelegt.

Parts of this Ph.D. thesis have been published by the author beforehand in conference proceedings and journal papers. All of these prior printed publications are registered according to the valid doctoral regulations and listed below. Therefore, they are not necessarily quoted explicitly in the text. Whether they were referenced, depended on maintaining comprehensibility and providing all necessary context.

P. Christ and T. Sattelmayer. Reduced order modelling of flow and mixing in an automobile HVAC system using proper orthogonal decomposition. *Applied Thermal Engineering*, 133:211–223, 2018

P. Christ and T. Sattelmayer. Thermal modeling of an automotive HVAC unit using a coupled POD and flow resistance network approach. In *SAE International World Congress Experience*, 2018

Supervised Student Theses

Im Rahmen dieser Dissertation entstanden am Lehrstuhl für Thermodynamik, Technische Universität München in den Jahren 2016 bis 2018 unter wesentlicher wissenschaftlicher, fachlicher und inhaltlicher Anleitung des Autors die im Folgenden aufgeführten studentischen Arbeiten. Ergebnisse aus diesen Arbeiten sind in Teilen in das vorliegende Dokument eingeflossen. Der Autor dankt hiermit explizit allen ehemals betreuten Studenten für ihr Engagement bei der Unterstützung des hier behandelten Forschungsprojekts sowie der damit verknüpften Dissertation.

Associated with this Ph.D. thesis are a number of student theses (Bachelorarbeiten, Semesterarbeiten, Masterarbeiten) that were supervised by the author of the present work. These theses were prepared at the Lehrstuhl für Thermodynamik, Technische Universität München in the years 2016 through 2018 under the close supervision of the present author. Parts of these supervised theses have been incorporated into the present thesis. The author would like to express her sincere gratitude to all formerly supervised students for their commitment and support of this research project and of the Ph.D. thesis at hand.

Student	Thesis type, title, submission date
Boyang Lu	Bachelorarbeit, Entwicklung eines Rechenmodelles zur Vorhersage der Luftverteilung im Klimagerät, 15.11.2016
Tobias Korthals	Masterarbeit, Numerische Untersuchung der Ausblastemperaturen eines Klimagerätes, 13.12.2016
Ferdinand Wöhr	Semesterarbeit, Niederdimensionale Modellierung der Strömungstemperaturen in den Luftkanälen einer Fahrzeug-Klimaanlage, 28.07.2017
Gerrit Pauls	Bachelorarbeit, Entwicklung eines Modells zur Berechnung der Temperaturregulierung im Klimagerät, 18.10.2017
Mathias Lesjak	Bachelorarbeit, Modellierung einer Fahrzeugkabine mittels Proper Orthogonal De- composition, 23.10.2017
Johannes Lindenblatt	Bachelorarbeit, Erweiterung und Validierung eines instationären Modells zur Berech- nung der Wärmeverluste in Luftführungen , 29.11.2017
Julius Drost	Bachelorarbeit, Aufbau und Regelung eines Prüfstandes zur simultanen Messung der Ausblastemperaturen und der Volumenströme eines Klimagerätes, 20.12.2017
Andreas Fraunhofer	Masterarbeit, Vergleich 1D-Simulation und gekoppelte Simulation für das thermis- che Verhalten eines Heizsystems für Batterien in Elektrofahrzeugen, 11.06.2018

Bibliography

- [1] First Air Conditioned Auto. *Popular Science*, 123, 1933. Google-Books-ID: 7CcDAAAAMBAJ.
- [2] Federal Motor Vehicle Safety Standard No. 103. *Windshield defrosting and defogging systems*. Code of Federal Regulations, 1968.
- [3] A. Afram and F. Janabi-Sharifi. Review of modeling methods for HVAC systems. *Applied Thermal Engineering*, 67:507–519, 2014.
- [4] A. Afram and F. Janabi-Sharifi. Theory and applications of HVAC control systems – A review of model predictive control (MPC). *Building and Environment*, 72:343–355, 2014.
- [5] A. Afram and F. Janabi-Sharifi. Gray-box modeling and validation of residential HVAC system for control system design. *Applied Energy*, 137:134–150, 2015.
- [6] A. Afram, F. Janabi-Sharifi, A. S. Fung, and K. Raahemifar. Artificial neural network (ANN) based model predictive control (MPC) and optimization of HVAC systems: A state of the art review and case study of a residential HVAC system. *Energy and Buildings*, 141:96–113, 2017.
- [7] Z. Afroz, G.M. Shafiullah, T. Urme, and G. Higgins. Modeling techniques used in building HVAC control systems: A review. *Renewable and Sustainable Energy Reviews*, 83:64–84, 2018.
- [8] E. Aggelogiannaki, H. Sarimveis, and D. Koubogiannis. Model predictive temperature control in long ducts by means of a neural network approximation tool. *Applied Thermal Engineering*, 27:2363–2369, 2007.

- [9] P. Astrid. *Reduction of process simulation models: a proper orthogonal decomposition approach*. PhD thesis, Technische Universiteit Eindhoven, 2004.
- [10] P. Astrid, S. Weiland, K. Willcox, and T. Backx. Missing point estimation in models described by proper orthogonal decomposition. *IEEE Transactions on Automatic Control*, 53:2237–2251, 2008.
- [11] H. D. Baehr and S. Kabelac. *Thermodynamik: Grundlagen und technische Anwendungen*. Springer-Verlag, 2012.
- [12] G. Berkooz, P. Holmes, and J. L. Lumley. The proper orthogonal decomposition in the analysis of turbulent flows. *Annual Review of Fluid Mechanics*, 25:539–575, 1993.
- [13] T. Bui-Thanh, M. Damodaran, and K. Willcox. Proper orthogonal decomposition extensions for parametric applications in compressible aerodynamics. In *21st AIAA Applied Aerodynamics Conference*, 2003.
- [14] Buick. Heating and AC Folder. Brochure, 1953. URL https://www.uniquecarsandparts.com.au/brochures_1953_buick_heating_aircon. Accessed: 2010-10-28.
- [15] A. Chatterjee. An introduction to the proper orthogonal decomposition. *Current Science*, 78:808–817, 2000.
- [16] Y. Chen and S. Treado. Development of a simulation platform based on dynamic models for HVAC control analysis. *Energy and Buildings*, 68:376–386, 2014.
- [17] C. C. Chiu, N. C. Tsai, and C. C. Lin. Construction of thermodynamic model and temperature regulation by near-LQR for electric vehicle. *International Journal of Thermal Sciences*, 81:106–117, 2014.
- [18] P. Christ and T. Sattelmayer. Reduced order modelling of flow and mixing in an automobile HVAC system using proper orthogonal decomposition. *Applied Thermal Engineering*, 133:211–223, 2018.

- [19] P. Christ and T. Sattelmayer. Thermal modeling of an automotive HVAC unit using a coupled POD and flow resistance network approach. In *SAE International World Congress Experience*, 2018.
- [20] S. Daly. *Automotive Air Conditioning and Climate Control Systems*. Butterworth-Heinemann, 2006.
- [21] G. Diaz, M. Sen, K. T. Yang, and R. L. McClain. Dynamic prediction and control of heat exchangers using artificial neural networks. *International Journal of Heat and Mass Transfer*, 44:1671–1679, 2001.
- [22] EN ISO DIN 5801. *Industrial fans-performance testing using standardized airways*. Deutsches Institut für Normung e. V., 2011.
- [23] B. Dong, Z. O’Neill, D. Luo, and B. Trevor. Development and calibration of a reduced-order energy performance model for a mixed-use building. In *Proceedings of Building Simulation*, 2013.
- [24] J. Drost. *Aufbau und Regelung eines Prüfstandes zur simultanen Messung der Ausblastemperaturen und der Volumenströme eines Klimagerätes*. Student thesis at the chair of thermodynamics, Technische Universität München, 2017.
- [25] Z. M. Durovic and B. D. Kovacevic. Control of heating, ventilation and air conditioning system based on neural network. In *7th Seminar on Neural Network Applications in Electrical Engineering*, 2004.
- [26] H. Elarga, M. De Carli, and A. Zarrella. A simplified mathematical model for transient simulation of thermal performance and energy assessment for active facades. *Energy and Buildings*, 104:97–107, 2015.
- [27] R. Everson and L. Sirovich. Karhunen-Loeve procedure for gappy data. *J. Opt. Soc. Am. A*, 12:1657–1664, 1995.
- [28] P. O. Fanger. *Thermal comfort: Analysis and applications in environmental engineering*. Danish Technical Press, 1970.
- [29] Y. Farzaneh and A. A. Tootoonchi. Controlling automobile thermal comfort using optimized fuzzy controller. *Applied Thermal Engineering*, 28: 1906–1917, 2008.

- [30] B. Flieger. *Innenraummodellierung einer Fahrzeugkabine in der Programmiersprache Modelica*. PhD thesis, RWTH Aachen, 2013.
- [31] D. Ghebru. *Modellierung und Analyse des instationären thermischen Verhaltens von Verbrennungsmotor und Gesamtfahrzeug*. PhD thesis, Karlsruher Institut für Technologie, 2013.
- [32] B. Glück. *Hydrodynamische und gasdynamische Rohrströmung, Druckverluste*. Verlag Bauwesen, Berlin, 1988.
- [33] H. Großmann. *Pkw-Klimatisierung: Physikalische Grundlagen und technische Umsetzung*. Springer Vieweg, 2013.
- [34] J. Hager and T. Anzenberger. Eine umfassende Methode zur frühzeitigen Analyse der Luftströmungen in Klimageräten, Ausströmern und Kanälen. In *PKW-Klimatisierung III: Klimakonzepte, Regelungsstrategien und Entwicklungsmethoden*, 2003.
- [35] M. Hakenberg. *Modellreduktion und Regelung von Strömungsprozessen mit dem POD-Galerkin-Verfahren*. PhD thesis, RWTH Aachen, 2015.
- [36] V. S. K. V. Harish and A. Kumar. A review on modeling and simulation of building energy systems. *Renewable and Sustainable Energy Reviews*, 56:1272–1292, 2016.
- [37] P. Holmes, J. L. Lumley, G. Berkooz, and C. W. Rowley. *Turbulence, coherent structures, dynamical systems and symmetry*. Cambridge University Press, 2012.
- [38] B. S. K. K. Ibrahim, M. A. N. Aziah, S. Ahmad, R. Akmeliawati, H. M. I. Nizam, A. G. A. Muthalif, S. F. Toha, and M. K. Hassan. Fuzzy-based temperature and humidity control for HV AC of electric vehicle. *Procedia Engineering*, 41:904–910, 2012.
- [39] I. E. Idelchik and E. Fried. *Handbook of hydraulic resistance*. Hemisphere Publishing, 1986.
- [40] Verfahrenstechnische Gesellschaft im VDI. *VDI-Wärmeatlas: Berechnungsblätter für den Wärmeübergang*. Deutscher Ingenieur-Verlag, 1957.

- [41] F. P. Incropera, D. P. DeWitt, T. L. Bergman, and A. S. Lavine. *Fundamentals of heat and mass transfer*. John Wiley & Sons, 2006.
- [42] M. J. Jiménez, H. Madsen, and K. K. Andersen. Identification of the main thermal characteristics of building components using matlab. *Building and Environment*, 43:170–180, 2008.
- [43] P. Kadlec, B. Gabrys, and S. Strandt. Data-driven soft sensors in the process industry. *Computers & Chemical Engineering*, 33:795–814, 2009.
- [44] H. M. Kamar, R. Ahmad, N. B. Kamsah, and A. F. M. Mustafa. Artificial neural networks for automotive air-conditioning systems performance prediction. *Applied Thermal Engineering*, 50:63–70, 2013.
- [45] K. R. Kambly and T. H. Bradley. Estimating the HVAC energy consumption of plug-in electric vehicles. *Journal of Power Sources*, 259:117–124, 2014.
- [46] C. Kasnakoğlu, A. Serrani, and M. Ö. Efe. Control input separation by actuation mode expansion for flow control problems. *International Journal of Control*, 81:1475–1492, 2008.
- [47] G. Kerschen, J. C. Golinval, A. F. Vakakis, and L. A. Bergman. The method of proper orthogonal decomposition for dynamical characterization and order reduction of mechanical systems: An overview. *Non-linear Dynamics*, 41:147–169, 2005.
- [48] H. Khayyam, A. Z. Kouzani, and E. J. Hu. Reducing energy consumption of vehicle air conditioning system by an energy management system. In *IEEE Intelligent Vehicles Symposium*, 2009.
- [49] H. Khayyam, S. Nahavandi, E. Hu, A. Kouzani, A. Chonka, J. Abawajy, V. Marano, and S. Davis. Intelligent energy management control of vehicle air conditioning via look-ahead system. *Applied Thermal Engineering*, 31:3147–3160, 2011.
- [50] K. I. Kim, K. Jung, and H. J. Kim. Face recognition using kernel principal component analysis. *IEEE Signal Processing Letters*, 9:40–42, 2002.

- [51] T. Kimura, T. Tanaka, K. Fujimoto, and K. Ogawa. Hydrodynamic characteristics of a butterfly valve – Prediction of pressure loss characteristics. *ISA Transactions*, 34:319–326, 1995.
- [52] M. Kirby. *Geometric data analysis: an empirical approach to dimensionality reduction and the study of patterns*. John Wiley & Sons, 2000.
- [53] Y. Kobayashi, K. Yoshida, H. Nagano, and I. Kohri. Proper orthogonal decomposition analysis of flow structures generated around engine cooling fan. *SAE International Journal of Passenger Cars-Mechanical Systems*, 7:728–738, 2014.
- [54] W.H. Kolbe, E.W. Yott, B.B. Brown, G.M. Gaskill, and W. Martin. The 1964 Cadillac comfort control. In *SAE Transactions*, 1965.
- [55] T. Korthals. *Numerische Untersuchung der Ausblastemperaturen eines Klimagerätes*. Student thesis at the chair of thermodynamics, Technische Universität München, 2016.
- [56] T. Lex. *Fluidodynamik von Gas-Flüssigkeits-Gemischen in Kugelhähnen*. PhD thesis, Technische Universität München, 2004.
- [57] J. Lindenblatt. *Erweiterung und Validierung eines instationären Modells zur Berechnung der Wärmeverluste in Luftführungen*. Student thesis at the chair of thermodynamics, Technische Universität München, 2017.
- [58] J. Ling, V. Aute, Y. Hwang, and R. Radermacher. A new computational tool for automotive cabin air temperature simulation. *SAE International Journal of Passenger Cars-Mechanical Systems*, 6:841–846, 2013.
- [59] M. Lorenz. *Reduction of heating loads and interior window fogging in vehicles*. PhD thesis, Technische Universität München, 2015.
- [60] S. Lorenzi, A. Cammi, L. Luzzi, and G. Rozza. POD-Galerkin method for finite volume approximation of navier–stokes and RANS equations. *Computer Methods in Applied Mechanics and Engineering*, 311:151–179, 2016.

- [61] B. Lu. *Entwicklung eines Rechenmodelles zur Vorhersage der Luftverteilung im Klimagerät*. Student thesis at the chair of thermodynamics, Technische Universität München, 2016.
- [62] J. L. Lumley. *Stochastic tools in turbulence*. Courier Corporation, 2007.
- [63] H. V. Ly and H. T. Tran. Modeling and control of physical processes using proper orthogonal decomposition. *Mathematical and Computer Modelling*, 33:223–236, 2001.
- [64] M. Massoud. *Engineering thermofluids*. Springer, 2005.
- [65] F. R. Menter. Improved two-equation k-omega turbulence models for aerodynamic flows. NASA, 1992.
- [66] M. Mohanraj, S. Jayaraj, and C. Muraleedharan. Applications of artificial neural networks for refrigeration, air-conditioning and heat pump systems – A review. *Renewable and Sustainable Energy Reviews*, 16:1340–1358, 2012.
- [67] G. Mustafaraj, J. Chen, and G. Lowry. Development of room temperature and relative humidity linear parametric models for an open office using BMS data. *Energy and Buildings*, 42:348–356, 2010.
- [68] R. Narasimha. Kosambi and proper orthogonal decomposition. *Resonance-Heidelberg*, 16:574, 2011.
- [69] B. C. Ng, I. Z. M. Darus, H. Jamaluddin, and H. M. Kamar. Application of adaptive neural predictive control for an automotive air conditioning system. *Applied Thermal Engineering*, 73:1244–1254, 2014.
- [70] B. C. Ng, I. Z. M. Darus, H. Jamaluddin, and H. M. Kamar. Dynamic modelling of an automotive variable speed air conditioning system using nonlinear autoregressive exogenous neural networks. *Applied Thermal Engineering*, 73:1255–1269, 2014.
- [71] B. R. Noack. *Niederdimensionale Galerkin-Modelle für laminare und transitionelle freie Scherströmungen*. 2006.

- [72] G. S. Okochi and Y. Yao. A review of recent developments and technological advancements of variable-air-volume (VAV) air-conditioning systems. *Renewable and Sustainable Energy Reviews*, 59:784–817, 2016.
- [73] H. M. Park and D. H. Cho. The use of the karhunen-loeve decomposition for the modeling of distributed parameter systems. *Chemical Engineering Science*, 51:81–98, 1996.
- [74] K. Pearson. On lines and planes of closest fit to systems of points in space. *The London, Edinburgh, and Dublin Philosophical Magazine and Journal of Science*, 2:559–572, 1901.
- [75] A. Qamar and S. Sanghi. Steady supersonic flow-field predictions using proper orthogonal decomposition technique. *Computers and Fluids*, 38:1218–1231, 2009.
- [76] S. J. Qin. Survey on data-driven industrial process monitoring and diagnosis. *Annual Reviews in Control*, 36:220–234, 2012.
- [77] X. Qu, Z. Qi, J. Shi, J. Chen, and H. Zhou. Numerical model of the temperature control curve linearity of HVAC module in automobile air-conditioning system and applications. *Journal of Thermal Science and Engineering Applications*, 2:041008, 2010.
- [78] W. Roetzel and B. Spang. *VDI-Wärmeatlas: Berechnung von Wärmeübertragern*. Springer, 2002.
- [79] S. Sambandan and M. Valencia. Robust 1D modelling for automotive HVAC warmup prediction using DFSS approach. In *SAE Technical Paper*, 2017.
- [80] B. Schmandt. *Eine standardisierte Methode zur numerischen Bestimmung von Strömungsverlusten unter Einbeziehung des zweiten Hauptsatzes der Thermodynamik*. PhD thesis, TU Hamburg, 2014.
- [81] B. Schmandt and H. Herwig. A standard method to determine loss coefficients of conduit components based on the second law of thermodynamics. In *ASME Conference Proceedings*, 2012.

- [82] F. Selimefendigil. Numerical analysis and POD based interpolation of mixed convection heat transfer in horizontal channel with cavity heated from below. *Engineering Applications of Computational Fluid Mechanics*, 7:261–271, 2013.
- [83] S. Shojaei, S. Robinson, C. Chatham, A. McGordon, and J. Marco. Modelling the electric air conditioning system in a commercially available vehicle for energy management optimisation. In *SAE Technical Paper*, 2015.
- [84] L. Si, M. Hirz, and H. Brunner. Big data-based driving pattern clustering and evaluation in combination with driving circumstances. In *SAE International World Congress Experience*, 2018.
- [85] S. Sirisup and G. E. Karniadakis. Stability and accuracy of periodic flow solutions obtained by a POD-penalty method. *Physica D: Nonlinear Phenomena*, 202:218–237, 2005.
- [86] L. Sirovich. Turbulence and the dynamics of coherent structures. I. Coherent structures. *Quarterly of Applied Mathematics*, 45:561–571, 1987.
- [87] B. Tashtoush, M. Molhim, and M. Al-Rousan. Dynamic model of an HVAC system for control analysis. *Energy*, 30:1729–1745, 2005.
- [88] W. L. Tse and W. L. Chan. An automatic data acquisition system for on-line training of artificial neural network-based air handling unit modeling. *Measurement*, 37:39–46, 2005.
- [89] M. A. Turk and A. P. Pentland. Face recognition using eigenfaces. In *IEEE Computer Vision and Pattern Recognition*, 1991.
- [90] A. Vendl, H. Faßbender, S. Görtz, R. Zimmermann, and M. Mifsud. Model order reduction for steady aerodynamics of high-lift configurations. *CEAS Aeronautical Journal*, 5:487–500, 2014.
- [91] Verification and Validation Committee. *Standard for Verification and Validation in Computational Fluid Dynamics and Heat Transfer*. The American Society of Mechanical Engineers, 2009.

- [92] Y. Wang, B. Yu, Z. Cao, W. Zou, and G. Yu. A comparative study of POD interpolation and POD projection methods for fast and accurate prediction of heat transfer problems. *International Journal of Heat and Mass Transfer*, 55:4827–4836, 2012.
- [93] Z. Wang, I. Akhtar, J. Borggaard, and T. Iliescu. Proper orthogonal decomposition closure models for turbulent flows: a numerical comparison. *Computer Methods in Applied Mechanics and Engineering*, 237:10–26, 2012.
- [94] K. Watanuki and T. Murata. Fuzzy-timing petri net model of temperature control for car air conditioning system. In *IEEE SMC Conference Proceedings*, 1999.
- [95] T. Weustenfeld. *Heiz- und Kühlkonzept für ein batterieelektrisches Fahrzeug basierend auf Sekundärkreisläufen*. PhD thesis, Technische Universität Braunschweig, 2017.
- [96] F. Wöhr. *Niederdimensionale Modellierung der Strömungstemperaturen in den Luftkanälen einer Fahrzeug-Klimaanlage*. Student thesis at the chair of thermodynamics, Technische Universität München, 2017.
- [97] C. G. Wu, Y. C. Liang, W. Z. Lin, H. P. Lee, and S. P. Lim. A note on equivalence of proper orthogonal decomposition methods. *Journal of Sound and Vibration*, 5:1103–1110, 2003.
- [98] S. Yin, S. X. Ding, X. Xie, and H. Luo. A review on basic data-driven approaches for industrial process monitoring. In *IEEE Transactions on Industrial Electronics*, 2014.
- [99] N. Zhang, B. Cao, Z. Wang, Y. Zhu, and B. Lin. A comparison of winter indoor thermal environment and thermal comfort between regions in europe, north america, and asia. *Building and Environment*, 117:208–217, 2017.
- [100] Q. Zhang and M. Canova. Lumped-parameter modeling of an automotive air conditioning system for energy optimization and management. In *ASME Dynamic Systems and Control Conference*, 2013.

- [101] Q. Zhang, S. Stockar, and M. Canova. Energy-optimal control of an automotive air conditioning system for ancillary load reduction. In *Automotive Air Conditioning*, 2016.